8-1-2002

A Three-dimensional ray tracing simulation of a synthetic aperture ground penetrating radar system

James III Jeter

A Three-Dimensional Ray Tracing Simulation of a Synthetic Aperture Ground Penetrating Radar System

By

James W. Jeter III

A Thesis Submitted

in Partial Fulfillment of the

Requirements for the Degree of

MASTER OF SCIENCE

In

Electrical Engineering

Approved by the
Thesis Committee:

_____
Dr. Vincent J. Amuso, Thesis Adviser

_____
Dr. Sohail A. Dianat, Member

_____
Dr. Raghuveer Rao, Member

_____
Dr. John Schott, Member

_____
Dr. Robert J. Bowman, Department Chairman

Rochester Institute of Technology
Rochester, New York

August 2002

The views expressed in this thesis are those of the author and do not reflect the official policy or position of the United States Air Force, Department of Defense, or the U.S. Government.

I, James W. Jeter III, hereby grant permission to the Wallace Library of the Rochester Institute of Technology to reproduce my thesis in whole or in part. Any reproduction will not be for commercial use or profit.

Date: 8/27/02 Signature of Author: _____

Table of Contents

List of Tables

List of Figures

ACKNOWLEDGEMENTS

I would like to thank my thesis committee, for providing input and suggestions throughout the writing process. I would also like to thank Douglas Lynch, Russell Brown, James VanDamme, Michael Wicks, and Al George for giving me the opportunity to work with their system and offering their expertise in teaching me about it. I would especially like to thank Dr. Amuso for being patient and keeping me on track. I couldn't have asked for a better advisor and I wish you the best of luck in future endeavors. Finally, I would like to thank my parents, who through this, as with everything else, have given me the strength, advice and support I needed.

ABSTRACT

Ground Penetrating Radar (GPR) is a useful tool for imaging the area below the Earth's surface. GPR works on the same principle as traditional radar, evaluating the electromagnetic returns reflected from an object or scene of interest to determine characteristics of the object that reflected the signal. Synthetic Aperture Radar (SAR) is a technique which combines radar returns of a given scene collected at several positions. By compiling the information contained in the returns, an image of a scene can be generated. Combining these two concepts allows us to create an image of an underground scene.

Air Force Research Lab, Rome, NY developed a ground penetrating, SAR system with a resolution of approximately three feet capable of penetrating to depths of 150-160 feet into the ground. In order to assess the results obtained from this system, a simulation was needed to generate expected returns from a user-defined synthetic scene.

Ray-tracing is a simulation technique that is frequently used to model radar and imaging systems. In the ray-tracing model, the transmitted radar signal is simulated by a number of straight lines, or rays, which propagate through the scene according to the principles of electromagnetic theory. The data carried with each ray can be used to generate a simulated radar return at the receiver.

This thesis describes a ray-tracing simulator, which was created to work in conjunction with the Rome Labs GPR system. The ray-tracing simulation models the transmissions and reflections from faceted target models using Snell's law and the Law

of Reflection. The results obtained demonstrate the effects that different scene orientations have upon the images generated by the Rome Labs system.

1. Introduction

When finding a needle in a haystack, it is helpful to know what the needle looks like. Ground penetrating radar data often resembles the proverbial haystack. A layer of ground with an unknown physical makeup obscures the target of interest, making it difficult to discern if the target is being observed, or simply another piece of hay. The unknown nature of the underground environment adds uncertainty as to how a valid return should look for a given target. The data received from a target of interest is often cluttered with returns from other objects around it, making it hard to interpret. It is useful to have a means to generate a controlled return that is created in a scene composed of material whose properties and dimensions are known. The control return can be used to aid in interpreting the received data or as a diagnostic tool for the GPR system.

Control return data can be generated either from a controlled test environment or a simulated scene. A controlled test environment is difficult to create in a GPR environment because it must be submerged underground and uncovered whenever changes are made to the scene's configuration. This technique is not only labor intensive, but prone to errors caused by soil property inconsistency. It is useful to have a means of accurately generating synthetic data based upon a simulated scene that can be easily manipulated. A simulated return from a synthetic scene provides this needed capability.

1.1 Problem Statement

This thesis presents a simulator that was developed to be used with a GPR system designed by Rome Labs. The Rome Labs GPR system employs synthetic aperture radar

to image an underground scene. A signal is transmitted from a single transmitter location and measured at several receiver locations within a receiver array grid. From these returns an image is generated in a simulated scene space. Rome Labs also developed a simulator in conjunction with their GPR system. The Rome Labs simulator models targets as ideal point reflectors that reflect equally to every receiver location in the receiver array grid. While this technique provides diagnostic validation of the GPR system, it does not provide the flexibility to accurately model the physical properties of different antenna and targets in the scene. The objective for this thesis is to develop a simulator that simulates complex targets, can accurately simulate the electromagnetic properties of the transmitted signal, is easily modified for different scenes, and is easily upgradeable.

1.2 *Overview*

The purpose of this thesis is to describe the implementation of a simulation technique that improves upon the simulator designed by Rome Labs. The document is organized as described below:

Chapter 1: Introduce the problem and define the bounds of the solution.

Chapter 2: Reviews works researched in the area of ground penetrating radar.

Chapter 3: Describes the background theory necessary to adequately describe the simulation technique.

Chapter 4: Describes the simulation approach used.

Chapter 5: Discusses the Rome Labs ground penetrating radar processing system.

Chapter 6: Describes the experimental implementation of the GPR simulator and discusses the results.

Chapter 7: Summarizes conclusions made through experimentation and discusses potential future activities.

2. *Review of Literature*

It is considerably more difficult to model a ground penetrating radar system than to model a similar system designed for use above ground. Simulations used in ground penetrating radar must account for phenomena that can be neglected in above ground radar simulators. The dielectric properties of the ground can be varied, which can cause unwanted clutter or ambiguous returns. Attenuation limits the depth of ground penetration and affects the frequencies that can be used. The limited depth of penetration and frequency requirements can also force the radar to operate in the near field. The simulation technique used needs to account for these constraints. Two techniques that are frequently used to simulate GPR systems are the finite difference, time domain (FDTD) technique and the ray-tracing technique.

2.1 Finite Difference, Time Domain Technique

Maxwell's equations rely upon initial temporal and spatial boundary conditions to calculate the magnitude of an electromagnetic field. In a heterogeneous dielectric medium, the dielectric properties vary considerably making Maxwell's equations difficult to solve. The FDTD technique was proposed by Kane S. Yee in his 1965 paper 'Numerical Solutions of Initial Boundary Value Problems Involving Maxwell's Equations in Isotropic Media' to solve Maxwell's equations sequentially. Yee divides the region of interest into a number of small cubic regions, using a discrete approach to evaluate Maxwell's equations at many points throughout the scene. Boundary conditions

for these regions are first defined and Maxwell's equations are then solved sequentially for each cube.

The first step in the FDTD technique involves dividing the region of interest into a grid of cubic regions (see Figure 2.1). These cubes will be referred to as cells. The dimensions of each cell in the grid must be a fraction of the wavelength of the transmitted signal [1]. Boundary conditions are then defined for each cell in the grid. Yee assumes the conducting surface to be a perfectly conducting surface and limits his calculations to the transverse magnetic field case, where the magnetic component of the electromagnetic field is parallel to the

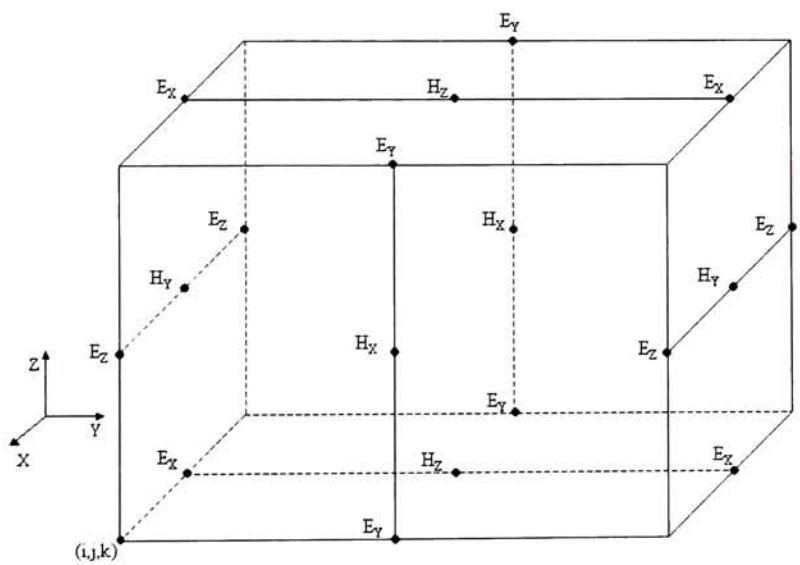

Figure 2.1: Yee Cube

surface. The tangential components of the electric field and the normal component of the magnetic field are therefore both zero. By using the X,Y, and Z directional components of Maxwell's equations, the electromagnetic field can be evaluated sequentially along all

of the discrete borders of the cells in the target scene. These modified versions of Maxwell's equations can be used to derive finite difference equations at the discrete cube boundaries for the transverse electric (TE) field and transverse magnetic (TM) field cases. [1]

TE case:

$$a.)\quad H_z^{n+1/2}(i+1/2,j+1/2)=H_z^{n-1/2}(i+1/2,j+1/2)-\frac{1}{Z}\frac{\Delta\tau}{\Delta x}\left[E_y^n(i+1,j+1/2)-E_y^n(i,j+1/2)\right]$$

$$+\frac{1}{Z}\frac{\Delta\tau}{\Delta y}\left[E_x^n(i+1/2,j+1)-E_x^n(i+1/2,j)\right]$$

$$b.)\quad H_y=0$$

$$c.)\quad H_x=0$$

$$d.)\quad E_x^{n+1}(i+1/2,j)=E_x^n(i+1/2,j)+Z\frac{\Delta\tau}{\Delta y}\left[H_z^{n+1/2}(i+1/2,j+1/2)-H_z^{n+1/2}(i+1/2,j-1/2)\right]$$

$$e.)\quad E_y^{n+1}(i,j+1/2)=-Z\frac{\Delta\tau}{\Delta x}\left[H_z^{n+1/2}(i+1/2,j+1/2)-H_z^{n+1/2}(i-1/2,j+1/2)\right]$$

$$f.)\quad E_z=0$$

(2-1)

TM case:

$$a.)\quad E_z^{n+1}(i,j)=E_z^n(i,j)+Z\frac{\Delta\tau}{\Delta x}\left[H_y^{n+1/2}(i+1/2,j)-H_y^{n+1/2}(i-1/2,j)\right]$$

$$-Z\frac{\Delta\tau}{\Delta y}\left[H_x^{n+1/2}(i,j+1/2)-H_x^{n+1/2}(i,j-1/2)\right]$$

$$b.)\quad E_x=0$$

$$c.)\quad E_y=0 \qquad (2\text{-}2)$$

$$d.)\quad H_x^{n+1/2}(i,j+1/2)=H_x^{n-1/2}(i,j+1/2)-\frac{1}{Z}\frac{\Delta\tau}{\Delta y}\left[E_z^n(i,j+1)-E_z^n(i,j)\right]$$

$$e.)\quad H_y^{n+1/2}(i+1/2,j)=H_y^{n-1/2}(i+1/2,j)+\frac{1}{Z}\frac{\Delta\tau}{\Delta x}\left[E_z^n(i+1,j)-E_z^n(i,j)\right]$$

$$f.)\quad H_z=0$$

Where

$$Z = \sqrt{\frac{\mu}{\varepsilon}}$$

$\tau = ct$

c = The speed of light, $2.9979 \times 10^{-7}\ m/s$

t = time

n = Numerical reference of cubic region

H = Magnetic Field Intensity

E = Electric Field Intensity

Note that for the transverse electric field case, the magnetic field components in the X and Y direction and the electric field component in the Z direction are equal to zero as a result of the assumption that the scatterer is a perfect conductor. Likewise, in the TM case, the X and Y components of the electric field and the Z component of the magnetic field are equal to zero. By performing Equations 2-1 or 2-2 for each cell in a scene from the transmitter to the receiver, the simulated radar return can be calculated.

Several variations on Yee's technique have been used to model a scene composed of dispersive media. One technique uses the Perfectly Matched Layer (PML), which defines the boundary conditions of the cells such that the cells maintain their dispersive properties. It also allows the borders of the scene of interest to be modeled as an infinite domain extending away from the scene. [2]

In order to accurately model a ground penetrating radar scene using the FDTD technique, the entire region must be divided into cells and digitized. This includes the transmitting and receiving antennas, as well as all scatterers in the scene. Some problems can result from modeling the scene in this fashion. If the cells are large compared to the width of the antenna material, it may be difficult to accurately represent the antenna using

cells. This problem is exacerbated if one of the antennas or another object in the scene contains edges that are not at right angles. These objects must be modeled by cells oriented diagonally to each other in a staircase fashion. The antennas used in the Rome Labs GPR system are bow-tie antennas, which have diagonal components that are not oriented at right angles. This makes them difficult to model using the FDTD technique. This can be a source of significant error for simulations operating in the near field. [3] Yasuhiro Nishioka et al used Yee's FDTD technique to simulate a GPR scene that uses bow-tie transmit and receive antennas. Nishioka modified the discrete versions of Maxwell's equations to include non-square cells, which could be used to more effectively approximate the shape of the bow-tie antennas.

While the FDTD technique provides a very accurate simulation approach, it has some significant problems. The FDTD technique steps through the entire scene and sequentially calculates the electromagnetic field contributions at each cell along the way. This enables the FDTD technique to accurately account for the cumulative dispersive characteristics of each cell. It also allows a very complex scene to be modeled, and makes the FDTD technique an effective simulator of both near field and far field antenna gain patterns. However, using this approach also creates some problems. The size of the cells is dictated by the frequency used by the transmitter. Yee recommends using cells that are smaller than a wavelength, requiring the number of cells needed to model a large scene to be very high. The number of calculations that must be performed and the boundary conditions that must be defined are related to the number of cells in the scene. The large number of calculations needed to model the scene can cause simulation run

times to be prohibitive. The FDTD technique also requires the transmit and receive antennas to be modeled very accurately. The antenna shape must be re-created from individual cells and the material properties of each cell must match those of the antenna. To model different antenna gain patterns, the physical properties of the antenna must be changed rather than simply altering the gain pattern.

2.2 Ray-tracing technique

The propagation of an electromagnetic field through a medium exhibits some characteristics of a particle traveling through space and some characteristics of a wave. The ray-tracing technique leverages upon the particle-like behavior of electromagnetic fields, using straight, narrow beams, or rays, to represent electromagnetic fields. This technique is also used to model optical systems. Ray-tracing is considered valid for frequencies above 10MHz [4] and for objects that are larger than a wavelength. [5]

In the ray-tracing technique, rays are generated at a source and made to propagate through a scene containing synthetically generated scatterers based upon the rules of geometric physics. To determine if the rays intersect the scatterer, the scene must be simulated spatially, with the objects in the scene represented by mathematical functions. If the rays intersect a scatterer in the scene, a portion of the electromagnetic field will be reflected from the surface of the scatterer and a portion will be transmitted through the object.

The synthetic return is calculated based upon the rays that propagate to a given observation point. The total distance traveled by the ray can be determined by summing all of the path segments the ray takes between object intersections. The magnitude of the

rays can be calculated based upon path distance, dielectric properties of the scene, and the number of reflections and transmissions a ray undergoes.

The ray-tracing technique can be approached with either a forward ray-tracing technique, or a backward ray-tracing technique. The forward model projects rays from the transmitter, models their propagation through a scene, and then measures the parameters of the rays that arrive at a receiver location. In the backward model, rays are projected from the receiver, made to propagate through a scene and then recorded if they intersect the transmitter. It is generally easier to use a forward technique if the source is small compared to the receiver. It is generally easier to use a backward modeling technique if the source is large compared to the receiver.[6]

For the simulation to be effective the transmitter, receiver and targets in the scene must be modeled mathematically and material properties of the objects in the scene must be defined. Several techniques have been used to mathematically represent the scatterers in the scene. Cai and McMechan demonstrated a method for the two-dimensional case, which approximates the scatterers as continuous polynomial functions. The material properties of the modeled scatterers are assigned to the function. [5] Another two-dimensional technique, which was used by Goodman, requires the scene to be divided into a grid and the target modeled as a series of piece-wise continuous functions within each section of the grid. The material properties of the targets in this technique are associated with each section of the grid. [7] In three-dimensional space, the targets can be modeled as three-dimensional surfaces or using a series of triangular facets to

represent the surface. [6] The target's material properties must be either assigned to the surface, or assigned to each of the facets that make up the target.

After the targets have been defined in the scene, the direction of the rays must be determined. For a ray-tracing model to accurately simulate a radar transmit antenna, the number of rays, their origin and direction vectors must be chosen to reflect the characteristics of the antenna. Antenna main and side lobes gain patterns can be modeled using different directions and groupings of rays. A transmitter operating in the far field can use a series of parallel rays to simulate its antenna gain pattern. The Fresnel field can be represented by a series of rays fanning out from a single origin. [8]

The path distance of the rays as they propagate through the scene can be calculated using Snell's Law and the Law of Reflection to define the path the transmitted and reflected rays will take when they come into contact with the scatterers in the scene. Several different methods are used to calculate the ray's path distance. In the two-dimensional case used by Cai and McMechan, rays are traced in the incident and reflected direction at evenly spaced points on the target curve. The angle between the incident and reflected ray is varied, subject to the Law of Reflection until the offset of the two rays on the surface is equal to the constant offset between the transmitter and receiver. The technique used by Glassner in the three-dimensional case involves calculating the reflected and transmitted ray based upon the incident ray and the angle it makes with a line that is normal to the target surface.

While geometrical optics simulation approaches account for the particle-like behavior of electromagnetic fields, the physical optical properties, which define a field's

wave-like behavior are not adequately accounted for. Diffraction, dispersion, and diffuse reflections are examples of some wave-like behavior that are not modeled in standard ray-tracing techniques. Several simulation techniques have been used to account for these effects. Sato, Wakayama and Takemura modeled diffracted rays by adding additional rays to the outer edge of a target when a ray came in contact with the edge of the target. [9] Goodman proposed combining the results of several different ray trace runs with different material parameter settings to simulate dispersion. [7]

The ray's attenuation can be determined by keeping track of the types of material it travels through and the number of times it interacts with another material. Goodman and Cai et al proposed similar techniques for measuring attenuation. Both considered the amplitude of the transmitted signal, effects of path attenuation, as well as attenuation caused by the reflection and transmission of the rays.

Ray-tracing provides a simple, intuitive method to model an electromagnetic system. The targets can be easily modeled using facets at varying degrees of detail, and can be moved around the scene with relative ease. The antenna gain pattern can be changed intuitively by adjusting the direction and origin of the rays. Wavelike characteristics of the field can be included, although it may introduce additional complexity. While the computer system requirements of a complex scene can be substantial, it is dependent upon the number of rays in the scene, allowing a low fidelity model to be performed using fewer rays.

The objective for modifying the Rome Labs GPR simulator was to develop a model that simulates complex targets, can accurately simulate the electromagnetic

properties of the transmitted signal, is easily modified for different scenes, and is upgradeable. The ray-tracing technique was selected for the simulator because it satisfied these objectives and was readily compatible with the current system.

3. Theory

3.1 Electromagnetic Waves

Radar is similar in concept to a sound wave echoing from a canyon wall. By measuring the elapsed time between when the sound is produced and when it is heard, the distance to the canyon wall can be calculated using simple kinematics and the speed of sound. The behavior of electromagnetic waves in radar is analogous to the sound wave's behavior in the echo example described above. In radar, the elapsed time of an electromagnetic wave is measured as it is transmitted, reflected from a target, and received by a receiver. Electromagnetic waves exhibit many of the characteristics of sound waves, except that while sound waves are created by amplitude fluctuations of air, an electromagnetic wave is created by fluctuations of electric and magnetic fields.

When two charged particles are introduced into an environment, they tend to exert either an attractive or repulsive force on each other. Two positively or negatively charged particles will repel each other, while a positive and a negative charge exert an attractive force. These forces are caused by an electric field, which is present whenever two or more charges exert an attractive or repulsive force upon each other. [10] The electric field can be quantized with the units of volts/meter and is a measure of the force per unit charge created by the interaction between several electrical charges. [11] When more than one charged particle is present, the electric field generated is the sum of the fields created by all of the charges present.

In addition to the forces exerted on charges by an electric field, an additional force acts upon charges when they are moved through a voltage gradient. This force is

known as a Lorentz force and is caused by a magnetic field. A current is formed when a charge is moved along a voltage gradient, therefore, when a current is present, it creates a magnetic field.

While electric and magnetic fields are separate entities, they do have a symbiotic interrelationship. The relation between the electric and magnetic fields was quantified by Maxwell and expressed in the form of Equations (3-1)a-d. These equations are known collectively as Maxwell's equations.

$$\begin{aligned} &a.) \quad \oint \mathbf{E} \cdot d\mathbf{S} = \frac{q}{\varepsilon_0} \\ &b.) \quad \oint \mathbf{B} \cdot d\mathbf{S} = 0 \\ &c.) \quad \oint \mathbf{E} \cdot dl = -\frac{d\Phi_B}{dt} \\ &d.) \quad \oint \mathbf{B} \cdot dl = \mu_0 \varepsilon_0 \frac{d\Phi_E}{dt} + \mu_0 i \end{aligned} \tag{3-1}$$

Where E is the electric field, **S** is a volume, q is the charge, **B** is the magnetic flux density, l is a linear surface, Φ_E is the electric flux, Φ_B is the magnetic flux and μ and ε represent the magnetic permeability and dielectric permittivity of the material the wave is propagateing through. The magnetic flux is the total net amount of magnetic flux density entering or leaving a volume. Similarly, the electric flux is the total net magnitude of electric field density entering or leaving a volume. The magnetic permeability and dielectric permittivity are parameters that describe the properties of the material the electromagnetic wave is propagateing through, and will be discussed in more detail later. Equation (3-1)a states that the total flux of electric field leaving a closed volume is equal to the charge in the volume. Equation (3-1)b is analogous to Equation (3-1)a for the

magnetic field case. It states that the net amount of magnetic flux density leaving a closed volume is zero. Therefore, the net magnetic flux is zero.

Equation (3-1)c quantitatively states that an electric field is created by a time-varying magnetic field. Conversely, Equation (3-1)d shows that a magnetic field can be created by electric currents or a time-varying electric field. [12]

When a charged particle is accelerated, a time varying electric field is created which begins in the vicinity of the charge's acceleration and propagates radially away from it. This induces a time-varying magnetic field, which in turn contributes to the electric field. In this manner, the electromagnetic field propagates away from the accelerated charge. This phenomenon is known as an electromagnetic wave. From this point on, the electric field will be annotated by the vector **E** and the magnetic field will be referred to as the vector **B**.

The **E** and **B** components of the electromagnetic wave are mutually orthogonal. The electromagnetic wave propagates in the direction of the Poynting Vector, S, which is defined as

$$\vec{\mathbf{S}} = \vec{\mathbf{E}} \times \vec{\mathbf{B}} \tag{3-2}$$

The Poynting Vector is equal to the rate of energy flow per unit area. The directional relationship between the Poynting Vector and the E and B fields is pictured in Figure 3.1.[13]

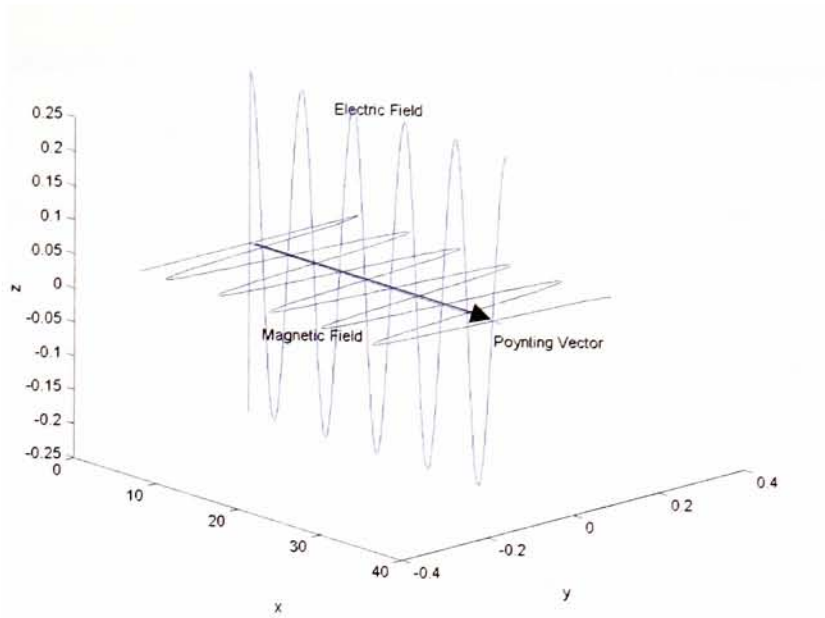

Figure 3.1. Electric and Magnetic Field components of an EM wave

The time varying nature of the **E** and **B** components of the electromagnetic wave give rise to the electromagnetic wave equation, Equation (3-3).

$$\begin{aligned} a.) \quad & E(r,t) = \mathrm{Re}[\hat{E}(r)e^{j\omega t}] \\ b.) \quad & H(r,t) = \mathrm{Re}[\hat{H}(r)e^{j\omega t}] \end{aligned} \tag{3-3}$$

where r is distance, t is time, and ω is angular frequency.[11]

3.2 Electromagnetic fields

When a rock is dropped into a smooth surface of water, the waves ripple away radially from the disturbance. Right after the rock hits the water, the wave moves away from it in a very tight circle. As the ripple moves away from the disturbance, the circular ripple grows larger and larger in radius. At a sufficient distance from the point where the rock impacted the water, the radius will be so large that the ripple will almost look flat (if

only a small section is observed). Continuing the water ripple metaphor, the ripple can be said to make a wavefront as it moves through the water away from the disturbance. A wavefront is a line connecting all equal phase points of a wave.

Electromagnetic waves behave similarly to the waves caused by the rock in the pool. In Section 3.1, we discussed electromagnetic behavior in a single direction. They actually move in every direction at once, similar to a ripple in a still body of water. As with the water ripple example, the wavefront is different depending on the target's distance from the antenna. The further the wavefront travels from the origin of the wave, the closer a small section is to being flat. Three range regions have been identified to classify the wavefront at different distances: the Fraunhofer (far-field) region, the Fresnel region, and the near-field region. The Fraunhofer region is valid for targets at distances that are greater than D^2/λ from the transmitter, where D represents aperture size and λ is the wavelength of the transmitted electromagnetic wave (defined by Equation (3-4)).

$$\lambda = \frac{c}{f} \tag{3-4}$$

This region is far enough from the antenna that the spherical wave fronts transmitted from the antenna can accurately be approximated by a plane. The field is the same at all points at an equal distance from the transmitter. The wavefront of antennas operating in this region can be modeled by a series of planar wave fronts. The Fresnel region extends from $D^2/4\lambda$ to the point D^2/λ from the transmitter. The Fresnel region is not far enough from the antenna that the effect of the curvature of the spherical wave fronts transmitted by the antenna can be negated. In this region, the antenna pattern is not constant over a

certain distance. The gain pattern of antennas operating in this region can be modeled by a series of spherical wave fronts. [8] The near field extends from the transmitter to a distance $D^2/4\lambda$ from the aperture. [14] The near field region is close enough to the transmit antenna that the effects of different lobes of the antenna in this region affect the emissions along the length of the antenna.[15]

3.3 Antenna reflection characteristics

Electromagnetic waves behave differently depending upon the material properties and size of the medium they are propagating through. The material properties of a medium can be characterized by three parameters: magnetic permeability (μ), dielectric permeability (ε), and electric conductivity (σ). [16] Magnetic permeability is a measure of a medium's magnetic properties. The dielectric permeability is a measure of the medium's relative capacitance. [10] Dielectric permeability is proportional to the current caused by the displacement of bound charges and has its greatest effect upon the field at higher frequencies. [16] The electric conductivity describes a material's currents caused by free charge flow and affects the field most strongly at lower frequencies. The velocity of an electromagnetic wave through a medium is a function of the medium's dielectric permittivity and magnetic permeability. The equation for calculating the velocity of an electromagnetic wave through a medium is

$$v = \frac{c}{\sqrt{\varepsilon\mu}} \tag{3-5}$$

It is possible that the values of ε and μ will vary for different frequencies. This will cause the velocity of propagation to change based upon the frequency of the electromagnetic field. This effect is known as dispersion. [17]

3.4 Physical and Geometric Models

In the previous sections, electromagnetic waves have been compared to sound waves and waves in the water. While electromagnetic waves exhibit wave-like behavior, under some circumstances, they also exhibit behavior that is similar to a particle traveling in a straight line. Under these circumstances, its path can be approximated by a narrow, straight line that extends perpendicularly to the wavefront, or a ray. [4] The ray's behavior is governed by specific rules as it reflects and passes through the surfaces of objects it comes into contact with. The technique of using rays to represent the path of an electromagnetic wave's propagation is known as a geometrical model. The geometrical model is an approximation of the exact behavior of the electromagnetic wave, but is valid if the electromagnetic wave is impeded only by objects that are much larger than a wavelength and if a great degree of accuracy is not needed around the sharp edges of the objects in the scene. [4] In cases where the geometrical model approximation is not valid, the electromagnetic wave can be modeled according to its wave-like behavior as it propagates and comes into contact with other objects around it. This technique is known as a physical model. The following section will discuss the interaction of an electromagnetic wave with objects in its path, both from the physical and geometrical perspectives.

The interaction of an electromagnetic wave with objects in its path will first be described using the physical model. When a field propagates through a homogenous medium, it is generally directed away from the transmitter. When the wave encounters a transition from one medium to another, it causes the field to change directions.[10] If a field propagates through a vacuum, it will continue on unimpeded indefinitely. When the incident field propagates through a constant medium, it oscillates the charges associated with the free electrons in the medium. These oscillations create a field emanating from each atom in the medium. Assuming the material is fairly constant, the field emanates from each atom similar to a point source. This creates a series of spherical wave fronts propagating from each point along the surface. Each of the spherical wave fronts causes constructive or destructive interference with the wave fronts surrounding it. When the field encounters an object of a different material, the pattern of the molecules will also change. This results in a change in the spherical wave fronts emitted from the atoms within the material. The spherical wave fronts will be directed both into the new material and also away from it. This phenomena is known as reflection and transmission. At distances very close to any sharp edges of the object, diffraction occurs. The spherical waves from the molecules on the edges of the object will not combine with the same number of spherical waves as a molecule in the center of the object. This causes the electromagnetic wave to propagate in a slightly curved fashion around the edge of the object.

If the size of the object is large compared to the wavelength of the incident field, the reflected and transmitted components can be described using the geometrical model.

Richard B. Feynman describes the geometrical model in his book *QED The Strange Theory of Lig d Matter.*

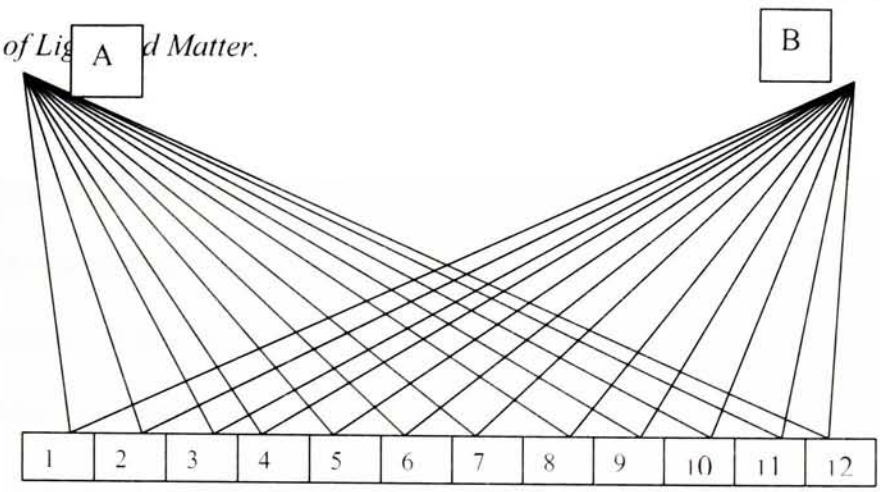

Figure 3.2 Feynman's QED Analysis of Reflection

Feynman's technique involves tracing a number of lines to represent possible routes that the field can take from point A to point B in Figure 3.2. Point A represents the transmitter and B the receiver. These paths are numbered according to the spot where they intersect the surface. Each path requires the field to propagate a slightly different distance. The distance along path 1 and 12 is longer than the distance along paths 6 and 7. Because the paths are being used to represent an EM field that varies sinusoidally as a function of distance, each path can be associated with a magnitude and phase component of the EM field. If a long array of reflective paths is observed along the length of an object, countless different paths can be taken. The distribution of the phases associated with the different paths is found to be centered around the shortest path distance. The phase differences associated with the paths closer to the edges of the medium (paths

1,2,11, and 12) are further apart than the phases associated with 5 and 6. Because of superposition, the signal observed at point B will be the sum of the electromagnetic field contribution from each of these paths. The mean of the distances of all the possible paths the field can take is the path where the angle made between the incident path and the normal to the surface is equal to the angle made by the reflected path and the line normal to the surface. When the phases of all of the different possible paths are added, all phases except that belonging to the shortest distance will cancel out. The shortest path distance from A to B occurs when the angle made between the incident ray and the line normal to the surface is the same as the angle made between the reflected ray and the normal line. [18]

The idea of an electromagnetic wave taking the shortest path between points was originally proposed by Hero of Alexandria, who lived between 150 B.C. and 250 A.D. to explain the reflective properties of light.[10] This approximation held, provided the two points are in the same medium, as is the case in the reflected example described above. In 1657, Fermat expanded on this idea, proposing that the path taken by an electromagnetic wave was actually the path of least propagation time. [10] Fermat's hypothesis applies not only to the reflected case where the wave propagates through one medium, but also to the transmitted case, where the wave must propagate through more than one medium to get from point to point. The speed of propagation is affected by the dielectric properties of the incident medium and the medium the field is incident upon. Similar to the reflective case above, the phases of all of the possible paths will cancel except for the path having the least propagation time. As discussed by Eugene Hecht in

Optics, Figure 3.3 is useful in describing the calculation of the path of shortest propagation time through an interface between two mediums.

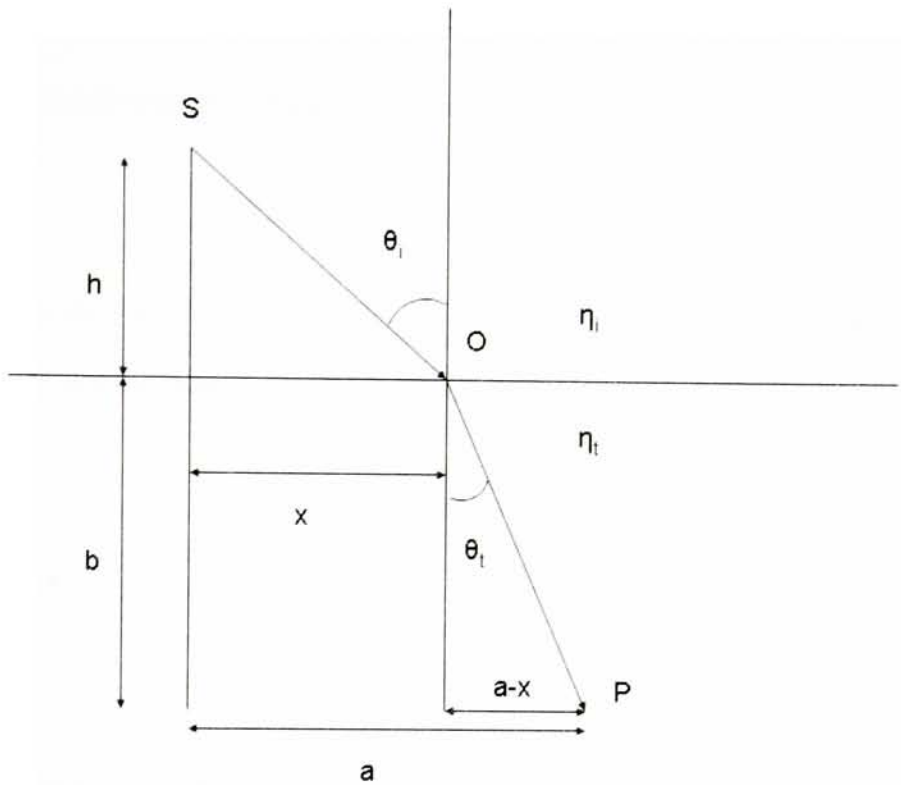

Figure 3.3 Snell's Law Definition Diagram

In this example, the path of shortest propagation time will be calculated from point S to point P. The horizontal axis line represents a transition from the incident medium to the transmitting medium. The vertical axis line represents a line normal to the surface of the medium interface. Because the two mediums have different dielectric properties, the electromagnetic wave will propagate at different speeds through the two materials. Using the equation time = distance/velocity the total time it takes for the wave to propagate from point S to point P via point O is equal to

$$t = \frac{\overline{SO}}{v_i} + \frac{\overline{OP}}{v_t} \tag{3-6}$$

where v_i and v_t represent the velocity of the wave through the incident and transmitting medium, respectively. Assuming that the points S and P are given, the path propagation time is dependent upon x. Equation (3-6) can be written in the form

$$t(x) = \frac{\sqrt{(h^2 + x^2)}}{v_i} + \frac{\sqrt{[b^2 + (a-x)^2]}}{v_t} \tag{3-7}$$

Taking the derivative of Equation (3-7) with respect to x and setting it equal zero will give the relative minimum time of propagation.

$$\frac{dx}{dt} = \frac{x}{v_i (h^2 + x^2)^{1/2}} + \frac{-(a-x)}{v_t [b^2 + (a-x)^2]^{1/2}} = 0 \tag{3-8}$$

From Figure 3.3, we can see that

$$\frac{\sin(\theta_i)}{v_i} = \frac{\sin(\theta_t)}{v_t} \tag{3-9}$$

By multiplying both sides of Equation (3-9) by the speed of light, c and making the substitution $\eta = c/v$, Equation (3-9) can be rewritten as

$$\eta_i \sin(\theta_i) = \eta_t \sin(\theta_t) \tag{3-10}$$

Equation (3-10) is known as Snell's Law. The variable η represents the index of refraction and is a property of materials.[10]

3.5 Antenna Beam Forming

Electromagnetic waves are generated by time-varying current in a transmitting antenna. The time-varying current causes time-varying electric and magnetic field components, resulting in an electromagnetic wave. When an alternating voltage is

applied to an antenna, the voltage travels down the length of the antenna. When the end of the antenna is reached, the sinusoid is reflected back towards the source of the voltage. The reflected voltage sinusoid interferes with the applied voltage, creating a standing current wave along the length of the antenna. This time varying current through the antenna creates a magnetic field and a corresponding electric field. The combined effect of the electric and magnetic fields result in an electromagnetic field emitted from the antenna. [19]

Different shaped antennas have a different current distribution along their length. [20] The current distribution of the antenna causes the magnitude of the electromagnetic field surrounding the antenna to vary according to the angle from normal and the distance from the antenna. Points of equal electromagnetic field magnitude can be plotted in a polar coordinate plane. This plot is known as an antenna's antenna pattern. The size and shape of the antenna affect the antenna pattern and therefore can be varied to generate a desired antenna pattern. The antenna pattern varies as a function of the angle normal to the antenna and distance from the antenna, and typically has several lobes occurring at different angles to the antenna. These lobes are caused by constructive and destructive interference along the length of the antenna. The lobe containing the maximum radiation is known as the main lobe. Lobes that are not in the direction of maximum radiation are referred to as side lobes. [20] A typical beam pattern is pictured in Figure 3.4.

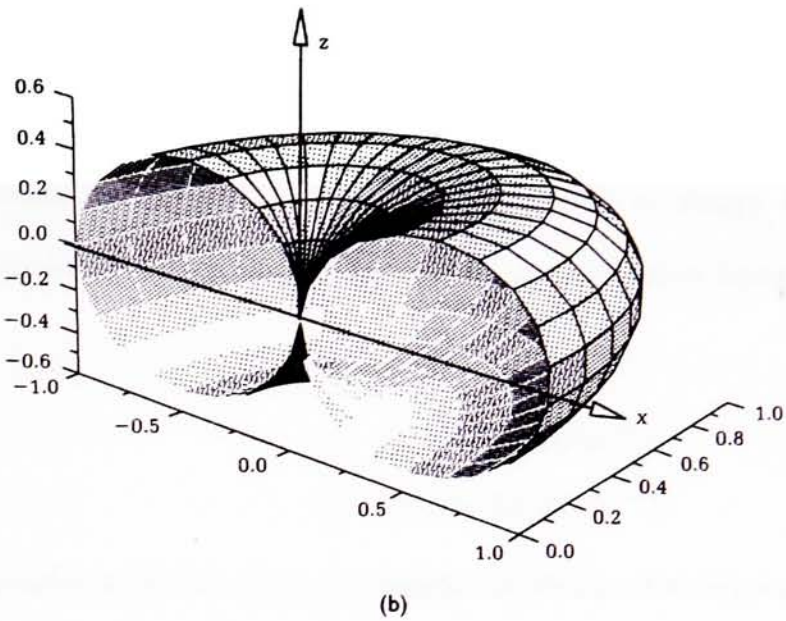

Figure 3.4. Antenna Gain Pattern of A Hertzian Dipole Antenna[1]

A receive antenna also has a gain pattern associated with it. The receive antenna's gain pattern shows the angular fluctuations and side lobes of its receiving sensitivity. The reciprocity theorem states that the antenna pattern of a receive antenna is the same as its transmit antenna pattern at the same frequency.[20]

3.6 Attenuation

In addition to causing the electromagnetic wave to change directions at a material interface, the dielectric properties of a medium also cause attenuation as the signal

---

[1] From *Applied Electromagnetism*, 2 Edition by Liang Chi Shen and Jin Au Kong, ©1987, Reprinted with permission of Brooks/Cole, an imprint of the Wadsworth Group, a division of Thomson Learning. Fax (800)730-2215

propagates through it. As an electromagnetic wave propagates through a dielectric medium, its magnitude attenuates as a function of the distance it propagates and the dielectric properties of the medium. It is also attenuated by reflections and transmissions with other materials it encounters. In an electromagnetic field, the electric and magnetic components vary sinusoidally in position and in time, as described in Equations (3-11) a and b:

$$\begin{aligned} &a.) \quad E(r,t) = \mathrm{Re}[\hat{E}(r)e^{j\omega t}] \\ &b.) \quad H(r,t) = \mathrm{Re}[\hat{H}(r)e^{j\omega t}] \end{aligned} \tag{3-11}$$

The careted variables are used to represent complex amplitudes that vary with position r. The exponential components represent time variation. [11] By applying Maxwell's equations to the time-varying electromagnetic components in Equation (3-11)a and b, Maxwell's equations can be written for a field that varies sinusoidally in time:

$$\begin{aligned} &a.) \quad \nabla x E(r) = -j\omega\mu \hat{H}(r) \\ &b.) \quad \nabla x H(r) = \hat{J_f}(r) - j\omega\varepsilon \hat{E}(r) \\ &c.) \quad \nabla \cdot \hat{E}(r) = \hat{\rho}_f(r)/\varepsilon \\ &d.) \quad \nabla \cdot \hat{B}(r) = 0 \end{aligned} \tag{3-12}$$

When Equations (3-12)a-d are considered in only the Z direction and time, and the assumption is made that there is no outside sources ($\rho_f = 0$) they can be rewritten in the form:

$$
\begin{aligned}
&a.) \quad \frac{\partial E_x}{\partial z} i_x + \frac{\partial E_x}{\partial z} i_y = -\mu \frac{\partial \overline{H}}{\partial t} = -j\omega\mu\overline{H} \\
&b.) \quad \frac{\partial H_y}{\partial z} i_x + \frac{\partial H_x}{\partial z} i_y = -\sigma E_x - \varepsilon \frac{\partial \overline{E}}{\partial t} = -(\sigma + jw\varepsilon)E_x \\
&c.) \quad \varepsilon \frac{\partial E_z}{\partial z} = 0 \\
&d.) \quad \mu \frac{\partial H_z}{\partial z} = 0
\end{aligned}
\tag{3-13}
$$

Where the variable i designates components of a unit vector. By separating the H and E vectors in Equation (3-13)a and b into their X and Y directional components, we see that E_x is related to H_y and E_y is related to H_x [11]

$$
\begin{aligned}
&a.) \quad \frac{\partial E_x}{\partial z} = -j\omega\mu H_y \\
&b.) \quad \frac{\partial E_y}{\partial z} = -j\omega\mu H_x \\
&c.) \quad \frac{\partial H_y}{\partial z} = -(\sigma + jw\varepsilon)E_x \\
&d.) \quad \frac{\partial H_x}{\partial z} = -(\sigma + jw\varepsilon)E_y
\end{aligned}
\tag{3-14}
$$

By differentiating Equation (3-14)a and substituting Equation (3-14)c, we have [21]

$$
\frac{\partial^2 E_x}{\partial z^2} = -j\omega\mu \frac{\partial H_y}{\partial z} = j\omega\mu(\sigma + j\omega\varepsilon)E_x \tag{3-15}
$$

Which is the wave equation for the electric field in the X direction. [11] Defining

$$
\gamma = \sqrt{j\omega\mu(\sigma + j\omega\varepsilon)} = \alpha + j\beta \tag{3-16}
$$

The solution of Equation (3-15) is given by

$$
E_x(z) = E_+ e^{-\gamma z} + E_- e^{\gamma z} \tag{3-17}
$$

Where E_+ and E_- are dependant upon initial conditions in time and boundary conditions in space representing the case where $z > 0$ and $z < 0$, respectively. Adding a time variant expression to Equation (3-17), we have

$$E_x(z,t) = E_+ e^{-\gamma z} e^{j\omega t} + E_- e^{\gamma z} e^{j\omega t} \tag{3-18}$$

By taking the cases where $z > 0$ and $z < 0$ separately, Equation (3-18) can be expressed as

$$E_x(z,t) = \begin{cases} \mathrm{Re}(e^{-\alpha z} E_+ e^{j(\omega t - \beta z)}); z > 0 \\ \mathrm{Re}(e^{\alpha z} E_- e^{j(\omega t + \beta z)}); z < 0 \end{cases} \tag{3-19}$$

The values for α and β can be calculated from Equation (3-16): [21]

$$\begin{aligned} &a.) \quad \gamma = \sqrt{j\omega\mu(\sigma + j\omega\varepsilon)} = \alpha + j\beta \\ &b.) \quad \gamma^2 = j\omega\mu\sigma - \omega^2\mu\varepsilon = (\alpha + j\beta)^2 \\ &c.) \quad \gamma^2 = \alpha^2 + j2\alpha\beta - \beta^2 \end{aligned} \tag{3-20}$$

The real and imaginary parts of Equation (3-20)b and c can be separated:

$$\begin{aligned} &a.) \quad \alpha^2 - B^2 = -\omega^2\mu\varepsilon \\ &b.) \quad 2\alpha\beta = \omega\mu\sigma \end{aligned} \tag{3-21}$$

By squaring Equations (3-21)a and b and adding them, and then taking the square root, we have

$$\sqrt{(\alpha^2 - B^2)^2 + (2\alpha\beta)^2} = \alpha^2 + \beta^2 = \omega^2\mu\varepsilon\sqrt{1 + \left(\frac{\sigma}{\omega\varepsilon}\right)^2} \tag{3-22}$$

By combining Equations (3-21)a with Equation (3-22),

$$\begin{aligned} &a.) \quad \alpha^2 = \frac{1}{2}\left[-\omega^2\mu\varepsilon + \omega^2\mu\varepsilon\sqrt{1 + \left(\frac{\sigma}{\omega\varepsilon}\right)^2}\right] \\ &b.) \quad \beta^2 = \frac{1}{2}\left[\omega^2\mu\varepsilon + \omega^2\mu\varepsilon\sqrt{1 + \left(\frac{\sigma}{\omega\varepsilon}\right)^2}\right] \end{aligned} \tag{3-23}$$

Therefore,

$$a.)\quad \alpha = \frac{\omega\sqrt{\mu\varepsilon}}{\sqrt{2}}\left[\sqrt{1+\left(\frac{\sigma}{\omega\varepsilon}\right)^2}-1\right]^{1/2}$$
$$b.)\quad \beta = \frac{\omega\sqrt{\mu\varepsilon}}{\sqrt{2}}\left[\sqrt{1+\left(\frac{\sigma}{\omega\varepsilon}\right)^2}+1\right]^{1/2} \qquad (3\text{-}24)$$

By plugging the values of α and β into the real portion of Equation (3-19), the path attenuation can be calculated. [11]

The electromagnetic field also experiences attenuation when it is reflected or transmitted from a scatterer. Conservation of energy requires that the amount of energy going into the intersection must be equal to the amount leaving it. For a electromagnetic field with a normal incidence onto the scatterer, [11]

$$a.)\quad \hat{E}_i + \hat{E}_r = \hat{E}_t$$
$$b.)\quad \frac{\hat{E}_i}{\eta_1} + \frac{\hat{E}_r}{\eta_1} = \frac{\hat{E}_t}{\eta_2} \qquad (3\text{-}25)$$

Combining the above two equations and rearranging yields the reflective coefficient R and the transmission coefficient T: [11]

$$a.)\quad R = \frac{\hat{E}_r}{\hat{E}_i} = \frac{\eta_2 - \eta_1}{\eta_2 + \eta_1}$$
$$b.)\quad T = \frac{\hat{E}_t}{\hat{E}_i} = \frac{2\eta_2}{\eta_2 + \eta_1} \qquad (3\text{-}26)$$

Because the angles of incidence, reflection, and transmission are rarely zero, the index of refraction must be scaled by the angle they make with the normal: [11]

$$a.)\quad R=\frac{\hat{E}_r}{\hat{E}_i}=\frac{\dfrac{\eta_2}{\cos\theta_t}-\dfrac{\eta_1}{\cos\theta_i}}{\dfrac{\eta_2}{\cos\theta_t}+\dfrac{\eta_1}{\cos\theta_i}}=\frac{\eta_2\cos\theta_i-\eta_1\cos\theta_t}{\eta_2\cos\theta_i+\eta_1\cos\theta_t}$$

$$b.)\quad T=\frac{\hat{E}_t}{\hat{E}_i}=\frac{2\eta_2}{\cos\theta_t\left(\dfrac{\eta_2}{\cos\theta_t}+\dfrac{\eta_1}{\cos\theta_i}\right)}=\frac{2\eta_2\cos\theta_i}{\eta_2\cos\theta_i+\eta_1\cos\theta_t} \qquad (3\text{-}27)$$

3.7 Radar

Radar systems make use of the electromagnetic returns reflected from objects to obtain information about their properties and location. By measuring the time delay from the time of transmission to the time of reception of the reflected signal, the range to the target can be calculated. The magnitude of the reflected return contains information about the reflective material properties of the target.

In the simplest radar example, a short duration, single frequency pulse is used as the transmitted signal. The distance to the target can be determined from the amount of time it takes for the pulse to return after being reflected from the target. The amount of power a pulse contains increases as the time duration of the pulse increases. The pulse duration also has an inverse effect on range resolution. Small differences in range cannot be distinguished in a long duration pulse because returns from targets that are close in range will overlap in time. By frequency modulating the transmitted signal, the signal power can be maximized, while not sacrificing range fidelity. [15]

A frequency modulated return signal can be demodulated by downconverting the received signal using the transmitted signal as a reference. After demodulation, returns at different ranges will contribute different range dependant frequency components to the signal. Two return signals that overlap in time will still contribute different frequency components to the downconverted signal. Therefore, a frequency modulated signal can be long in duration, allowing for sufficient power and also allow for precise range resolution.

It is important in radar to have a high fidelity of range resolution, but it is also important to have directional information as well. Knowing the range very precisely does not provide all of the information needed about the location of a target. If only range and no directional information is known, a target could be anywhere within a sphere having a radius of the calculated range. Target directional information can be obtained by having an antenna with a very narrow beam and knowing the direction the antenna is pointing. The resolution of an antenna can be calculated using

$$\delta_{cr} = R\theta_B \tag{3-28}$$

where θ_B is the width of the transmit beam and R is range. The width of an antenna's beam is

$$\theta_B = k\lambda / D \tag{3-29}$$

Where λ is wavelength and D is the antenna width. [15] An antenna with a narrow beam width requires a large diameter. Large diameter antennas can be expensive to build and difficult to transport. An alternative method for obtaining data with high spatial resolution is through synthetic aperture processing. Synthetic aperture radar (SAR) uses

returns from an antenna with a wider beam taken at several locations within an area and integrated to simulate the effect of a smaller beam antenna.

The small beam produced by SAR systems allows for very high resolution returns. The resolution of SAR systems is small enough that the radar can be used to generate pixels in an image. By combining many returns collected by the synthetic aperture at several different angles, a number of pixels can be combined and an image can be generated.

Directional information in a SAR system can be described using two terms: range resolution and cross-range resolution. Range resolution describes resolution in the direction of the main lobe of the antenna. Cross-range resolution describes the direction perpendicular to the main lobe of the antenna. Different SAR processing techniques are able to obtain different range and cross-range resolution.

The assumptions and techniques used in ray-tracing are based upon physical properties of electromagnetic fields. The electromagnetic field, antenna, and radar information discussion in this section provide the theory needed to describe the ray-tracing simulation procedure. The following section will describe the ray-tracing technique and discuss how its implementation mirrors the theory discussed in this section.

4. *Experimental Procedure*

The ray-tracing technique offers an improvement over the existing uniform point scatterer simulator in several areas. The ray-tracing technique is capable of modeling complex three-dimensional faceted targets, while the uniform point scatterer models does not accurately account for three-dimensional effects. Ray-tracing allows targets to have a shadowing effect upon other targets, or on other portions of the same target, an effect that was not modeled in the previous model. Ray-tracing also permits targets to be assigned different dielectric properties and accounts for transmitter directivity, two features not modeled with the uniform point source model.

In using the ray-tracing algorithm, several assumptions were made. First, the electromagnetic wave in the underground environment was assumed to exhibit ray-like characteristics. This assumption requires that the size of the target is large compared to the wavelength and that the effects of diffraction can be disregarded. It was also assumed that the dielectric permittivity was constant within a target and that the magnetic permeability was constant throughout the scene. The effects of dispersion and non-specular reflection were also not modeled.

4.1. Surface Generation

The Rome Labs GPR system was designed to operate in a wide variety of soil conditions and target environments. In order to accurately recreate the target scene, the synthetic scene must be flexible enough to model the varied shapes and material properties of the dielectrics the electromagnetic waves propagate through. The triangular faceted model used by Andrew S. Glassner in *An Introduction to Ray Tracing*

provided the flexibility needed. The contours of the surface of each object in the scene are broken into a series of two-dimensional triangular target facets that cover the surface of the target. The receiver array is modeled using the same triangular target facet technique. This is a very versatile modeling approach, as it can be used to model both highly textured targets and relatively flat ones.[6]

Each of the triangular target facets that make up the surface of an object are specified by three target facet points that lie within a plane. This plane is referred to as the target plane and can be expressed by the following equation:

$$Ax + By + Cz + D = 0 \tag{4-1}$$

Where A,B,C and D are constants, and x,y, and z represent all Cartesian points in the plane.

The target plane equation can be found by taking the cross product of the lines that make up two of the legs of the triangular target facets of interest. This will give the A, B, and C constants of the equation. The D constant can then be solved for by plugging the Cartesian coordinates of one of the points in the target plane into the x, y and z variables of Equation (4-1) and solving for D. [6] In this simulation, one of the target facet points was used as this point. The [A B C] values of the target plane equation also describe the x,y, and z unit directional coordinates of a vector that is normal to the target plane.

All of the information associated with the targets is stored in a three dimensional matrix. This includes the dielectric constant of the medium outside of the target (ε outside), the dielectric constant of the medium within the surface of the target object (ε

inside), the x, y and z coordinates of the points in the target facet, and the A, B, C and D constants of the plane equation. The A, B, and C coordinates of the plane are normalized so the magnitude of the line normal to the target plane will be 1. The matrix dimensions are Nx3x5, where N is the number of target facets. The first two target facets in the array (N = 1,2) are used to designate the receiver array. For each target facet, there is a 3x5 two-dimensional matrix containing the following information:

	1	2	3
1	Point 1 X	Point 1 Y	Point 1 Z
2	Point 2 X	Point 2 Y	Point 2 Z
3	Point 3 X	Point 3 Y	Point 3 Z
4	A value	B value	C value
5	D value	ε outside	ε inside

Table 4.1: Facet data table

4.2. Ray Generation

Glassner demonstrated a ray modeling technique that breaks down rays into line equations in the X, Y, and Z directions, given their initial position and a direction unit vector. The rays are characterized by Equations (4-2)a-c.[6]

$$\begin{aligned} &\text{a. } X(t) = X_0 + X_d t \\ &\text{b. } Y(t) = Y_0 + Y_d t \\ &\text{c. } Z(t) = Z_0 + Z_d t \end{aligned} \tag{4-2}$$

Where X(t), Y(t) and Z(t) represent the position of the ray at a given time, X_0, Y_0, and Z_0 represent the origin of the ray in Cartesian coordinates, X_d, Y_d, and Z_d represent the direction unit vector of the ray and t = distance traveled. At t = 0, the ray originates at the

point (X_0,Y_0,Z_0). As t increases, the ray is extended in the X, Y, and Z direction according to Equations (4-2) a-c.

Transmitters operating in the near field can be modeled using rays that originate at the transmitter location and extend radially away from it.[8] Therefore, the transmitter coordinates are selected as the ray origin point and the direction unit vector are selected to create rays that extend away from the origin. The direction unit vectors of the transmitted rays are converted from the polar coordinate inputs provided by the user to the Cartesian coordinate system. The azimuth angle θ, and the declination angle, Φ describe the direction of the center ray. The azimuth and declination spreading angles, ψ_a and ψ_d describe the spread of the rays in the azimuth and declination direction (see Figure 4.1). The number of rays in the azimuth and declination directions is also specified. The polar coordinates of the ray direction are then converted into the Cartesian coordinates system and the origin (X_0,Y_0,Z_0) and direction components (X_d,Y_d,Z_d) of the ray are saved in the ray queue.

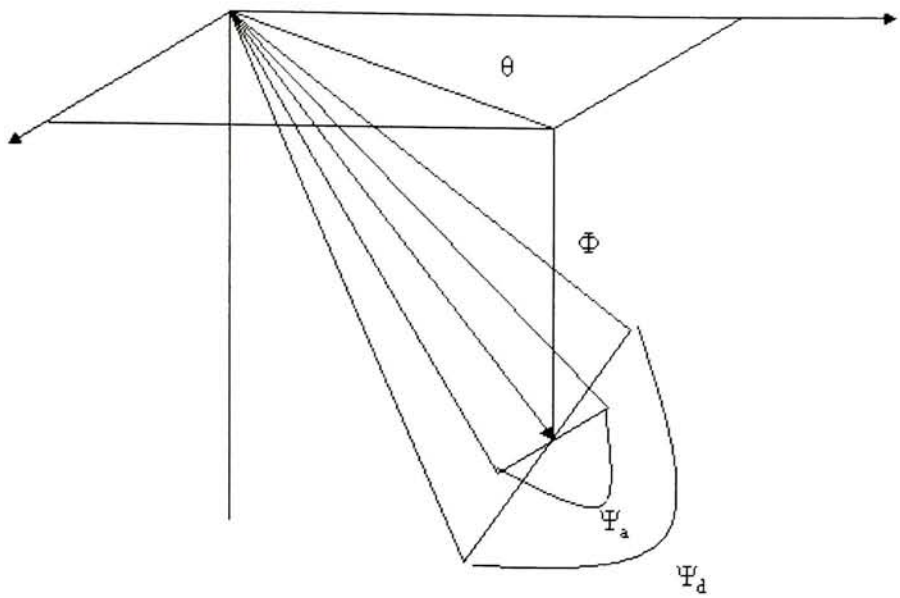

Figure 4.1 Transmitted Ray Orientation

4.3. Intersection Detection

After the target has been defined and the direction of the rays has been calculated, the software detects whether the rays intersect with the target. Each ray must be compared against each triangular facet of the target model to determine if the ray intersects with the plane of the target facet. If the ray intersects with the target facet plane, it must be determined if the point where the ray intersects the plane is within the boundaries of the target facet. Glassner describes a technique for doing this by solving Equations (4-2)a-c for each of the plane equations for the triangular target facets of the target. This equation is then solved for the variable t, the distance of propagation.

For a ray described by the equations

$$X(t) = X_0 + X_d t$$
$$Y(t) = Y_0 + Y_d t \qquad (4\text{-}3)$$
$$Z(t) = Z_0 + Z_d t$$

and a triangular target facet described by the plane equation

$$Ax + By + Cz + D = 0 \qquad (4\text{-}4)$$

which has been normalized such that

$$A^2 + B^2 + C^2 = 1 \qquad (4\text{-}5)$$

Equations(4-3)a-c can be substituted into the x, y and z variables of Equation (4-4). This results in a plane equation as a function of t:

$$A(X_0 + X_d t) + B(Y_0 + Y_d t) + C(Z_0 + Z_d t) + D = 0 \qquad (4\text{-}6)$$

Equation (4-6) can be solved for t. [6]

$$t = \frac{-(AX_0 + BY_0 + CZ_0 + D)}{AX_d + BY_d + CZ_d} \qquad (4\text{-}7)$$

Equation (4-7) can be expressed more efficiently by using vector notation. As discussed before, a vector having the direction components [A B C] is normal to the target plane of interest. This normalized unit vector will be referred to as $\mathbf{P_n}$. The origin of the X,Y, and Z components of the ray, [X_0 Y_0 Z_0] will be defined as $\mathbf{R_0}$. $\mathbf{R_d}$ will be used to define the X,Y, and Z direction components of the ray, [X_d Y_d Z_d]. Equation (4-7) can be expressed in vector notation as

$$t = \frac{-(\mathbf{P_n} \cdot \mathbf{R_0} + D)}{\mathbf{P_n} \cdot \mathbf{R_d}} \qquad (4\text{-}8)$$

If the value calculated for t is greater than zero, then the ray intersects the target plane. If t is less than zero, then the ray intersects prior to its origin, and it should be counted as

non-intersecting. If the t value calculated using Equation (4-8) is positive, the coordinates of the ray's intersection with the plane (R_i) can be calculated by substituting t into Equation (4-3)a-c and arranging the result into the vector $\mathbf{R_i}$= [Xi Yi Zi][6]

$$\mathbf{R}_i = [X_0 + X_d t \quad Y_0 + Y_d t \quad Z_0 + Z_d t] \tag{4-9}$$

After the coordinates of the ray's intersection with the target plane have been calculated, it must be determined whether the intersection coordinates are within the target facet. We will refer to a ray-target facet intersection where the intersection coordinates are within the target facet as a valid intersection. The technique Glassner uses to determine if a valid intersection occurs requires the triangular target facet in question to be collapsed into two dimensions. (See Figure 4.2)

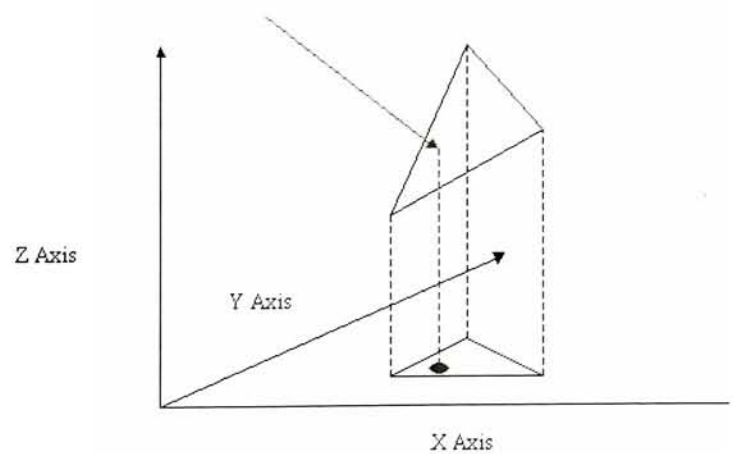

Figure 4.2- Collapsed Facet Diagram

If the intersection coordinates are within the target facet, they will also be within the two dimensional projection of the facet. If the three target points share common values in the dimension that the facet is collapsed in, the target facet collapses to a line

and it is impossible to determine if the intersection is within the facet. For instance, a vertically oriented target cannot be collapsed to a plane parallel to the ground. To prevent this, the collapsed dimension is selected such that the coordinates of the collapsed dimension are not the same for all three target points in the target facet. The three sides that make up the collapsed facet will be referred to as the facet boundary lines (see Figure 4.3).

To determine if a valid intersection occurred, a line is traced within the collapsed facet in a single direction away from the intersection coordinates, R_i. This line will be referred to as the intersection determination line. If the intersection determination line crosses only one facet boundary line of the collapsed facet projection, then the intersection coordinates can be considered within the target facet and the intersection can be ruled valid. If the intersection determination line crosses zero or two facet boundary lines, then the intersection coordinates are outside of the target facet and the intersection is ruled invalid. (see Figure 4.3) In order to avoid ambiguities that may occur if the intersection determination line crosses the vertex between two sides of the target facet, the intersection determination line is traced parallel to one of the facet boundary lines.

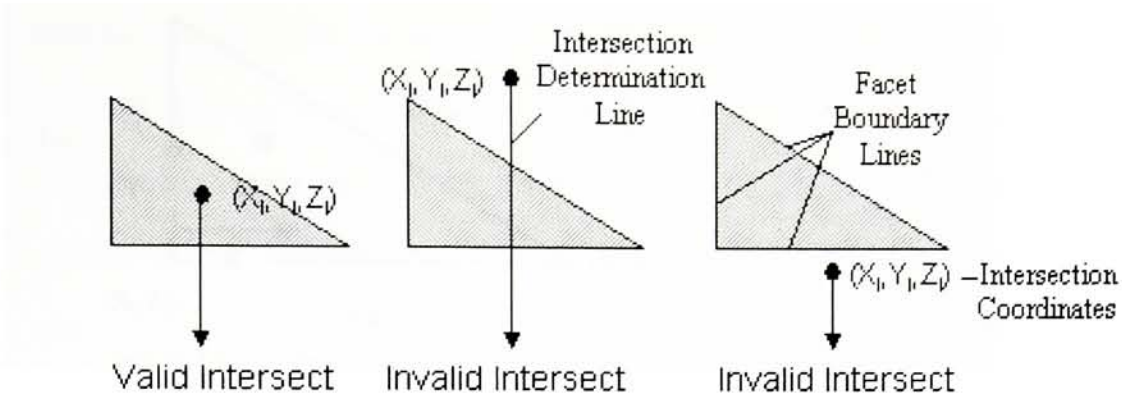

Figure 4.3 Valid Intersection Determination

The following example describes a valid intersection determination. The three vertices of the target facet are defined as:

$$\begin{aligned}(X_1,Y_1,Z_1)\\(X_2,Y_2,Z_2)\\(X_3,Y_3,Z_3)\end{aligned} \tag{4-10}$$

The ray/target plane intersection coordinates, which were calculated using Equation (4-9) are defined as

$$(X_i,Y_i,Z_i) \tag{4-11}$$

For this example, the target is assumed to be collapsed in the Z direction. Therefore, the Z dimension can be neglected in the valid intersection determination. The projection in the X and Y dimensions is pictured in Figure 4.4.

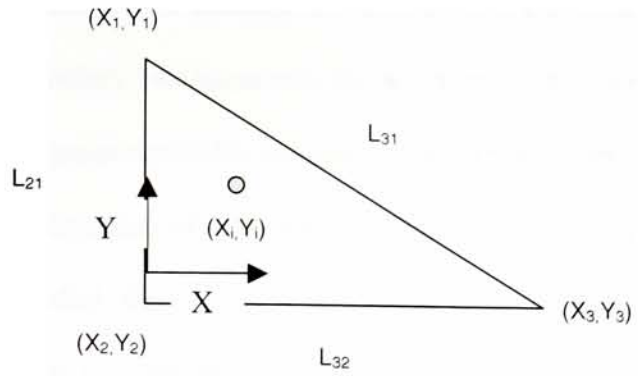

Figure 4.4 Projected Facet In X-Y Dimension

The X and Y components of the facet boundary lines can be written in terms of the vertices using the following line equations:

$$
\begin{aligned}
&a.) \quad L_{31X}(u) = X_3 + (X_3 - X_1)u \\
&b.) \quad L_{31Y}(u) = Y_3 + (Y_3 - Y_1)u \\
&c.) \quad L_{21X}(u) = X_2 + (X_2 - X_1)u \\
&d.) \quad L_{21Y}(u) = Y_2 + (Y_2 - Y_1)u \\
&e.) \quad L_{32X}(u) = X_3 + (X_3 - X_2)u \\
&f.) \quad L_{32Y}(u) = Y_3 + (Y_3 - Y_2)u
\end{aligned}
\tag{4-12}
$$

Where u is a linearly increasing function from zero to infinity. Equations (4-12)a-f are linear equations that have their origin at the facet boundary line vertices and a direction component defined by the difference between the two end points of the facet boundary line. In this example, the intersection determination line will be traced parallel to line L_{32}. Therefore, the X and Y components of the intersection determination line's slope will be equal to that of L_{32X} and L_{32Y}. The X and Y line equations of the intersection determination line are:

$$
\begin{aligned}
&a.) \quad L_{iX}(t) = X_i + (X_3 - X_2)t \\
&b.) \quad L_{iY}(t) = Y_i + (Y_3 - Y_2)t
\end{aligned}
\tag{4-13}
$$

Where t is a linearly increasing function from zero to infinity. Similar to the facet boundary line equations, the intersection determination line equations contain an origin at the point where the ray intersects the target facet plane and a direction component parallel to Equation (4-12)e and f. Because line L_{32} and the intersection determination line are parallel, the two lines will never cross. Therefore, it is only necessary to determine if lines L_{31} and line L_{21} crosses the intersection determination line. To determine if the intersection determination line crosses the facet boundary lines, the intersection determination and facet boundary line equations are set equal to each other:

$$\begin{aligned} &a.) \quad X_i + (X_3 - X_2)t = X_3 + (X_3 - X_1)u \\ &b.) \quad Y_i + (Y_3 - Y_2)t = Y_3 + (Y_3 - Y_1)u \\ &c.) \quad X_i + (X_3 - X_2)t = X_2 + (X_2 - X_1)u \\ &d.) \quad Y_i + (Y_3 - Y_2)t = Y_2 + (Y_2 - Y_1)u \end{aligned} \tag{4-14}$$

After rearranging, Equations (4-14)a-d can be written in the form:

$$\begin{aligned} &a.) \quad X_i - X_3 = -(X_3 - X_2)t + (X_3 - X_1)u \\ &b.) \quad Y_i - Y_3 = -(Y_3 - Y_2)t + (Y_3 - Y_1)u \\ &c.) \quad X_i - X_2 = -(X_3 - X_2)t + (X_2 - X_1)u \\ &d.) \quad Y_i - Y_2 = -(Y_3 - Y_2)t + (Y_2 - Y_1)u \end{aligned} \tag{4-15}$$

Equations (4-15)a-d can be expressed in vector notation

$$\begin{aligned} &a.) \quad \begin{bmatrix} -(X_3 - X_2) & (X_3 - X_1) \\ -(Y_3 - Y_2) & (Y_3 - Y_1) \end{bmatrix} \begin{bmatrix} t \\ u \end{bmatrix} = \begin{bmatrix} (X_i - X_2) \\ (Y_i - Y_2) \end{bmatrix} \\ &b.) \quad \begin{bmatrix} -(X_3 - X_2) & (X_2 - X_1) \\ -(Y_3 - Y_2) & (Y_2 - Y_1) \end{bmatrix} \begin{bmatrix} t \\ u \end{bmatrix} = \begin{bmatrix} (X_i - X_2) \\ (Y_i - Y_2) \end{bmatrix} \end{aligned} \tag{4-16}$$

Equation (4-16)a and b can be solved by premultiplying both sides of the equation by the inverse of the leftmost bracketed expression. This expression is forced to be invertible because the target facet is collapsed in a dimension where all of the X, Y or Z values are

not the same. If the determinate of the matrix is determined to be zero, an infinitesimal amount is added to allow the calculation. The values of t and u are the products of premultiplication. The t and u values represent the distance that the intersection determination line and the line defining the sides of the target facet travel before they cross.

The next step is to count the number of times the intersection determination line crosses the facet boundary lines and determine if the intersection coordinates truly lie within the target facet. To get a positive count, two criteria must be verified. First, the value of t must be greater than zero to ensure that the intersection determination line was only traced in one direction.

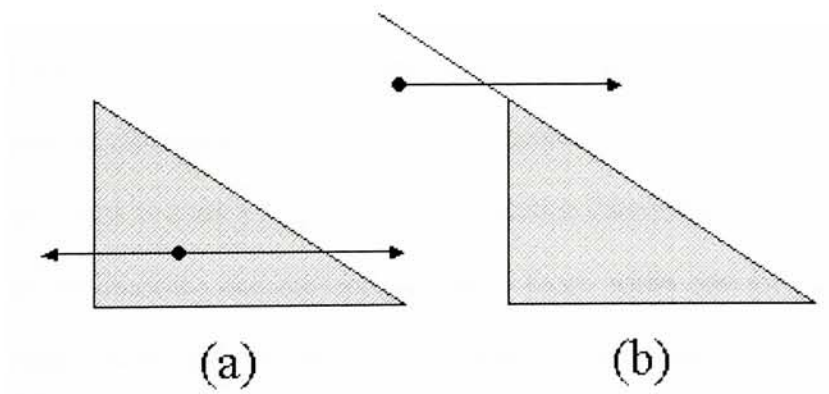

Figure 4.5(a+b) Invalid Intersection Determination Line Examples

If it was traced in both the positive and negative direction, extraneous intersections may be counted (See Figure 4.5a.). Second, the value of u must be between one and zero. Any two lines in a plane that are not parallel will cross at some point in the plane. The

crossing point must be within the boundaries of the target facet boundary line (see Figure 4.5b). In defining the boundary lines of the target facet, the slope of the line was calculated by subtracting the vertex points of the sides (See Equation (4-12)a-f). By defining the slope this way, if the intersection determination line crosses within the facet boundary line, it will have a value of u between one and zero. Take, for example, Equation (4-17):

$$\begin{aligned} a.) \quad & L_{31X}(u) = X_3 + (X_3 - X_1)u \\ b.) \quad & L_{31Y}(u) = Y_3 + (Y_3 - Y_1)u \end{aligned} \tag{4-17}$$

If u = 0, then the equation is equal to the origin, one of the extremes of the target boundary line. If u = 1, then the equation is equal to $X_3+(X_3-X_1)$, which is equal to the X coordinates of the vertex at the other end of the target facet boundary line.

Using the criteria described above, the number of crossings between the intersection determination line and the target facet boundaries are counted. This information is used to determine if the ray/target intersection is valid. Zero or two crosses of the target facet boundary lines and the intersection determination line represent an invalid intersection between the ray and the target facet, while one crossing of the target facet boundary lines and the intersection determination line represent a valid intersection between the ray and the target facet. [6]

It is possible for a single ray to intersect with several target facets, or no target facets at all. Therefore, for each ray, the ray/target facet intersection test must be performed on every target facet, regardless of whether the ray has had previous intersections. The distance the ray travels to each intersecting target facet is then logged.

If the ray does not intersect with any target facets, then that ray is discarded. If the ray intersected with several target facets, the target facet with the shortest distance traveled by the ray corresponds to the valid target facet intersection.

The intersection of rays with the receiver array represents a special case of the standard target intersection determination. The receiver array is assigned target facet numbers 1 and 2. If a ray intersects with one of these facets, the intersection coordinates are logged. The scene coordinates are oriented parallel to the sides of the receiver array, so the receiver array and the scene coordinates can be expressed on the same axes. If the dimensions and location of the receivers within the receiver array are known, the rays can be grouped by individual receiver based upon a linear transformation between the ray's intersection coordinates and the relative receiver positions in the receiver array.

4.4 Reflected and Transmitted Ray Calculation

After it has been determined that a ray has made a valid intersection with a target facet, a new ray is generated and logged in the ray queue with an origin at the intersection coordinates and directional components in the direction of a reflected ray. If applicable, another ray representing the transmitted component of the original ray is generated and added to the ray queue. The next step in the modeling process is to compute the direction component of the newly formed reflected and transmitted ray. Glassner's technique for calculating the reflected and transmitted direction components involves the use of the Law of Reflection and Snell's Law.

The Law of Reflection states that the angle that an incident ray makes with a line normal to the surface of the target facet and the angle the reflected ray makes with the

same normal line are equal. (See Figure 4.6) To use the Law of Reflection, information about the direction and origin of the normal line and incident ray is needed. In our case, the incident ray direction equation and origin points are known, and the normal line is described by the vector [A B C]. The direction components of the normal line in the X, Y, and Z coordinates are equal to the normalized A, B, and C coordinates of the plane equation calculated in Equation (4-1). The origin of the normal line is the target facet intersection coordinates. The normal line and the incident ray must be on the same side of the target facet. To verify this, the dot product of the incident ray and the normal line is taken. If the answer is negative, the direction of the normal line must be reversed.

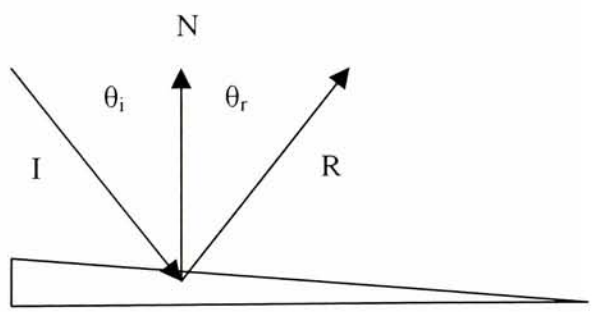

Figure 4.6 Law of Reflection

Two rules of physical optics will be used to determine the equation of the reflected ray. First, because the incident ray, I, the normal line, N, and the reflected ray, R are all in the same plane, R is a linear combination of I and N [6]. The equation for R can therefore be written as

$$R = \alpha I + \beta N \tag{4-18}$$

where α and β are linear functions. Second, the law of reflection states that the incident angle is equal to the reflected angle, $\theta_i = \theta_r$.

Taking the cosine of θ_i will give the projection of the incident ray along the normal. The cosine of θ_r will give the projection of the reflected ray along the normal direction. This can be expressed as a dot product in the following format:

$$\begin{aligned} &a.) \quad \cos(\theta_r) = -I \cdot N \\ &b.) \quad \cos(\theta_i) = N \cdot R \end{aligned} \tag{4-19}$$

The negative of I is used because the vectors must be arranged tail to tail to perform the dot product. Because $\theta_i = \theta_r$ it is also true that $\cos(\theta_i) = \cos(\theta_r)$. Therefore, Equations (4-19) a and b can be set equal to each other.

$$-I \cdot N = N \cdot R \tag{4-20}$$

By substituting the equation for the reflected ray, $R = \alpha I + \beta N$ into Equation (4-20), it can be rewritten as

$$-I \cdot N = N \cdot (\alpha I + \beta N) \tag{4-21}$$

After distribution,

$$-I \cdot N = \alpha(N \cdot I) + \beta(N \cdot N) \tag{4-22}$$

Because the normal vector was normalized to a magnitude of 1, N·N is equal to 1.

$$-I \cdot N = \alpha(N \cdot I) + \beta \tag{4-23}$$

Equation (4-23) is a function of two variables, α and β, so we can arbitrarily set α to 1 and solve the equation in terms of β. Leaving

$$\beta = -2(N \cdot I) \tag{4-24}$$

Equation (4-24) can be substituted into Equation (4-18)

$$R = I - 2(N \cdot I)N \tag{4-25}$$

Equation (4-25) is used to calculate the equation of the reflected ray.[6]

Similar to the approach used to calculate the reflected ray, Glassner's technique uses physical laws to calculate the direction component of the transmitted ray. The first physical law is Snell's law, which states that the incident and transmitted angles are related by the following equation:

$$\eta_i \sin(\theta_i) = \eta_t \sin(\theta_t) \tag{4-26}$$

Where η_i is the index of refraction of the incident medium and η_t is the index of refraction of the refractive medium. (See Figure 4.7)

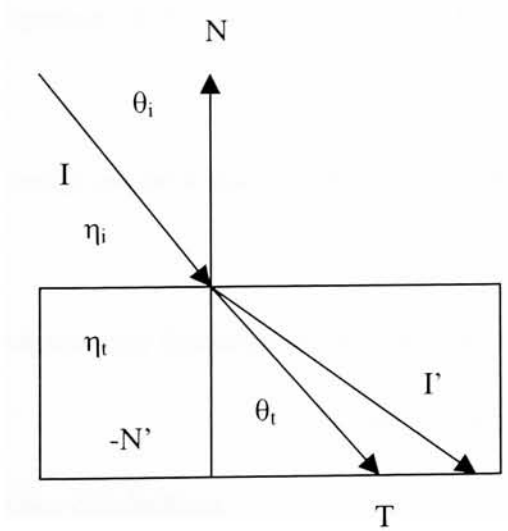

Figure 4.7 Transmitted Ray Calculation Diagram

For the calculation of the transmitted ray, it is useful to use Snell's law in the following format:

$$\frac{\sin(\theta_t)}{\sin(\theta_i)} = \frac{\eta_i}{\eta_t} = \eta_{it} \tag{4-27}$$

The second physical law used in determining the direction components of T is the fact that, similar to the reflected ray, the transmitted ray is in the plane of the incident ray. Therefore, the transmitted ray can be expressed linearly in terms of the incident ray, I and the normal line, N:

$$T = \alpha I + \beta N \tag{4-28}$$

Equation (4-27) can be rearranged and both sides squared, leaving:

$$\sin^2(\theta_t) = \eta_{it}^{\ 2} \sin^2(\theta_i) \tag{4-29}$$

Because $\sin^2(\theta)+\cos^2(\theta)=1$, Equation (4-29) can be rewritten

$$[1-\cos^2(\theta_i)]\eta_{it}^{\ 2} = [1-\cos^2(\theta_t)] \tag{4-30}$$

Equation (4-30) can be rewritten in the form

$$[1-\cos^2(\theta_i)]\eta_{it}^{\ 2} - 1 = -\cos^2(\theta_t) \tag{4-31}$$

$\cos(\theta_t)$ can be written in vector form, leaving:

$$[1-\cos^2(\theta_i)]\eta_{it}^{\ 2} - 1 = -[-N \cdot T] \tag{4-32}$$

Substituting Equation (4-28) into Equation (4-32) yields

$$[1-\cos^2(\theta_i)]\eta_{it}^{\ 2} - 1 = -[-N \cdot (\alpha I + \beta N)]^2 \tag{4-33}$$

After distribution,

$$[1-\cos^2(\theta_i)]\eta_{it}^{\ 2} - 1 = -[\alpha(-N \cdot I) + \beta(-N \cdot N)]^2 \tag{4-34}$$

Because N was normalized to a magnitude of 1, Equation (4-34) can be rewritten as

$$[1-\cos^2(\theta_i)]\eta_{it}^{\ 2} - 1 = -[\alpha\cos(\theta_i) - \beta]^2 \tag{4-35}$$

The transmitted ray direction vector should have a magnitude of 1, so

$$1 = T \cdot T \tag{4-36}$$

Substituting Equation (4-28), yields

$$\begin{aligned} a.)\quad & 1 = (\alpha I + \beta N)\cdot(\alpha I + \beta N) \\ b.)\quad & 1 = \alpha^2 (I \cdot I) + 2\alpha\beta (I \cdot N) + \beta^2 (N \cdot N) \\ c.)\quad & 1 = \alpha^2 - 2\alpha\beta\cos(\theta_i) + \beta^2 \end{aligned} \tag{4-37}$$

By solving Equations (4-37)c and Equation (4-35) simultaneously for α and β, and then plugging into Equation (4-28), we find the equation for the direction vector of the transmitted ray T to be [6]

$$T = \eta_{it} I + (\eta_{it}\cos(\theta_i) - \sqrt{(1+\eta_{it}^2(\cos^2(\theta_i)-1))}N \tag{4-38}$$

The indices of refraction of the objects in the scene are defined by two variables associated with each facet, the index of refraction inside of the closed target and the index of refraction outside of the target. It is therefore necessary to count the number of transmissions to determine if the ray is currently inside of the target or outside of the target. If an odd number of transmissions have occurred, the ray is inside of the target. If an even number or zero transmissions have occurred, then the ray is outside of the target. If the ray is determined to be inside of the target, the indices of refraction are reversed, so that the value originally used as the incident index of refraction is now the transmitted value and vice versa.

4.5 Attenuation

As discussed in Section 3.7, an electromagnetic wave attenuates as it propagates through a dielectric medium. The ray-tracing simulator assigns a magnitude to each initial ray sent from the transmitter. The attenuation is a function of the path distance traveled by the wave, the number of reflections and transmissions the wave is subjected

to, and the dielectric properties of the medium. The path distance attenuation is calculated every time a ray intersects with a facet. The equation defining the attenuation of the rays due to path length through the medium is

$$E = E_0 e^{\alpha t} \tag{4-39}$$

Where E_0 is the original magnitude of the electromagnetic field, t is the distance of propagation, and α is the attenuation function defined as

$$\alpha = \frac{\omega\sqrt{\mu\varepsilon}}{\sqrt{2}}\left[\sqrt{1+\left(\frac{\sigma}{\omega\varepsilon}\right)^2}-1\right]^{1/2} \tag{4-40}$$

The attenuation caused by reflection and transmission are quantified by Equations (4-41, a and b).[16]

$$\begin{aligned} a.\quad & R = \frac{\mu_2 k_1 \cos\theta_i - \mu_1\sqrt{k_2^2 - k_1^2\sin^2\theta_i}}{\mu_2 k_1 \cos\theta_i + \mu_1\sqrt{k_2^2 - k_1^2\sin^2\theta_i}} \\ b.\quad & T = \frac{2\mu_2 k_1 k_2 \cos\theta_i}{\mu_2 k_1 \cos\theta_i + \mu_1\sqrt{k_2^2 - k_1^2\sin^2\theta_i}} \end{aligned} \tag{4-41}$$

The initial magnitude of the reflected and transmitted rays is calculated by applying Equation (4-41)a to the magnitude of the reflected ray and Equation (4-41)b to the magnitude of the transmitted ray. The cumulative effects of the path length attenuation for the reflected and transmitted rays are applied on an intersection by intersection basis. If the magnitude of the incident ray falls below a user-defined level, additional reflected and transmitted rays will no longer be generated.

4.6. Synthetic Return Generation

The total path distance associated with a given ray can be calculated by adding the cumulative path lengths of the initial ray and each of its subsequent reflected and transmitted legs. This process is continued until the ray intersects the receiver array or is attenuated below the user defined level. From the total path distance, the simulated return signal can be generated using Equation (4-42)

$$r(t) = \mathrm{Re}[e^{j\theta}]$$
$$\theta = -2\pi\tau\sqrt{\mu\varepsilon}\,(f_c + \gamma t) + \pi\gamma\left(\tau\sqrt{\mu\varepsilon}\right)^2 \tag{4-42}$$

Where γ is the chirp rate, f_c is the start frequency of the chirp, τ is the path length, and t is time. The origin of this equation will be discussed in greater detail in Section 5.4. The simulated return for a given receiver location is generated by adding the simulated return from each ray that intersects that receiver location.

4.7. Automatic Ray Generation

For a ray-tracing model to accurately represent a transmitting antenna, the ray origin, direction and magnitude variables must be chosen carefully. If none of the transmitted rays are reflected to the receiver array, there is no information associated with the return. The ideal image is created when each of the receiver locations receive at least one ray. In practicality, this is subject to the antenna beam pattern, the size of the target, and the depth of the target. In order to get an idea of the best possible image, we needed a way to guarantee that each receiver would receive a ray. To do this, we needed to calculate the ray's direction unit vector, and calculate new dimensions for the target to ensure that each receiver receives a specularly reflected ray. (see Figure 4.8)

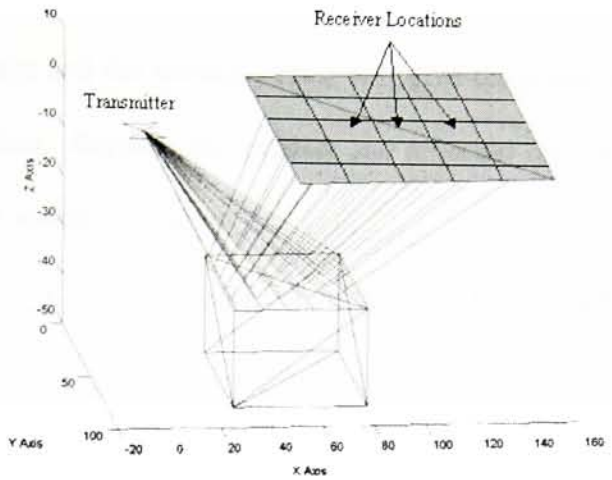

Figure 4.8 Automatic Ray Generation Example

The available information is:

$[X_R Y_R Z_R]$ - Receiver coordinates
[A B C D] - Target plane equation coefficient
$[X_T Y_T Z_T]$ - Transmitter coordinates

The variables that must be solved for are:

$[X_p Y_p Z_p]$ - Intersection coordinates
k - scaling factor

Applying Equation (4-1), the target facet plane equation to the unknown intersection coordinates, we have

$$AX_p + BY_p + CZ_p + D = 0 \tag{4-43}$$

Subtracting the intersection coordinates from the transmitter coordinates gives a direction vector of the transmitter to intersection point ray. The reflected ray direction vector can be calculated by subtracting the intersection coordinates from the receiver location. The Law of Reflection states that the angle made by the incident and normal vector is the

same as the angle made by the reflected and normal vector. The dot product of the incident and reflected rays and the normal vector will give the projection of the rays in the normal vector direction. Because the incident and reflected rays are not normalized, the dot products must be scaled by a factor, k.

$$A(X_R - X_p) + B(Y_R - Y_p) + C(Z_R - Z_p) = k\left[A(X_T - X_p) + B(Y_T - Y_p) + C(Z_T - Z_p)\right] \tag{4-44}$$

Factoring Equation (4-44) and combining,

$$AX_R - AX_p + BY_R - BY_p + CZ_R - CZ_p = kAX_T - kAX_p + kBY_T - kBY_p + kCZ_T - kCZ_p$$

$$(kAX_p - AX_p) + (kBY_p - BY_p) + (kCZ_p - CZ_p) = -AX_R - BY_R - CZ_R + kAX_T + kBY_T + kCZ_T$$

$$AX_p(k-1) + BY_p(k-1) + CZ_p(k-1) = k(CZ_T + BY_T + AX_T) - AX_R - BY_R - CZ_R$$

$$(k-1)(AX_p + BY_p + CZ_p) = (k[A\ B\ C]\cdot[X_TY_TZ_T] - [A\ B\ C]\cdot[X_RY_RZ_R]) \tag{4-45}$$

By substituting Equation (4-43),

$$(k-1)(-D) = (k[A\ B\ C]\cdot[X_TY_TZ_T] - [A\ B\ C]\cdot[X_RY_RZ_R])$$

$$(k-1)(-D) - k([A\ B\ C]\cdot[X_TY_TZ_T]) = -[A\ B\ C]\cdot[X_RY_RZ_R]$$

$$D - kD - k([A\ B\ C]\cdot[X_TY_TZ_T]) = -[A\ B\ C]\cdot[X_RY_RZ_R]$$

$$k(-D - [A\ B\ C]\cdot[X_TY_TZ_T]) = -D - [A\ B\ C]\cdot[X_RY_RZ_R]$$

$$k = \frac{D + [A\ B\ C]\cdot[X_RY_RZ_R]}{D + [A\ B\ C]\cdot[X_TY_TZ_T]} \tag{4-46}$$

By substituting $R = I - 2(N\cdot I)N$

$$(X_p - X_T) - 2[A(X_p - X_T) + B(Y_p - Y_T) + C(Z_p - Z_T)]A = k(X_R - X_p)$$

$$(Y_p - Y_T) - 2[A(X_p - X_T) + B(Y_p - Y_T) + C(Z_p - Z_T)]B = k(Y_R - Y_p)$$

$$(Z_p - Z_T) - 2[A(X_p - X_T) + B(Y_p - Y_T) + C(Z_p - Z_T)]C = k(Z_R - Z_p) \quad (4\text{-}47)$$

X_p, Y_p, and Z_p are then solved for using the Matlab polynomial solver. These values are calculated for each receiver location.

This section described the ray-tracing procedure used in the simulation. This specific implementation was designed to generate a simulated received signal to be used with the ground penetrating radar system developed by Rome Labs. The GPR system interprets this signal and uses it to generate an image of the scene. In the following section, the Rome Labs system will be described in detail and the image formation technique will be discussed.

5. *Description of System*

The simulator described in this thesis was designed to be used with a GPR image formation processor developed by Rome Labs, which will be described in this chapter. The Rome Labs system combines the principles of synthetic aperture and ground penetrating radar and was designed for deep soil penetration. The system uses a bow-tie transmit antenna to transmit a linearly chirped signal into an underground medium. The returns are measured at several locations within a receiver array grid using another bow-tie antenna. By aligning the returns measured at each receiver location in range and adding them coherently, an image of the underground scene can be generated. (See Figure 5.1)

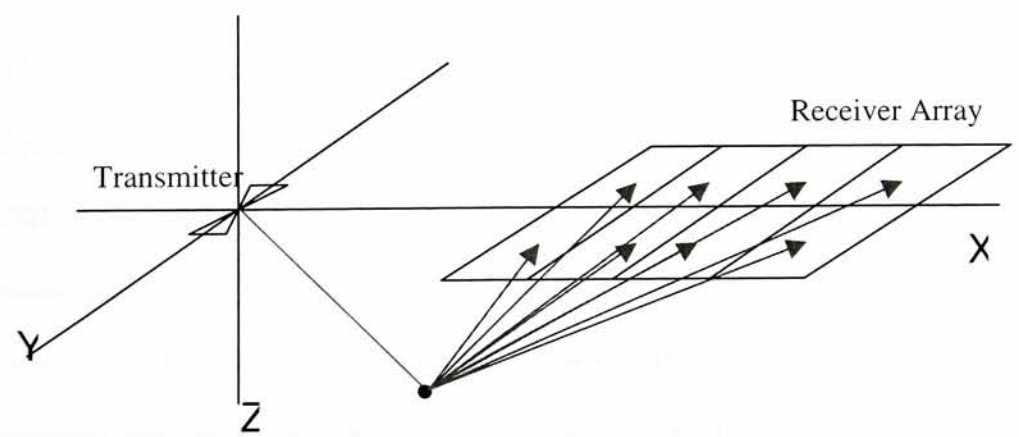

Figure 5.1 Rome Labs GPR Configuration

5.1. Transmission and Reception

Figure 5.2 is a block diagram representation of the Rome labs transmitter and receiver system.

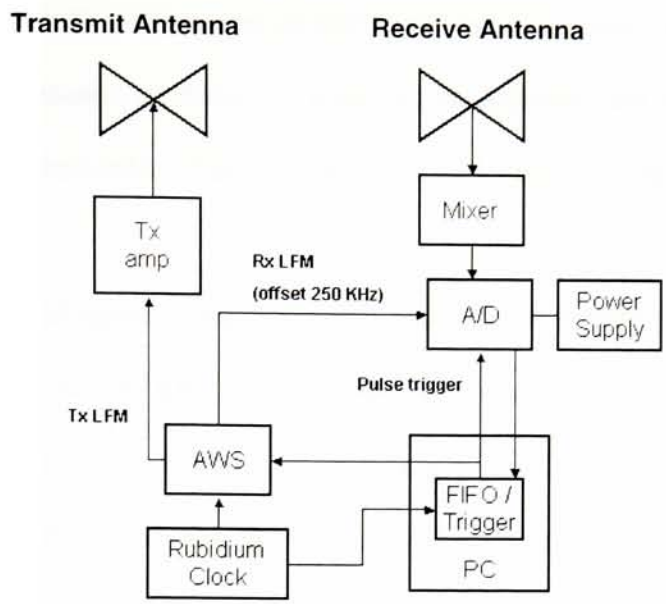

Figure 5.2 Rome Labs Transmitter and Receiver System

The Rome labs system uses a linear frequency modulated continuous wave waveform. This allows for accurate timing and control, while providing low peak power and high dynamic range. [22] The signal is down-ramp linear frequency modulated from 66 to 6 MHz over 2 milliseconds. The frequency range was selected to achieve the desired 3 ft resolution and avoid attenuation associated with the 160 ft maximum depth of ground penetration. [22] The pulse is triggered by a first in, first out (FIFO) trigger through the personal computer. The waveform is generated by an arbitrary waveform synthesizer and amplified to 10 watts, as shown schematically in Figure 5.1. A linear weighting function is applied at the waveform synthesizer to account for attenuation variations at different frequencies and ensure a level transmitted signal.

The signal is transmitted by a 22 ft by 5 ft bow-tie antenna. The bow-tie antenna was selected because it is wideband, directive, planar, efficient, and easily fabricated

[22]. The antennas are constructed of half-inch aluminum pipes and Plexiglas and rest directly on the ground. A balun is added to the antenna and adjusted to match the impedance of the feed cable. The receiver is a smaller bow-tie antenna, of dimensions 14 ft by 3 ft.

The received signal is demodulated by mixing it with a reference waveform that is offset in frequency by 250 KHz. The reference and transmitted signals are both generated by the arbitrary waveform synthesizer and triggered by the same FIFO trigger, ensuring that the reference waveform and the transmitted waveform are coherent. The output of the mixer is a signal containing a number of frequency components that are range dependent. Each frequency component contained in the dechirped signal corresponds to a return from a different scatterer in the scene. Mixing the received signal with a frequency offset reference downconverts the signal to an intermediate frequency.

The analog dechirped signal is converted into a discrete signal using a 16-bit analog to digital converter with a 1 MHz sample rate. The digital dechirped signal is then interfaced into the personal computer.

To obtain data from the entire data grid, the receive antenna is moved to each point in the receiver array grid. At each point, 2000 pulse samples are received and averaged in the personal computer. The location of each receiver location relative to the transmitter is measured and recorded using surveying equipment. After the averaged return signal has been input into the computer, it is saved in a file that corresponds to each receiver location. The relative position of each of the receiver locations is saved to a file as well. This information is input into a GUI program developed by Rome labs to

perform the processing and generate an image of the scene. The GUI program can be broken into two stages, the pre-processing stage, and the SAR processing stage.

5.2. Pre-Processing

After the input signal has been demodulated, each receiver location contains data that is composed of distance dependant frequency components. Each of the frequency components that comprise the demodulated signal correspond to a return from a different scatterer in the scene. The objective of the pre-processing stage is to subject the demodulated input data to several layers of signal processing to correct for undesired effects. The block diagram of the pre-processing stage is shown as Figure 5.3.

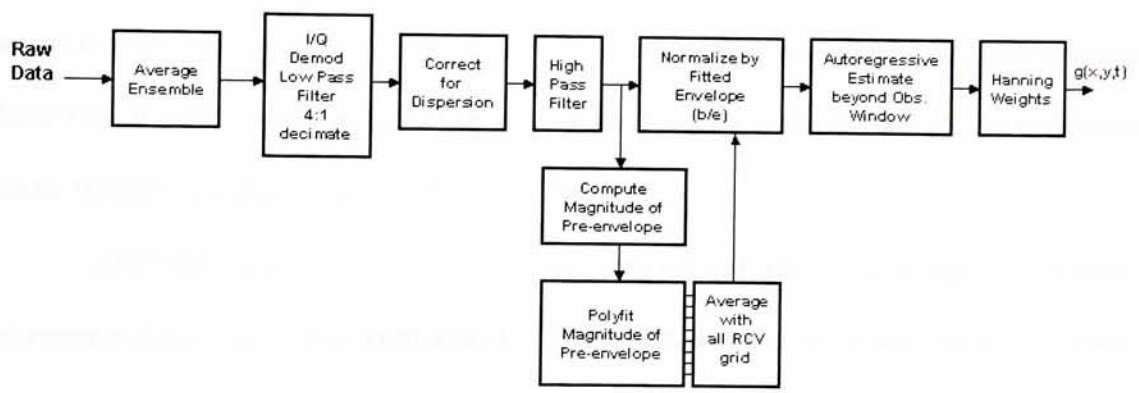

Figure 5.3 Rome Labs Pre-Processing System

The first operation performed in the pre-processor is I and Q channel demodulation. This step enables phase information to be taken from the received signal. Two different I and Q demodulation techniques were used at different development stages of the Rome Labs system. The first approach used separate channels to collect the I and Q signals. The two different channels are sampled at the same frequency, 90 degrees out of phase of each other. The other approach involves using only one channel.

The input data signal is sampled at a rate four times above the 250KHz demodulation frequency. Alternating data points of the sampled signal are then taken. A Hilbert transform is performed on the signal, resulting in two signals, one corresponding to the I channel and one to the Q channel, each containing half the number of samples of the original signal.

The next step in the pre-processing stage is dispersion correction. The transmit signal used in this system is linear frequency modulated from 66 to 6 Mhz. Within this frequency range, the velocity of the transmitted signal through the medium is subject to dispersion. The dispersion correction algorithm adds a phase component to the received signal to compensate for the variation introduced by dispersion. The dispersion phase correction is calculated as a function of chirp frequency and applied to each receiver location. If dispersion is not adequately corrected for, the demodulated signal will retain some frequency variation after it has been dechirped.

After the dispersion correction has been performed, the signal is high pass filtered to remove direct path signal components. The transmit and receive antenna have a multi-directional gain pattern and therefore are not directed solely into the ground. It is possible for the receiver to receive a pulse from the transmitter that has traveled directly through the air from the transmitter, without propagating through the ground. This is known as direct path. Electromagnetic waves travel about four times faster through the air than through the ground. Even if the difference in path distances between the direct path and a valid path through the ground is similar, the direct path return will be received before even the closest return from a valid ground path. After demodulation, the signal is

composed of many frequency components. The frequency of the signal components varies directly with time delay. The time delay associated with a direct path signal is significantly shorter than the time delay associated with a valid path. The frequency components of the direct path signals are therefore much lower than the valid signal returns. The frequency components of the signal caused by direct path can be removed by means of a high pass filter.

After the signal has been filtered to remove the direct path signal component, the magnitude of the signal is normalized to correct for attenuation. Attenuation is frequency dependent, and therefore the higher frequency components of the chirped signal are more affected by attenuation than the lower frequencies. The objective of the attenuation correction is to correct the entire received signal to the same level, so the attenuation correction must be frequency dependant. To calculate the normalization filter, the magnitude of the attenuated signal is fit to a fifth order polynomial envelope function across the entire received signal. The envelope function is calculated at each of the receiver locations and then averaged. If a specific frequency range within the received signal is consistently heavily attenuated, it will be reflected in the averaged envelope. The incoming signal is then multiplied by the inverse of the averaged amplitude function. If the envelope function is heavily attenuated over a certain frequency range, it will have a lower magnitude in that range. By multiplying the input signal by the inverse of the envelope function, heavily attenuated portions of the signal will be boosted more than other portions with less attenuation.

To explain the Autoregressive Estimate and Hanning window blocks of the preprocessing diagram, it is useful to review some signal processing concepts. When a sinusoidal function is multiplied by a rect function in the time domain, it creates a sinc function in the frequency domain. The smaller the rect function is, the higher the sidelobes of the sinc function. A similar effect is occurring with the demodulated signal. The sinusoidal signal of the demodulated signal is observed within a time window, which has the same effect on the frequency components of the signal as a rect function. A Hanning window is a signal processing technique that is frequently used to decrease the sidelobes of the sinc function caused by multiplication of a sinusoidal signal by a rect function. A Hanning window function is demonstrated in Figure 5.4(a-c).

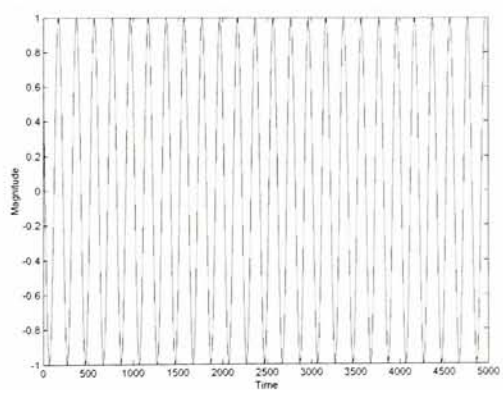

Figure 5.4a A Time Windowed Sinusoid

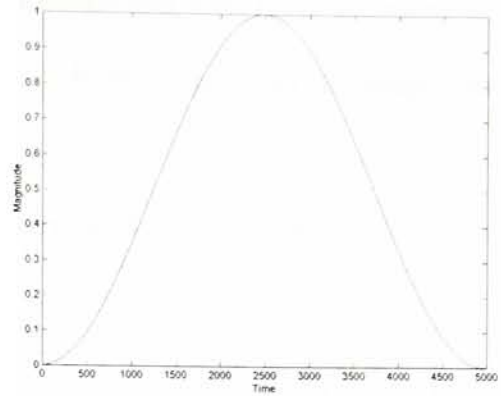

Figure 5.4b Hanning Filter

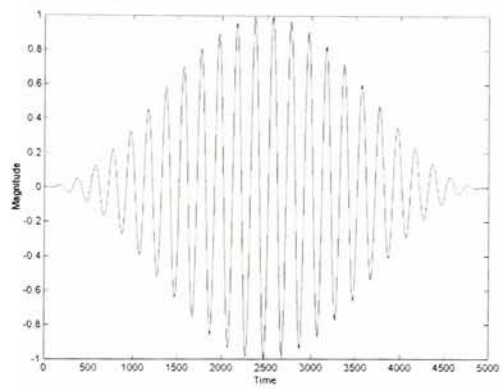

Figure 5.4c Hanning Filter Applied to Windowed Signal

While the Hanning function improves the sidelobes of a function, it also removes some of the information from the beginning and end of the signal, as can be seen in Figure 5.4c. In order to insure that all of the input data is included in the Hanning window, interpolated data is added to the beginning and end of the actual data.

5.3. SAR Processing

After the data has been conditioned and unfavorable effects have been removed, it is sent to the SAR processor. The SAR processor separates the frequency components

received at each receiver location and sorts them according to which region of the scene they were reflected from. It then generates an image based upon the location and magnitude of the return.

The SAR processing procedure is described in Figure 5.5.

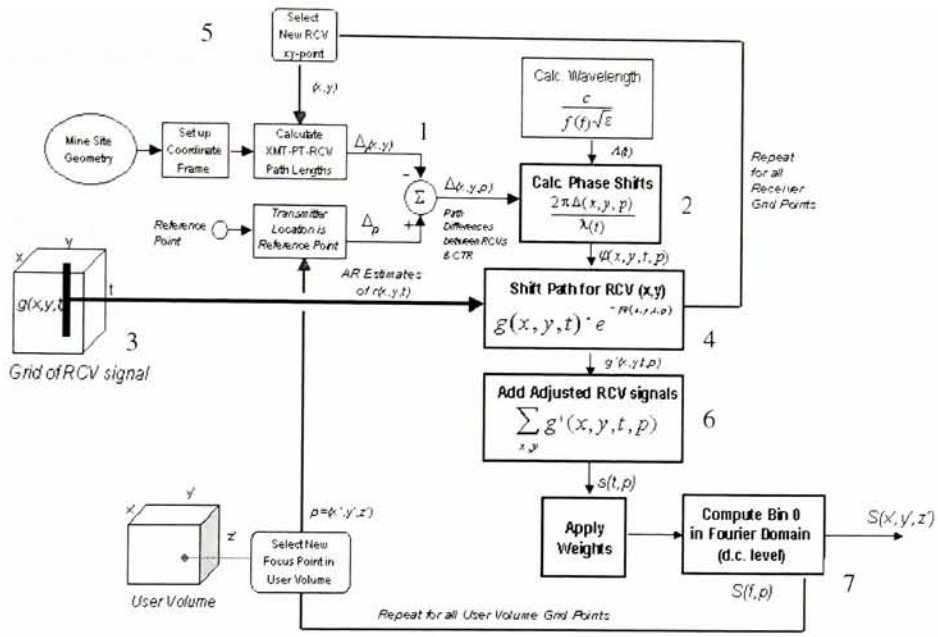

Figure 5.5 Rome Labs SAR Processing System

Before SAR processing takes place, the scene of interest, or user volume must be divided into voxels, or three dimensional volume pixels. The user specifies the size of the voxels used in the GUI. The first step of the SAR processing stage, in the bottom left corner of Figure 5.5, is to select a voxel from the user volume. This voxel is referred to as the voxel under test (VUT). We will call the first VUT selected in the scene VUT 1. An initial receiver location within the receiver array is also selected, as pictured in the upper left portion of Figure 5.5. We will call this receiver location Receiver 1. The Euclidean

distance from the transmitter to VUT1 to Receiver 1 is first calculated. This distance will be referred to as the reference path distance, $\Delta(x,y,p)$. If the scene is to be referenced to a point other than the transmitter, a correction can be added to the reference path distance.

The next step in SAR processing, depicted in the upper right portion of Figure 5.5 is to calculate the reference phase associated with the reference path distance. This is done by first calculating the wavelength of the frequency and then using Equation (5-1).

$$\varphi_r = -2 \cdot \pi \cdot \tau \left(f_c + \gamma t \right) + \pi \cdot \gamma \cdot \tau^2 \tag{5-1}$$

Where φ_r is the reference phase, τ is the time delay associated with the reference path distance, f_c is the frequency offset, and γ is the chirp rate. Equation (5-2) is then used to shift the input data, $g_{m,n}(x,y,t)$ by the reference phase.

$$g'_{m,n}(x, y, t, p) = g_{m,n}(x, y, t) \cdot e^{-j\varphi_{m,n}(x,y,t,p)} \tag{5-2}$$

If the signal at Receiver 1 contains a signal component from VUT 1, the exponential function from Equation (5-2) will cancel with the time-varying portion of $g_{m,n}(x,y,t)$ and there will be a large DC component of $g'_{m,n}(x,y,t,p)$. The samples of the received signal are then summed, returning the DC value of the return.

After Equation (5-2) has been performed for VUT 1 and Receiver 1, the next receiver location is selected, Receiver 2. A new reference path distance is calculated from the transmitter to VUT 1 to Receiver 2. The new reference phase is calculated using Equation (5-1) and $g'_{m,n}(x,y,t,p)$ is calculated using Equation (5-2). The new DC value for $g'_{m,n}(x,y,t,p)$ at Receiver 2 is added to the DC value calculated at Receiver 1. This process is continued for every receiver in the receiver array. After the last receiver

location has been calculated, the next VUT value (VUT 2) is selected and the process is started again.

After a value has been obtained for every voxel in the scene, an image is generated by assigning these values to a three-dimensional image representation of the scene. Each VUT corresponds to a certain voxel in the image representation, and the VUT value is assigned to that voxel.

5.4 GPR Simulation

To test the operation of the GPR software, Rome Labs developed a simulation program that generates an ideal, analytical return from a perfectly diffuse point reflector target. Perfectly diffuse point reflectors are reflectors of infinitesimal size that reflect a transmitted signal equally in every direction. A target is generated by combining a number of perfectly diffuse reflectors in a scene to approximate the target shape. Each of these perfectly diffuse reflectors reflect an equal magnitude signal to each of the receivers in the receiver array.

To create the simulation, the transmitted and received signal must be simulated mathematically. The transmitted signal generated by the Rome labs GPR system is a linear frequency modulated, sinusoidal signal. It can be expressed analytically using Equation (5-3).

$$s(t) = A_0 \cos(2\pi f_c t + \pi \gamma \ t^2) \tag{5-3}$$

In this equation, s(t) represents the transmitted signal, A_0 represents the maximum amplitude of the signal, f_c is the starting frequency, t is time in seconds, and γ is the chirp

rate. Equation (5-3) is similar to a sinusoidally varying signal, except that the second term in the cosine function increases the frequency as a function of time squared.

Assuming a loss-less environment, when the transmitted signal described by Equation (5-3) is applied to a scene, the signal measured at the receiver will be equal to the transmitted signal delayed in time. The length of the delay is determined by the propagation time from the transmitter to the reflector, and then to the receive antenna. This delay time is a factor of the distance traveled by the signal and the dielectric properties of the material. If the signal takes τ seconds to travel from transmitter to receiver, the received signal for a given scatterer can be expressed by Equation (5-2).

$$R(t) = a(t)\cos(2\pi f_c(t-\tau)+\pi\gamma(t-\tau)^2 \tag{5-4}$$

Where R(t) is the received signal as a function of time. The amplitude a(t) is expressed as a function of time because the signal will experience greater attenuation as it travels through a lossy medium. Because this attenuation is a function of distance or range, it is also a function of time.

After the signal is received, it is demodulated. Demodulation involves removing the original transmitted signal from the received signal. This is done by downconverting the received signal. Downconversion is done by first multiplying the received signal, which has been delayed in time, by the transmitted signal and then performing lowpass filtering. The signal used to downconvert the received waveform is scaled in frequency by an intermediate frequency, f_{if}. Equations (5-5) through (5-9) show the downconversion of the received signal. For convenience, the following substitutions can be made for the transmit and received signals:

$$\alpha = (2\pi f_c t - \pi \gamma t^2)$$
$$\beta = 2\pi f_c (t-\tau) + \pi \gamma (t-\tau)^2 \tag{5-5}$$

$$s(t) \cdot R(t) = \cos(\alpha)\cos(\beta) \tag{5-6}$$
$$= \frac{1}{2}[\cos(\alpha-\beta) + \cos(\alpha+\beta)]$$

The higher frequency component of this function is removed in the low pass filtering leaving

$$r(t) = \frac{1}{2}\cos(\alpha-\beta) \tag{5-7}$$

Equation (5-7) can be simplified by substituting θ for (α-β), leaving

$$r(t) = \frac{1}{2}\cos(\theta) = \frac{1}{2}\mathrm{Re}(e^{j\theta}) \tag{5-8}$$

where

$$\theta = (\alpha - \beta) = -2\pi\tau\,(f_c + \gamma t) + \pi\gamma\tau^2 + 2\pi f_{if} t \tag{5-9}$$

Equation (5-7) can be broken down into three different terms:

$-2\pi \cdot \tau(f_c + \gamma \cdot t)$	Doppler and Range Frequency Terms
$\pi \cdot \gamma \cdot \tau^2$	Residual Video Phase Term
$2\pi \cdot f_{if} t$	IF Frequency Term

The intermediate frequency term can be removed by downconverting the signal by the intermediate frequency term and then low pass filtering. Removal of the IF term yields:

$$\theta = -2\pi\tau\,(f_c + \gamma t) + \pi\gamma\tau^2 \tag{5-10}$$

Up to this point, it has been assumed that the signal measured at the receiver is the result of a signal that was only reflected by a single scatterer. The actual system will receive a signal at each receiver location that contains returns from many different scatterers. The uniform point source simulated returns at a single receiver location contain a return from each of the perfectly diffuse scatterers that make up the simulated target. For each scatterer, there will be a different delay, τ. The effect of the individual delays from each scatterer can be calculated using Equation (5-10). The received signal for a given receiver location can be calculated by summing the returns from each of the individual scatterers. For a given receiver, m and N scatterers, the received signal can be expressed as:

$$\sum_{n=1}^{N} a(t) \cdot \mathrm{Re}[e^{j\theta_{m,n}}] \qquad (5\text{-}11)$$

Where n = {1...N} references each individual scatterer.

Equation (5-11) is a mathematical representation of a return signal received at one of the receiver locations. The simulated signal contains all of the individual returns from each of the scatterers in the scene. It can be subjected to the same SAR processing as an actual received signal to extract the contribution of each scatterer in the scene.

This section described the processing involved in generating a scene using the Rome Labs System. The simulated returns generated using the ray-tracing simulation can be input into the GPR processing system to generate a simulated scene image. In the following section, several images are generated using ray-tracing simulated returns and the Rome Labs GPR system.

6. Results

To assess the performance of the ray-tracing simulator, several scene configurations were created and run through the Rome Labs GPR processing software. The scenes were selected to reflect different target, transmitter, and receiver array locations and orientations. The size of the target, the size of the receiver array, and the number of receivers in the receiver array were also varied. The transmitted ray direction were either selected manually or using the automatic ray generator.

This section contains images showing the results of the data set runs. Two images were generated for each data set: the scene configuration image and the GPR processed image. The scene configuration images depict the transmitter, the faceted target, and the receiver array. The transmitter is represented by a bow-tie shaped frame. The faceted target appears as a three-dimensional box with the facets visible on the outside. The receiver array is represented by a two-dimensional light blue rectangle. The rays are represented by dark blue lines extending from the transmitter. For clarity, only rays that propagate to a valid target are pictured, although additional rays may have been generated in the simulation. The GPR processed image shows the image generated by the Rome Labs GPR processing software. A reference target image has been superimposed upon the GPR processed image to show the location and proportions of the actual target.

Throughout this section, the dimensions and positions of the transmitter, target, and receiver arrays are specified in feet. They are expressed in Cartesian coordinates, as (X dimensions, Y dimensions, Z dimensions) or (X location, Y location, Z location). The

relative dielectric permittivity of the target was set to 2 and the relative dielectric permittivity of the surrounding scene was set to 15.

The Rome Labs system assigns a threshold to the voxels magnitude values in the scene. The generated image is composed of each voxel in the scene that exceeds this magnitude threshold. For the images in this section, the threshold was set to the top third of the magnitude values of the voxels in the scene.

6.1 Automatic Ray Generation

The automatic ray generator was used to generate the rays used in data sets 1-7. The automatic ray generator creates the ray equations such that a ray is received at every receiver location, after being specularly reflected from the target. The target's size and location in the X and Y dimensions are also adjusted to ensure that each receiver in the array receives a ray. The size and location of the target in the Z dimension are as specified by the user. Automatic ray generation is a useful tool to observe certain characteristics of scene configurations, ensuring that a sufficient number of rays are received by the receiver array.

Data set 1:

Transmitter Origin:	(0,50,0)	**Ray Generation:**	Automatic
Receiver Array Location:	(100,50,0)	**Receiver Array Dimensions:**	(100,100,0)
Receiver Spacing X:	10	**Receiver Spacing Y:**	10
Target Location:	(52.5, 52.5, -40)	**Target Size:**	(52, 52, 20)

Table 6.1: Data Set 1 Scene Configuration Information

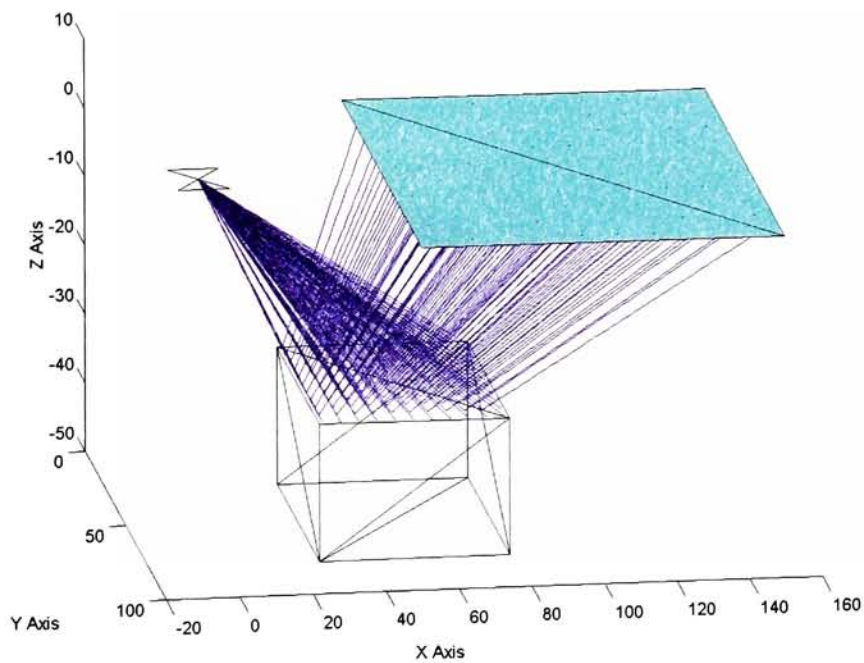

Figure 6.1a. Data Set 1 Scene Configuration Image

The images generated with the scene orientation used in data set 1 are intended to be a means of comparison of effects observable using the automatic ray generator. The orientation of the projected rays can be observed in Figure 6.1a. Due to the use of the

automatic ray generator, the top of the target has a large number of reflections directly to the receiver array. There are not any rays that transmit through the target.

The image generated by the Rome Labs GPR processing software for data set 1 is depicted in Figure 6.2b. The processed image is fairly consistent with the superimposed original target for about one half of the length of the target. Behind the target, there is a tail that extends from the top of the target towards the transmitter.

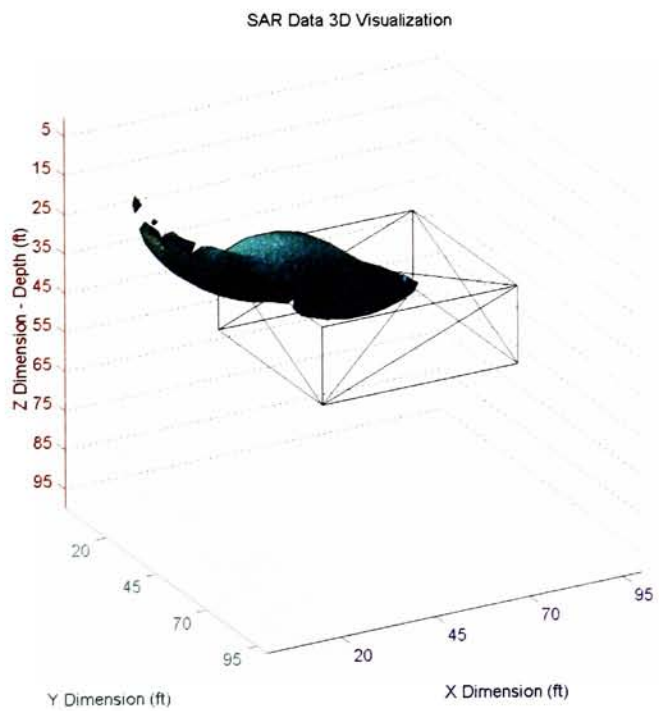

Figure 6.1b. Data Set 1 GPR Processed Image

6.1.1 Transmitter Orientation

Data sets 2 and 3 were set up similarly to data set 1, except the position of the transmitter was varied in the Y dimension. These data sets were performed to observe

the effects of varying the position of the transmitter laterally compared to the receiver array.

Data set 2:

Transmitter Origin:	(0,0,0)	**Ray Generation:**	Automatic
Receiver Array Location:	(100,50,0)	**Receiver Array Dimensions:**	(100,100,0)
Receiver Spacing X:	10	**Receiver Spacing Y:**	10
Target Location:	(52.5,27.5,-40)	**Target Size:**	(52, 52, 20)

Table 6.2: Data Set 2 Scene Configuration Information

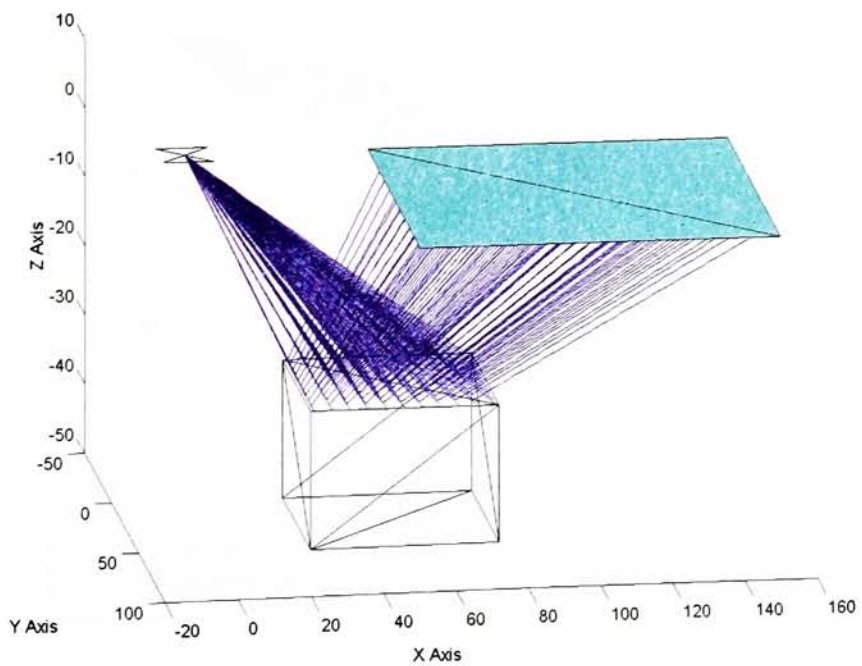

Figure 6.2a. Data Set 2 Scene Configuration Image

The scene configuration and GPR processed images for data set 2 are depicted in Figure 6.2(a-b). The configuration for this scene is the same as that for data set 1, except that the transmitter has been shifted to the X, Y, and Z coordinates (0,0,0). The target dimensions are (52, 52, 20) and the target is centered at (52.5, 27.5, -40). There are no rays that are transmitted into the target.

The processed image is similar to the image in data set 1. There is a tail present in the image that extends towards the transmitter, but the transmitter is located at the origin, so the tail extends at an angle.

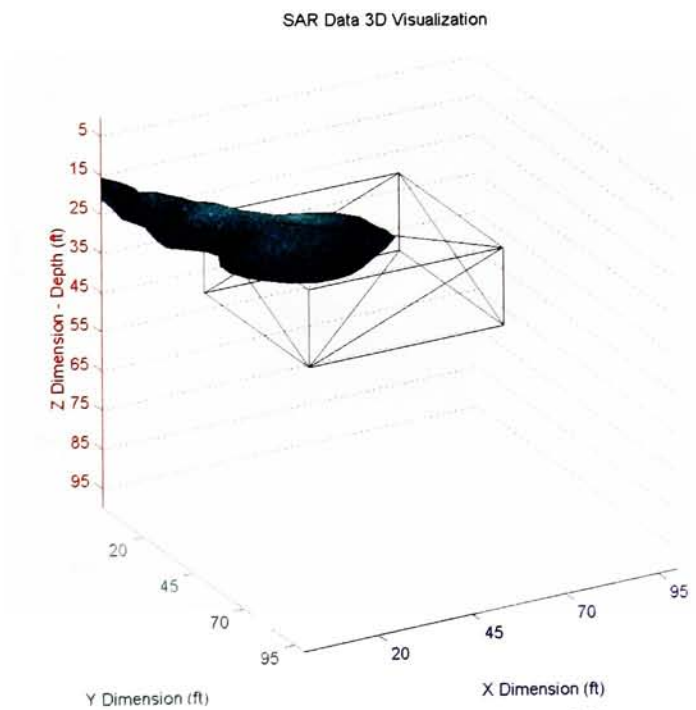

Figure 6.2b. Data Set 2 GPR Processed Image

Data set 3:

Transmitter Origin:	(0,100,0)	**Ray Generation:**	Automatic
Receiver Array Location:	(100,50,0)	**Receiver Array Dimensions:**	(100,100,0)
Receiver Spacing X:	10	**Receiver Spacing Y:**	10
Target Location:	(52.5, 77.5, -40)	**Target Size:**	(52, 52, 20)

Table 6.3: Data Set 3 Scene Configuration Information

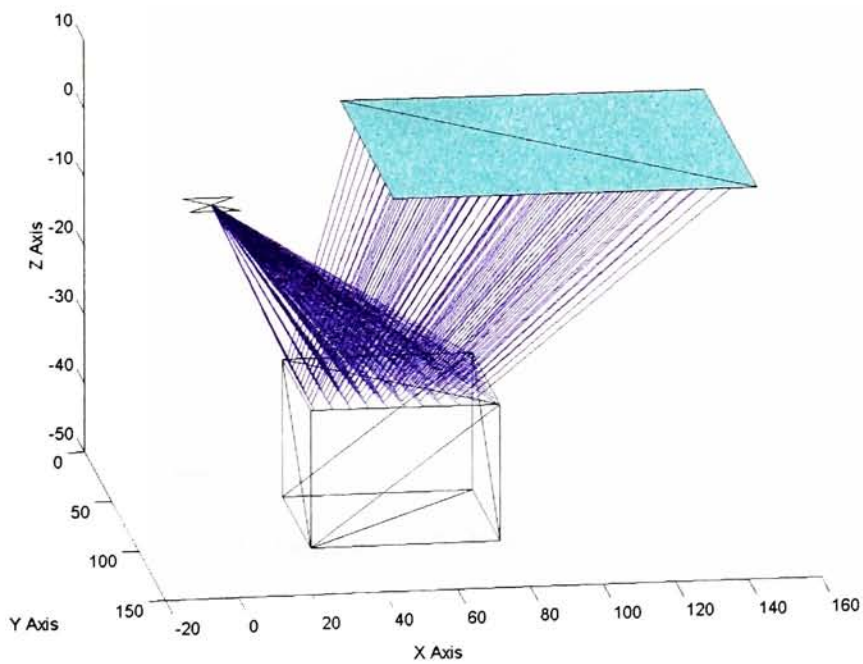

Figure 6.3a. Data Set 3 Scene Configuration Image

In data set 3, depicted in Figure 6.3(a-b), the transmitter is moved along the Y axis to the edge of the receiver array at (0, 100, 0). The resulting target is positioned at

(52.5, 77.5, –40) and has dimensions of (52, 52, 20). Like sets 1 and 2, there are no rays that transmit into the target.

Similar results were obtained in the GPR processed image as in data set 2. There is a tail that extends from the top of the superimposed target towards the transmitter, which is closer to the viewer as the image appears in Figure 6.3b.

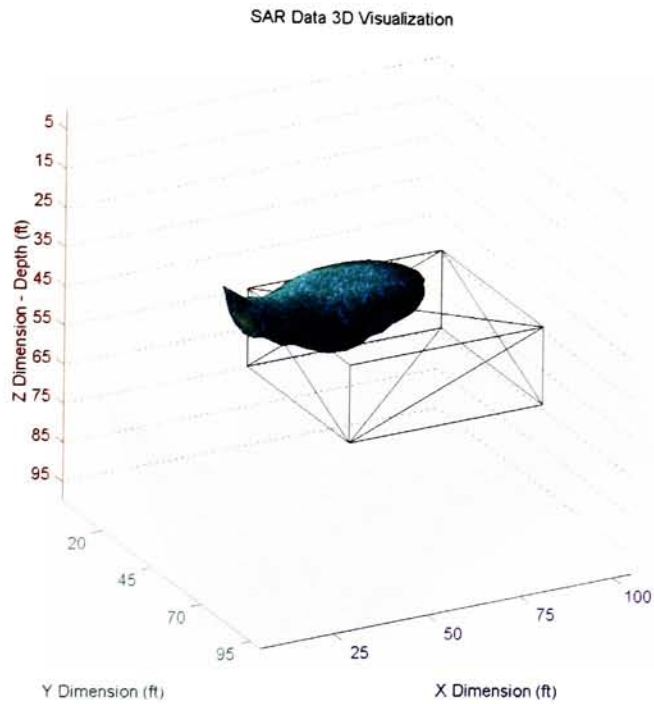

Figure 6.3b. Data Set 3 GPR Processed Image

6.1.2 Receiver Orientation

In data sets 4-7, the size of the receiver array and the spacing between the receivers was varied. The number of receivers in the array was calculated based upon the size of the receiver array. Therefore, larger receiver arrays had a greater number of receivers within them. The spacing between the receivers was also varied, making the array either more or less densely populated with receivers.

Data set 4:

Transmitter Origin:	(0,50,0)	**Ray Generation:**	Automatic
Receiver Array Location:	(100,50,0)	**Receiver Array Dimensions:**	(100,100,0)
Receiver Spacing X:	5	**Receiver Spacing Y:**	5
Target Location:	(51.25,51.25,-40)	**Target Size:**	(52, 52, 20)

Table 6.4: Data Set 4 Scene Configuration Information

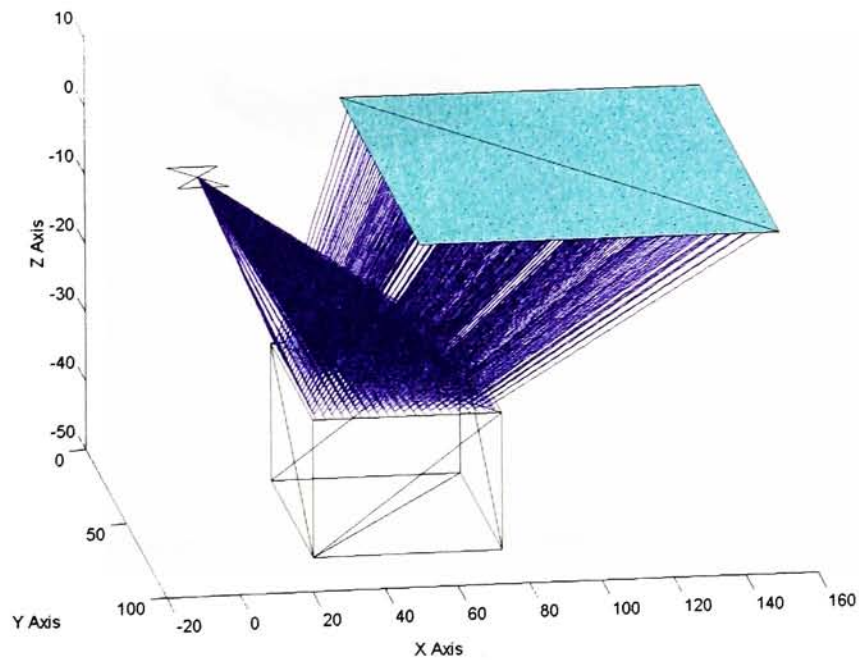

Figure 6.4a. Data Set 4 Scene Configuration Image

The fourth data set was generated using a receiver array with a denser concentration of receivers. The receivers in the array were spaced at 5 ft intervals in both the X and Y dimensions. The target's X and Y dimensions, generated by the automatic

ray generator, were found to be (52, 52, 20) and were centered at (51.25, 51.25, -40). There are considerably more rays reflected from the top of the target, but there are no rays that are transmitted into the target.

Figure 6.4b shows the GPR processed image generated using data set 4. There is a very strong return reflected from the top of the target. As in previous data sets, there is a tail extending from the target top towards the transmitter.

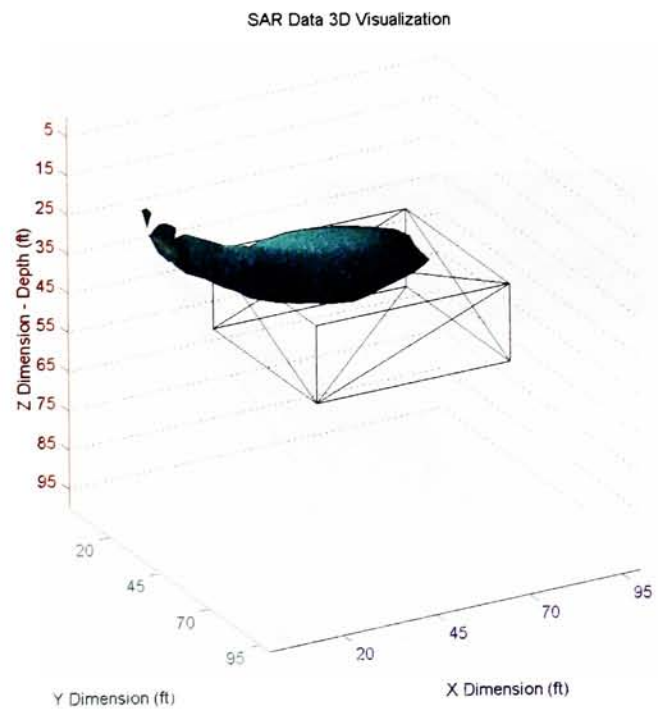

Figure 6.4b. Data Set 4 GPR Processed Image

Data Set 5:

Transmitter Origin:	(0,50,0)	**Ray Generation:**	Automatic
Receiver Array Location:	(100,50,0)	**Receiver Array Dimensions:**	(100,100,0)
Receiver Spacing X:	20	**Receiver Spacing Y:**	20
Target Location:	(51.25,51.25,-40)	**Target Size:**	(52, 52, 20)

Table 6.5: Data Set 5 Scene Configuration Information

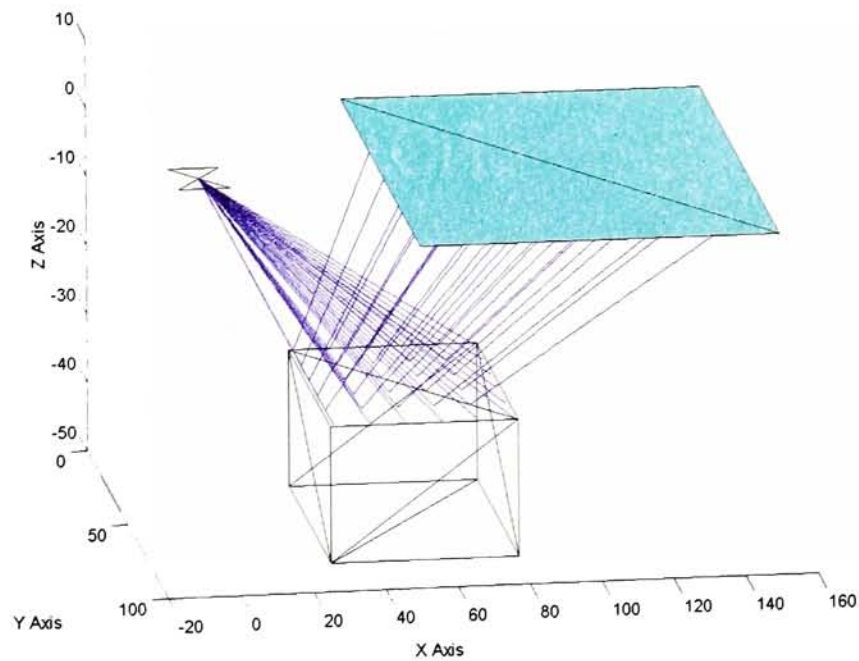

Figure 6.5a. Data Set 5 Scene Configuration Image

In data set 5, the simulation was run with a less densely populated receiver array, with the receivers spaced at 20 ft intervals in the X and Y dimensions. The GPR processed image for data set 5 is shown as Figure 6.5b. The image is clustered towards the front of the superimposed target. Only a small percent of the generated image is

actually in the immediate area of the target. There is a pronounced tail extending towards the transmitter.

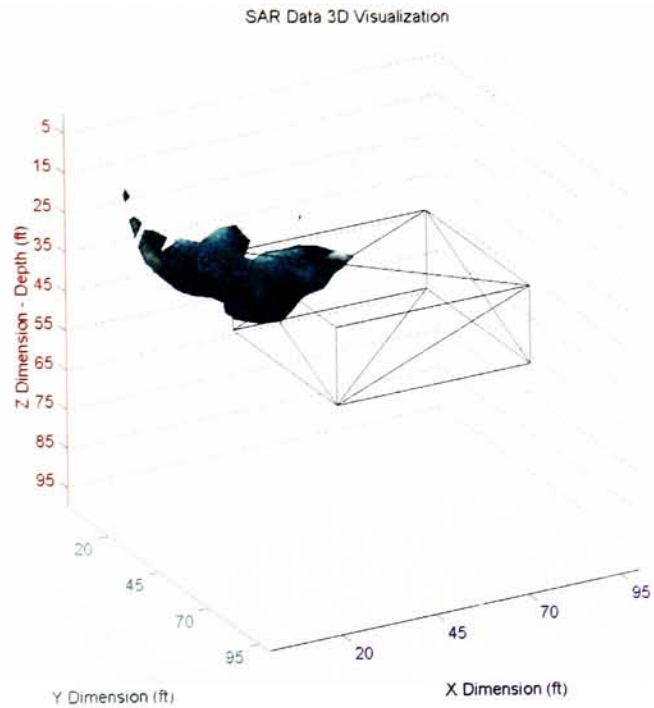

Figure 6.5b. Data Set 5 GPR Processed Image

Data Set 6:

Transmitter Origin:	(0,75,0)	**Ray Generation:**	Automatic
Receiver Array Location:	(100,75,0)	**Receiver Array Dimensions:**	(100,150,0)
Receiver Spacing X:	10	**Receiver Spacing Y:**	10
Target Location:	(52.5,77.5,-40)	**Target Size:**	(52,77,20)

Table 6.6: Data Set 6 Scene Configuration Information

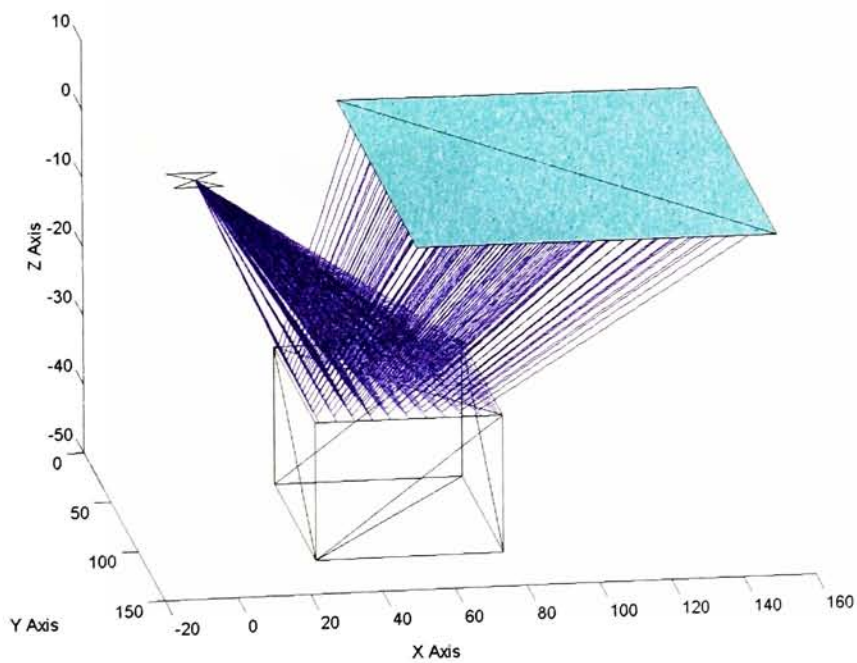

Figure 6.6a. Data Set 6 Scene Configuration Image

In data set 6, the receiver array was expanded to 100 ft in the X direction and 150 ft in the Y direction. The receiver array is centered at (100, 75, 0). Because the receiver array size was expanded and the spacing of the receivers was held constant, the number

of receivers increased from 121 to 176. The transmitter was moved to (0, 75, 0) so that it would remain centered between the sides of the receiver array in the Y dimension.

Figures 6.6(a-b) shows the scene configuration of data set 6. The GPR processed image for data set 6 is shown as Figure 6.6b. The image generated covers almost the entire target in the Y direction, but less than half of the target in the X direction. A tail extends from the top of the target towards the transmitter in the X direction.

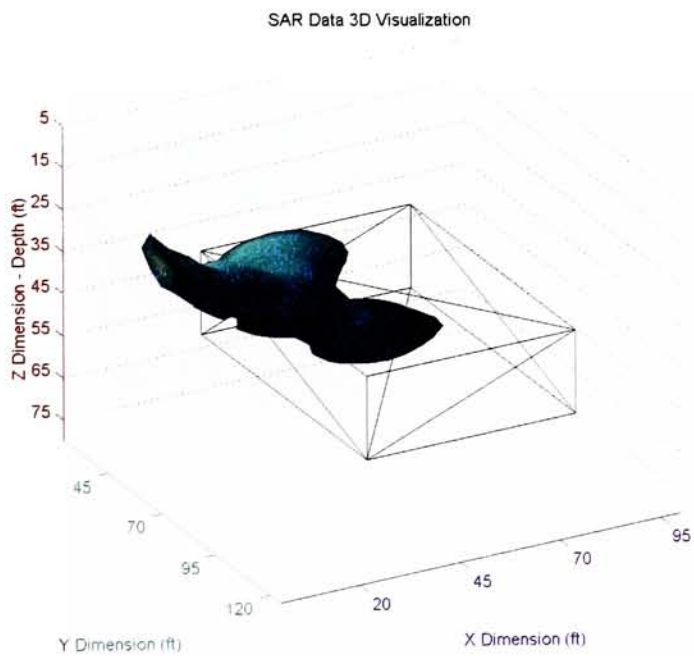

Figure 6.6b. Data Set 6 GPR Processed Image

Data Set 7:

Transmitter Origin:	(0,50,0)	**Ray Generation:**	Automatic
Receiver Array Location:	(100,50,0)	**Receiver Array Dimensions:**	(150,100,0)
Receiver Spacing X:	10	**Receiver Spacing Y:**	10
Target Location:	(52.5,52.5,-40)	**Target Size:**	(77,52,20)

Table 6.7: Data Set 7 Scene Configuration Information

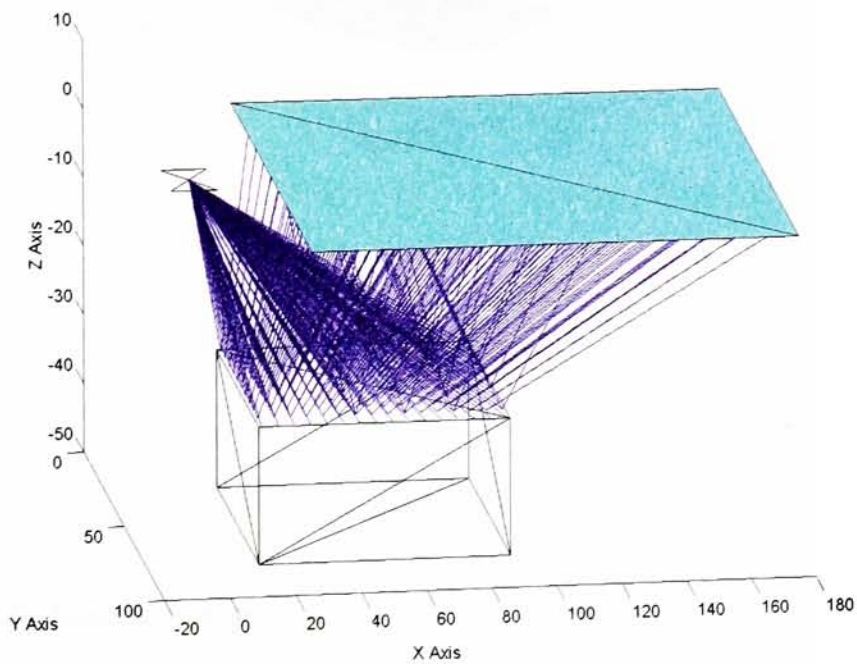

Figure 6.7a. Data Set 7 Scene Configuration Image

In data set 7, the size of the receiver array was increased in the X direction. The receiver array was of size (150, 100, 0) with receivers spaced every 10 ft in the Y direction and every 10ft in the X direction. As can be seen in Figure 6.7a, several rays reflected repeatedly from the top of the target and off of the bottom of the ground; however, no rays were transmitted into the target.

The GPR processed image for data set 7 is shown as Figure 6.7b. The image extends approximately halfway across the target. There is a tail that extends from the top of the target towards the transmitter.

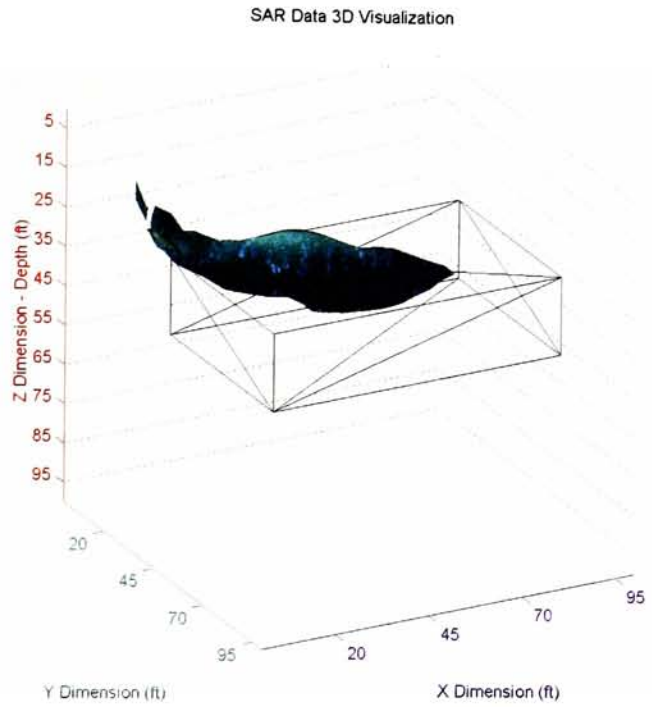

Figure 6.7b. Data Set 7 GPR Processed Image

6.2 Manually Generated Rays

In data sets 8-13, the size and position of the target was varied. In all of the data sets in this section, the transmitter and receiver array orientation was the same. The receiver array was a (100, 100, 0) ft square with receivers spaced at 10ft intervals in the X and Y directions. The receiver array was centered at (100, 50, 0). In this data set, the transmitted rays were sent from a transmitter located at (0, 50, 0) and generated manually without the aid of automatic ray generator. It is recommended in the Xpatch manual that

10 rays are projected at a target per each unit of wavelength. It also states that for an uncomplicated target, 3 rays per unit of wavelength are sufficient [8]. Because our target is not complicated, 3 rays per unit of wavelength were used.

To determine the number of rays to use, it was first necessary to calculate the wavelength of the transmitted signal. The wavelength can be calculated from:

$$\lambda = \frac{c}{f\sqrt{\varepsilon\mu}} \tag{6-1}$$

Where f is the frequency of the transmitted signal, ε is the relative dielectric permittivity and μ is the relative magnetic permeability. The relative dielectric permittivity assumed in the simulation was 15. This is a typical dielectric constant for granite or soil [23]. The magnetic permeability is frequently assumed to be 1 in GPR simulations [7]. The transmitted frequency was 66-6 MHz. We will use the higher frequency, which requires a greater number of rays, as a worst-case scenario. The wavelength is calculated to be 1.17 m, or 3.84 ft.

The following example will demonstrate how the number of rays is chosen. Take, for example a target of dimensions (20, 40, 20) ft. The dimensions in units of wavelength are (5.20, 10.41, 5.20)λ. The maximum area of this object seen by the transmitter in the scene configuration defined above is seen when the target is tilted at a 45-degree angle. The maximum area is:

$$\sqrt{5.20^2 + 5.20^2} \times 10.41 = 76.55\lambda^2 \tag{6-2}$$

It is recommended that 3 rays per linear unit of wavelength are sent. In a two dimensional area, 9 rays must be transmitted per unit of λ^2. This equates to 689 rays.

The wavelength and antenna dimensions can be used to calculate if the system is operating in the Fresnel or far field. The extent of the Fresnel field is from $D^2/4\lambda$ to D^2/λ. The far field extends past D^2/λ. Using the wavelength value calculated above and an antenna diameter of 22 ft, we find that the Fresnel field extends from 38.5 ft to 126.2 ft away from the transmitter. The far field extends past 126.2 ft from the transmitter. The target positions used in this section are within the Fresnel field. As discussed in Section 4, transmitters operating in the near field can be modeled using rays that originate at the transmitter location and extend radially away from it. This technique will be used to model the transmitted signal in this section.

Data Set 8:

Transmitter Origin:	(0,50,0)	**Ray Generation:**	Manual
Receiver Array Location:	(100,50,0)	**Receiver Array Dimensions:**	(100,100,0)
Receiver Spacing X:	10	**Receiver Spacing Y:**	10
Target Location:	(50,50,-40)	**Target Size:**	(20,40,20)
Ray Array Size: X	26	**Ray Array Size: Y**	26

Table 6.8: Data Set 8 Scene Configuration Information

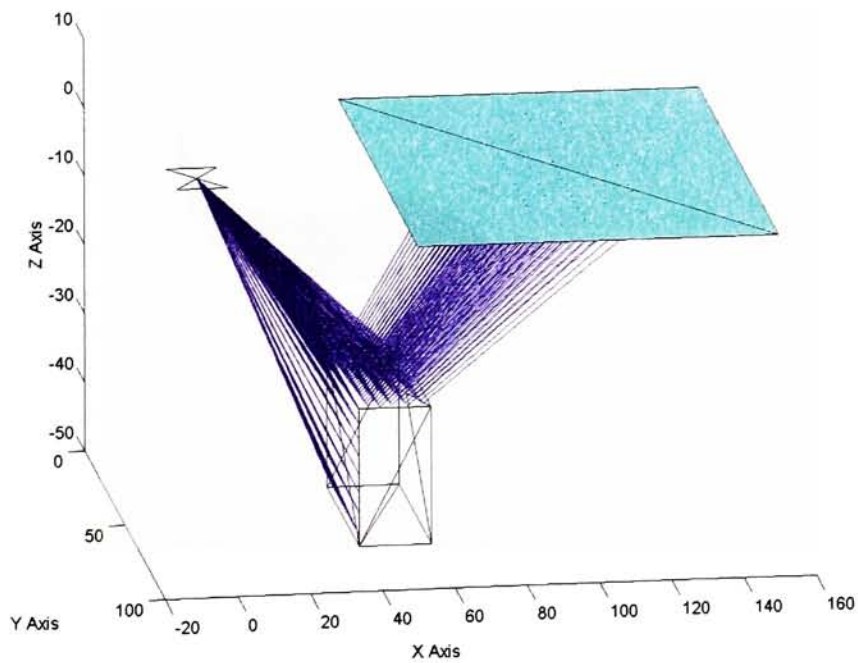

Figure 6.8a Data Set 8 Scene Configuration Image

Data set 8, and the images associated with it were intended to be useful in comparison of different scene orientations used with manually generated rays. In data set 8, the target is of dimensions (20, 40, 20) and is centered at (50, 50, -40). The transmitter

projects a 26 by 26 array of rays towards the target. As can be seen in Figure 6.8a, many rays contact the side of the target and are not transmitted into the target. This is because the rays are incident at a glancing angle. Snell's law states that rays are more likely to penetrate a target at a more direct angle. The rays that extend to the receiver array are specularly reflected from the top of the target.

The GPR processed image for data set 8 shows a thick image, which covers the majority of the top of the target. There is also a dense tail that extends from the top of the target in the X dimension towards the transmitter.

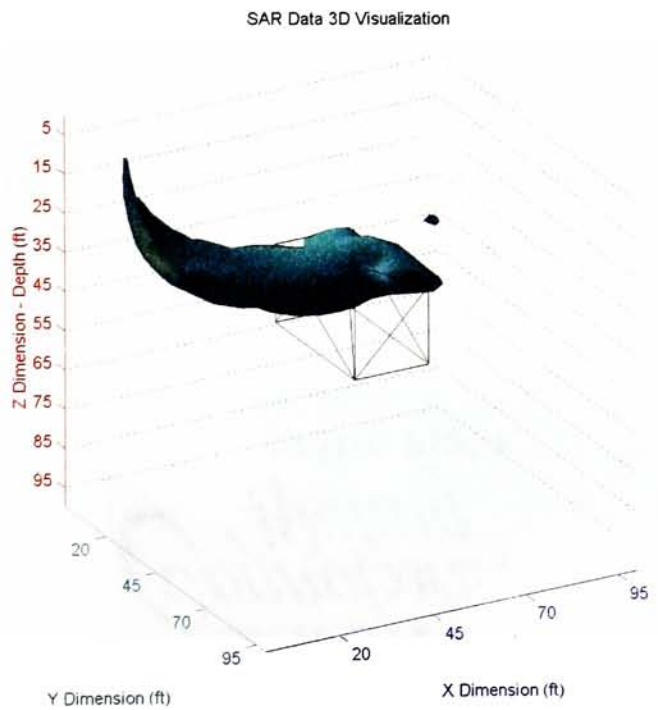

Figure 6.8b Data Set 8 GPR Processed Image

6.2.1 Target Position

In this section, the position, orientation, and depth of the target are varied. The results are observable in data sets 9-13. All data sets use the same receiver array location, dimensions, and spacing.

Data Set 9:

Transmitter Origin:	(0,50,0)	**Ray Generation:**	Manual
Receiver Array Location:	(100,50,0)	**Receiver Array Dimensions:**	(100,100,0)
Receiver Spacing X:	10	**Receiver Spacing Y:**	10
Target Location:	(50,50,-40)	**Target Size:**	(100,20,20)
Ray Array Size: X	82	**Ray Array Size: Y**	21

Table 6.9: Data Set 9 Scene Configuration Information

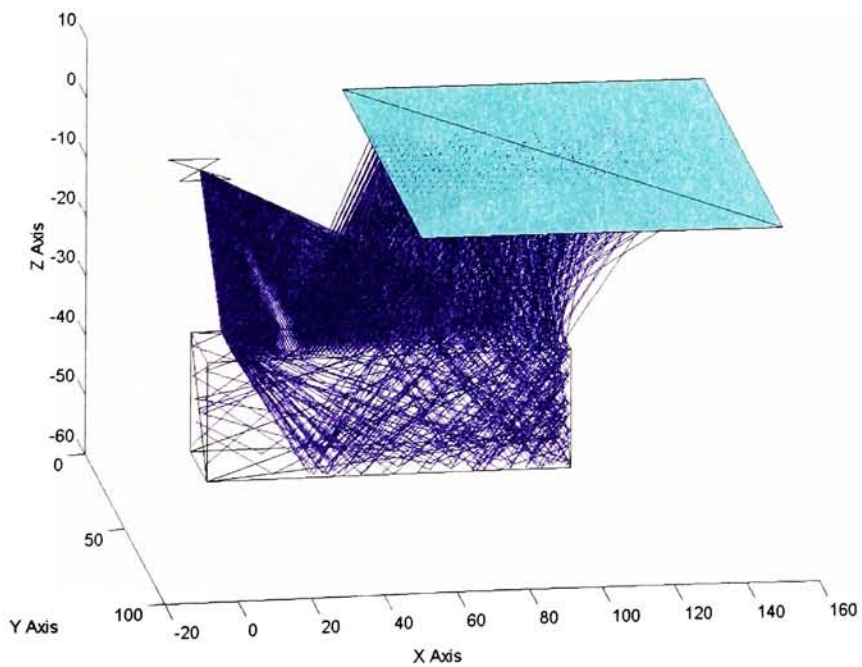

Figure 6.9a. Data Set 9 Scene Configuration Image

In data set 9, the target is rectangular in shape with its longer dimension in the X dimension. The target size is (100, 20, 20) and it is centered at (50, 50 ,-40). An 82 by 21 array of rays is transmitted at the target. A large number of rays are reflected from the top of the target. There are also a large number that penetrate into the target. The penetrating rays make several reflections within the target and many intersect the receiver array. Some of the rays that are reflected from the top of the target are reflected towards the receiver array, reflect from the bottom of the receiver array, and are reflected from the target again towards the receiver array.

The GPR processed image of data set 9 shows a dense image located closest to the transmitter in the X direction. There is a broken tail that extends from the top of the target towards the transmitter in the X direction.

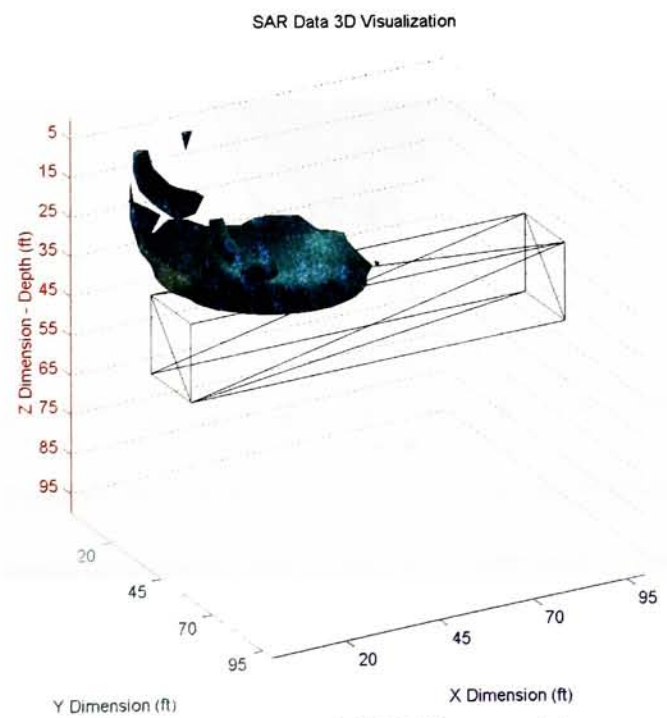

Figure 6.9b. Data Set 9 GPR Processed Image

Data Set 10:

Transmitter Origin:	(0,50,0)	**Ray Generation:**	Manual
Receiver Array Location:	(100,50,0)	**Receiver Array Dimensions:**	(100,100,0)
Receiver Spacing X:	10	**Receiver Spacing Y:**	10
Target Location:	(50,50,-40)	**Target Size:**	(20,100,20)
Ray Array Size: X	21	**Ray Array Size: Y**	82

Table 6.10: Data Set 10 Scene Configuration Information

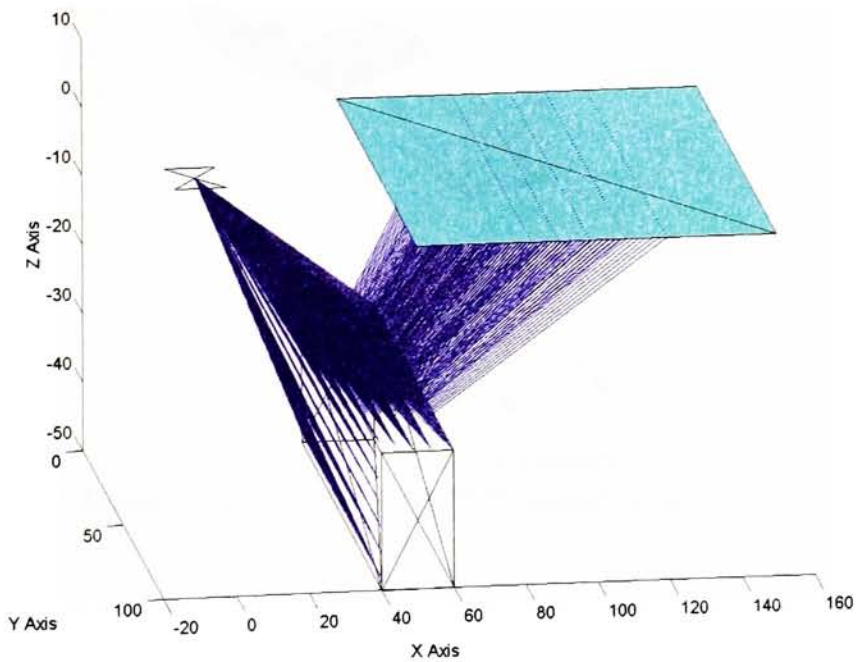

Figure 6.10a. Data Set 10 Scene Configuration Image

The same target dimensions used in data set 9 were used in data set 10, except the orientation of the target is rotated so the longer dimension of the target is oriented in the Y dimension. An array of 21 by 82 rays was transmitted at the target from the transmitter. As in data set 8, many rays impact the side of the target and are not

transmitted into the target, making the only rays that extend to the receiver array those that are reflected from the top of the target.

Figure 6.10b shows the GPR processed image of data set 10. The image generated does not extend to the sides of the target, but is centered in the Y dimension. There is a tail that extends from the top of the target towards the transmitter.

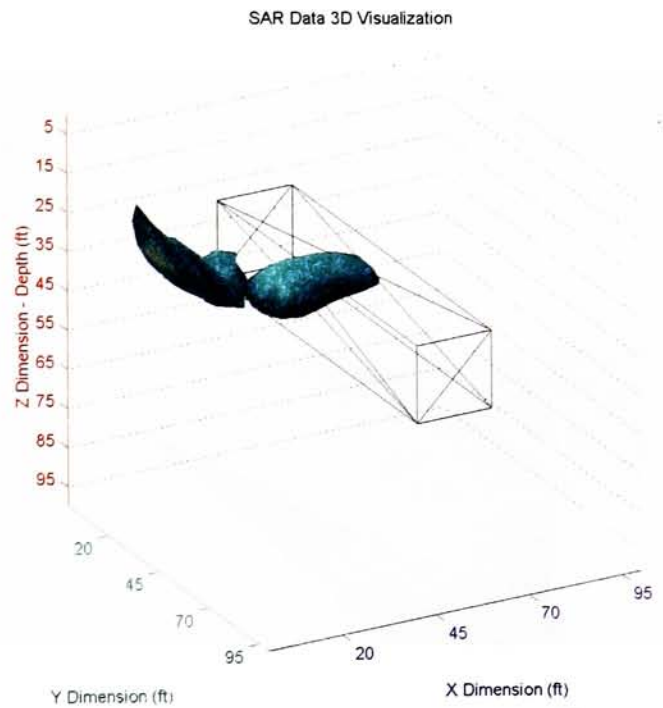

Figure 6.10b. Data Set 10 GPR Processed Image

Data Set 11:

Transmitter Origin:	(0,50,0)	**Ray Generation:**	Manual
Receiver Array Location:	(100,50,0)	**Receiver Array Dimensions:**	(100,100,0)
Receiver Spacing X:	10	**Receiver Spacing Y:**	10
Target Location:	(100,50,-40)	**Target Size:**	(20,40,20)
Ray Array Size: X	26	**Ray Array Size: Y**	26

Table 6.11: Data Set 11 Scene Configuration Information

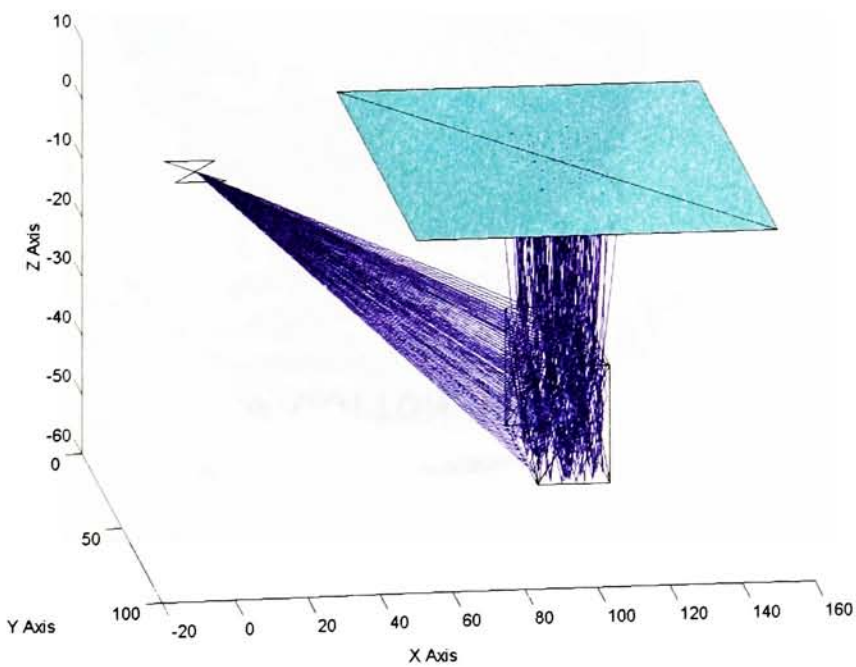

Figure 6.11a. Data Set 11 Scene Configuration Image

In data set 11, the target was moved to the location (100, 50, -40). Because the target is positioned directly underneath the receiver, there are no rays reflected from the top of the target. The distance separating the transmitter and receiver caused the rays that

are incident on the side of the target to be at a more direct angle, allowing them to transmit into the target. These rays are subject to several reflections within the target, and many are reflected towards the receiver array.

The GPR processed image for data set 11 shows a significant amount of clutter, making it difficult to determine the exact location of the target. There is a hemispherical shaped clutter pattern with its bottom at approximately the position of the target. There are two distinct erroneous images immediately below the bottom of the hemisphere.

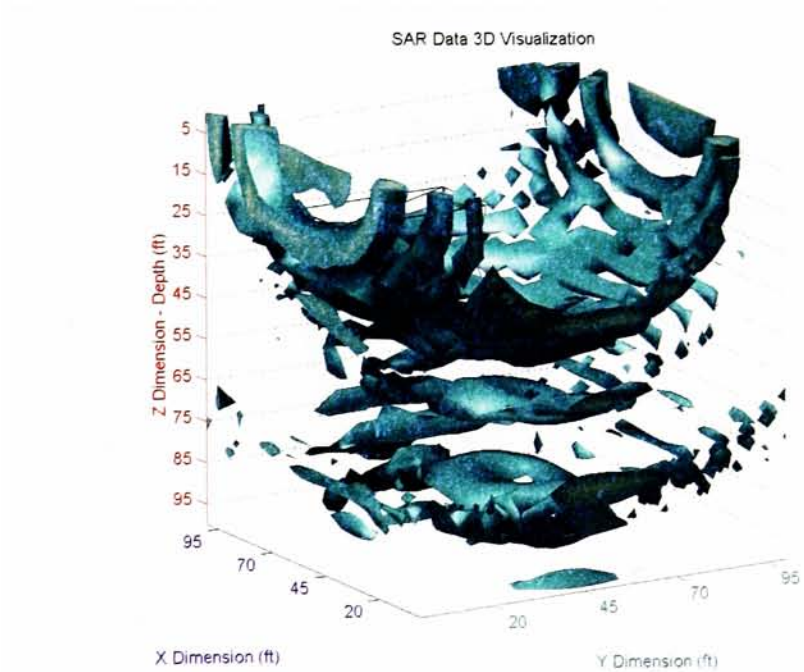

Figure 6.11b. Data Set 11 GPR Processed Image

Data Set 12:

Transmitter Origin:	(0,50,0)	**Ray Generation:**	Manual
Receiver Array Location:	(100,50,0)	**Receiver Array Dimensions:**	(100,100,0)
Receiver Spacing X:	10	**Receiver Spacing Y:**	10
Target Location:	(50,50,-100)	**Target Size:**	(20,40,20)
Ray Array Size: X	26	**Ray Array Size: Y**	26

Table 6.12: Data Set 12 Scene Configuration Information

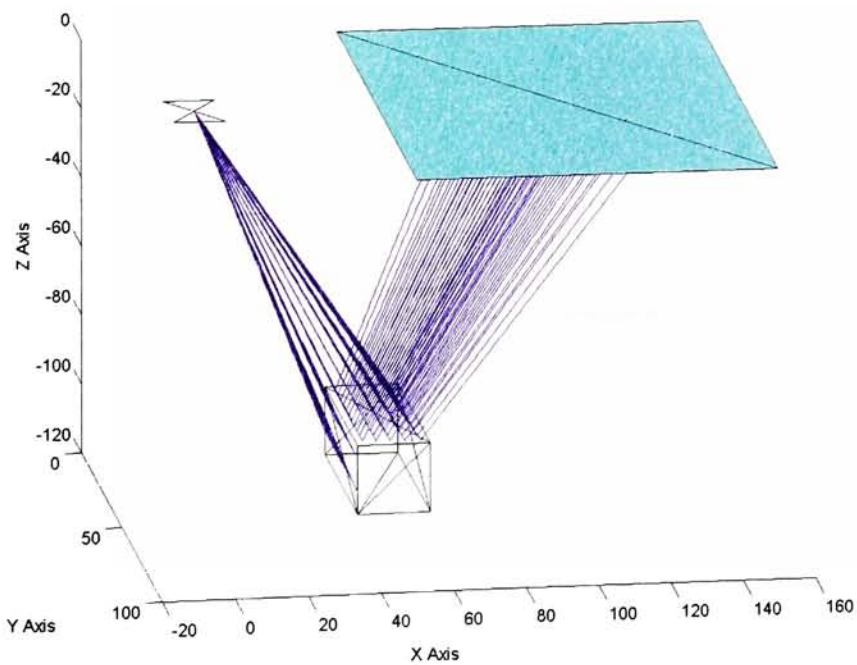

Figure 6.12a. Data Set 12 Scene Configuration Image

In data set 12, a (20, 40, 20) target was lowered in the Z direction to a location of (50, 50, -100). Similar to data set 8, few of the rays were transmitted into the target. The only rays that intersect with the receiver array are those reflected from the top of the target.

The resulting GPR processed image is approximately the same dimensions as the target. The image has a less pronounced tail extending towards the transmitter and a slight overhang extending in the positive X direction.

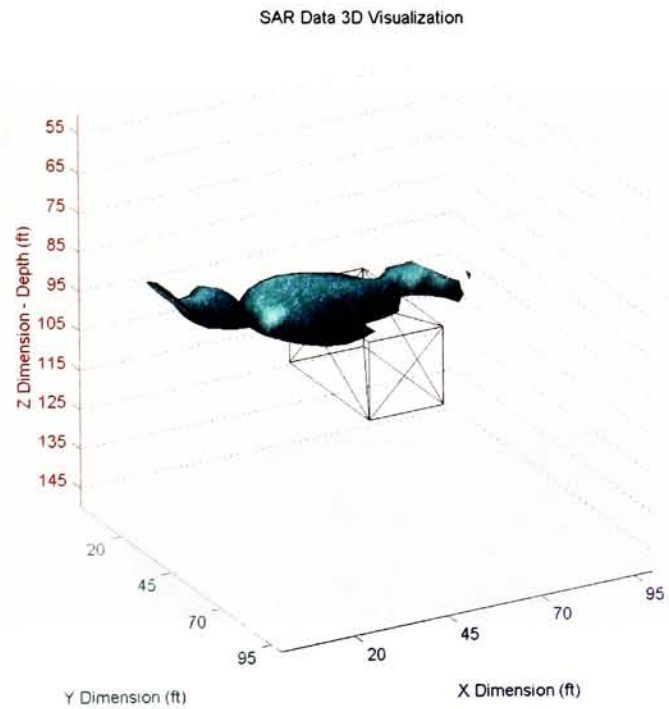

Figure 6.12b. Data Set 12 GPR Processed Image

Data Set 13:

Transmitter Origin:	(0,50,0)	**Ray Generation:**	Automatic
Receiver Array Location:	(100,50,0)	**Receiver Array Dimensions:**	(100,100,0)
Receiver Spacing X:	10	**Receiver Spacing Y:**	10
Target Location:	(52,52,-100)	**Target Size:**	(52,52,20)

Table 6.13: Data Set 13 Scene Configuration Information

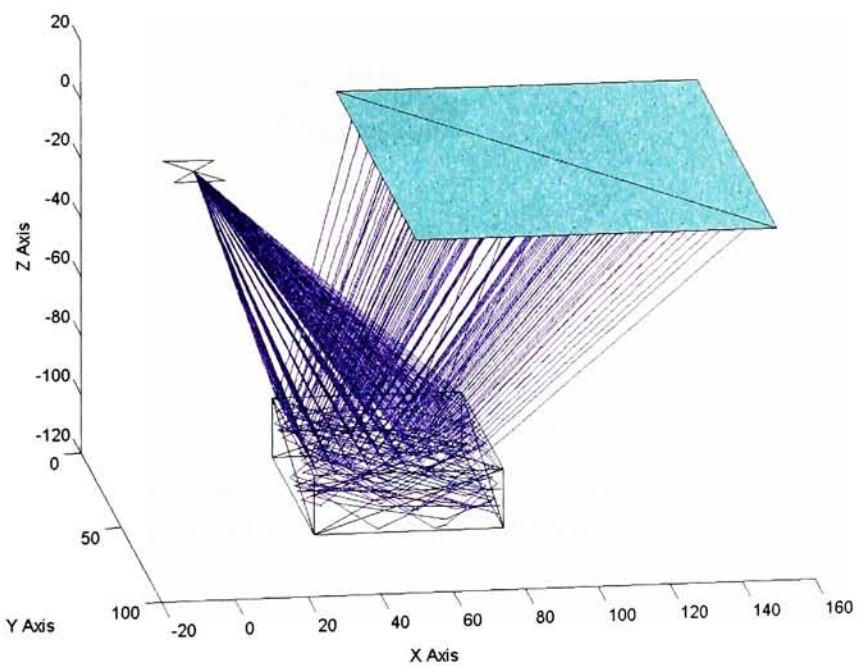

Figure 6.13a. Data Set 13 Scene Configuration Image

Data set 13 was set up similarly to data set 12, except automatic ray generator was used to generate the rays and size the transmitter to ensure a specular reflection to all of the receiver locations. The size and location of the target are almost identical to those for

data set 1, except the target in data set 13 is at a depth of –100ft. The orientation of this target caused some of the rays to be transmitted into the target.

The GPR processed image generated by data set 13 is shown in Figure 6.13b. The image is focused towards the front of the target. The tail that is apparent on many of the other images is gone in this image.

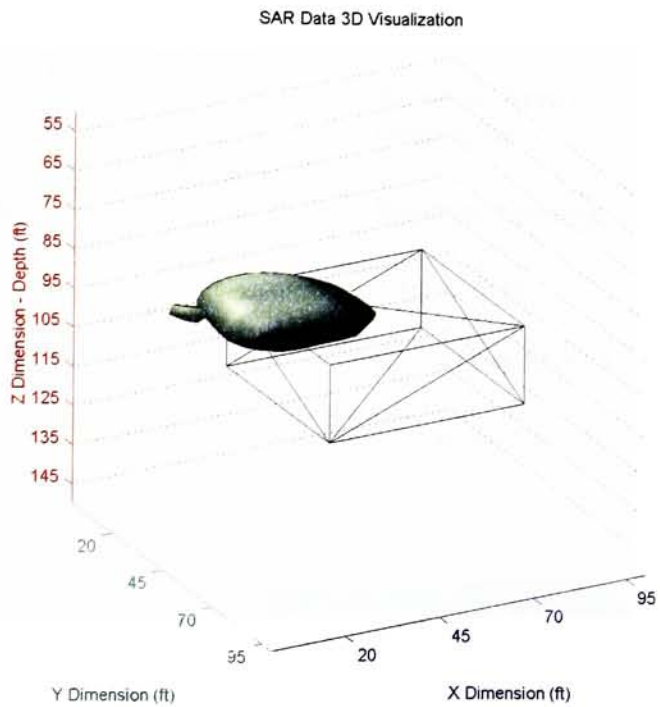

Figure 6.13b. Data Set 13 GPR Processed Image

6.2.2 Resolution / Number of Rays

The resolution of the image was varied in data sets 14-17. Two methods were used to change the resolution. The first method was to alter the number of rays transmitted into the scene. The second method was to change the voxel size used to generate the image in the GPR processing GUI. The scene used for these runs had the

transmitter located at (0, 50, 0). The target was located at (50, 50, -40) and its size was (20, 40, 20). The receiver array was centered at (100, 50, 0) with a size of 100ft by 100 ft. The receivers in the array were spaced at 10 ft in the X direction and 10 ft in the Y direction.

Data Set 14:

Transmitter Origin:	(0,50,0)	**Ray Generation:**	Manual
Receiver Array Location:	(100,50,0)	**Receiver Array Dimensions:**	(100,100,0)
Receiver Spacing X:	10	**Receiver Spacing Y:**	10
Target Location:	(50,50,-40)	**Target Size:**	(20,40,20)
Ray Array Size: X	26	**Ray Array Size: Y**	26

Table 6.14: Data Set 14 Scene Configuration Information

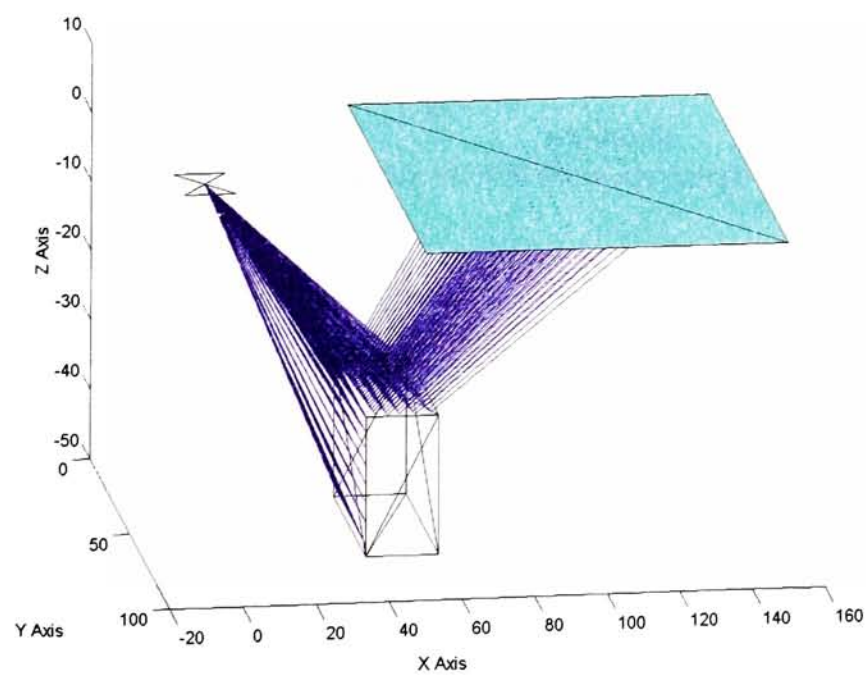

Figure 6.14a. Data Set 14 Scene Configuration Image

In data set 14, the voxel size setting in the GPR processing GUI was changed from 5 ft to 10 ft. This caused the GPR processed image to be larger and less defined than data set 8, where the voxel size was set to 5 ft. The GPR generated image has a broken tail that extends towards the transmitter, similar to the effects seen in data set 8.

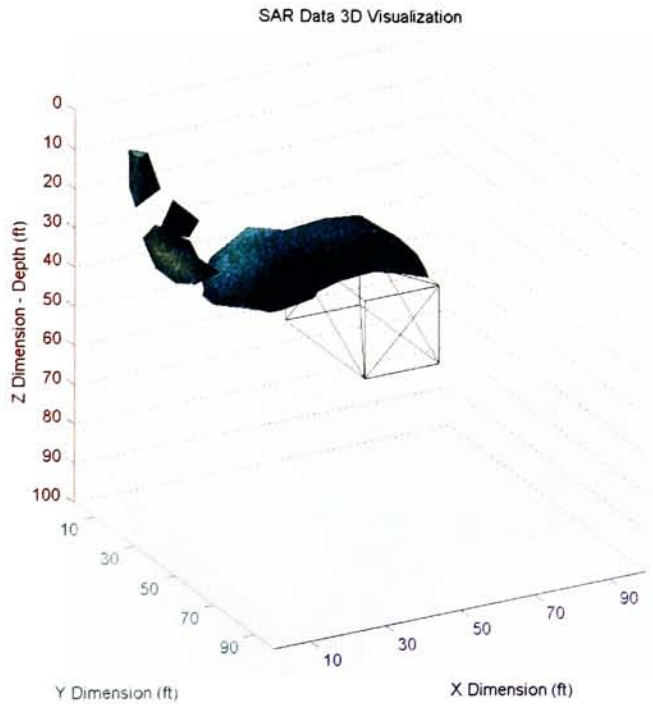

Figure 6.14b. Data Set 14 GPR Processed Image

Data Set 15:

Transmitter Origin:	(0,50,0)	**Ray Generation:**	Manual
Receiver Array Location:	(100,50,0)	**Receiver Array Dimensions:**	(100,100,0)
Receiver Spacing X:	10	**Receiver Spacing Y:**	10
Target Location:	(50,50,-40)	**Target Size:**	(20,40,20)
Ray Array Size: X	26	**Ray Array Size: Y**	26

Table 6.15: Data Set 15 Scene Configuration Information

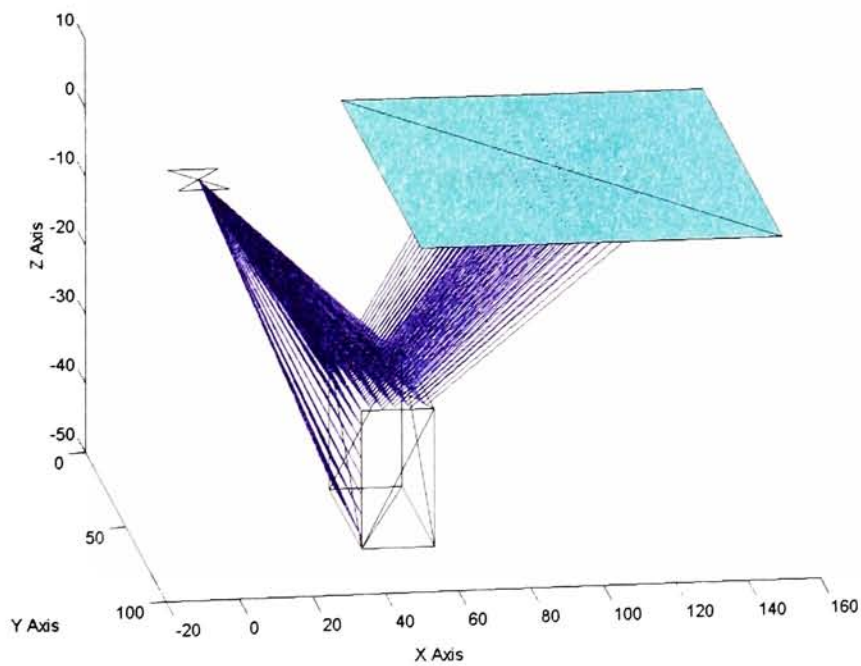

Figure 6.15a Data Set 15 Scene Configuration Image

Data set 15 was generated using the same transmitter, target, and receiver parameters as data set 8. The voxel size used to generate the GPR processed image was set to 2.5 ft in the X dimension and 2.5 ft in the Y dimension. The resulting image can be viewed in Figure 6.15b. Note that the image has improved resolution, although it is not

extremely different in shape than the image generated using data set 8.

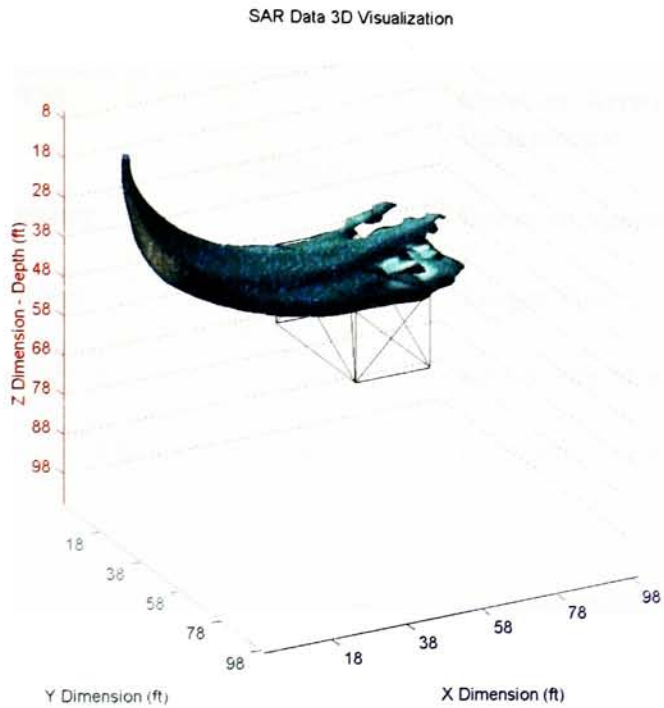

Figure 6.15b. Data Set 15 GPR Processed Image

Data Set 16:

Transmitter Origin:	(0,50,0)	**Ray Generation:**	Manual
Receiver Array Location:	(100,50,0)	**Receiver Array Dimensions:**	(100,100,0)
Receiver Spacing X:	10	**Receiver Spacing Y:**	10
Target Location:	(50,50,-40)	**Target Size:**	(20,40,20)
Ray Array Size: X	52	**Ray Array Size: Y**	52

Table 6.16: Data Set 16 Scene Configuration Information

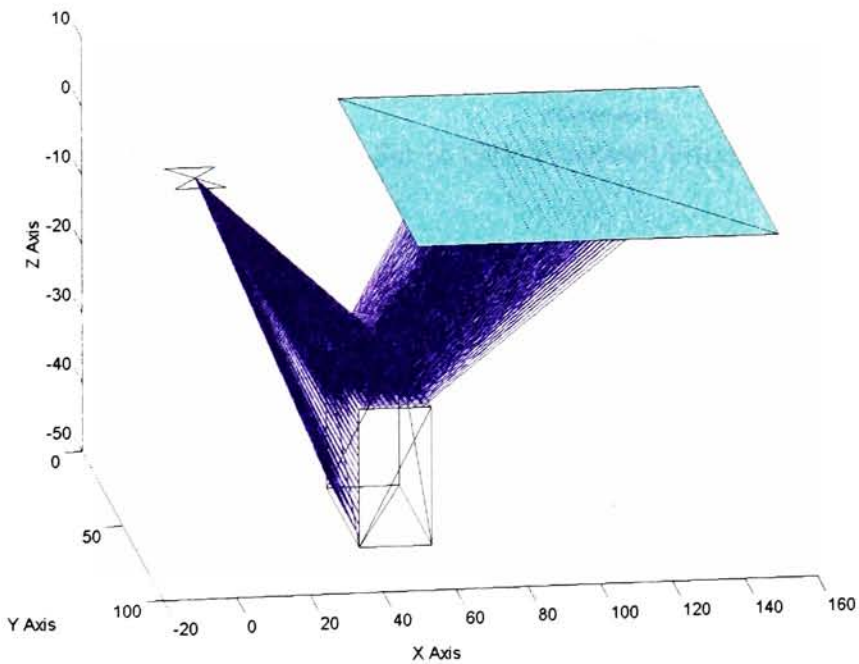

Figure 6.16a. Data Set 16 Scene Configuration Image

Data set 16 was generated by using an array of 52 by 52 rays. Four times as many rays were transmitted towards the target as compared to data set 8. The voxel size was reset to 5 ft. The resulting image, pictured in Figure 6.16b is very similar to the GPR processed image generated using data set 8.

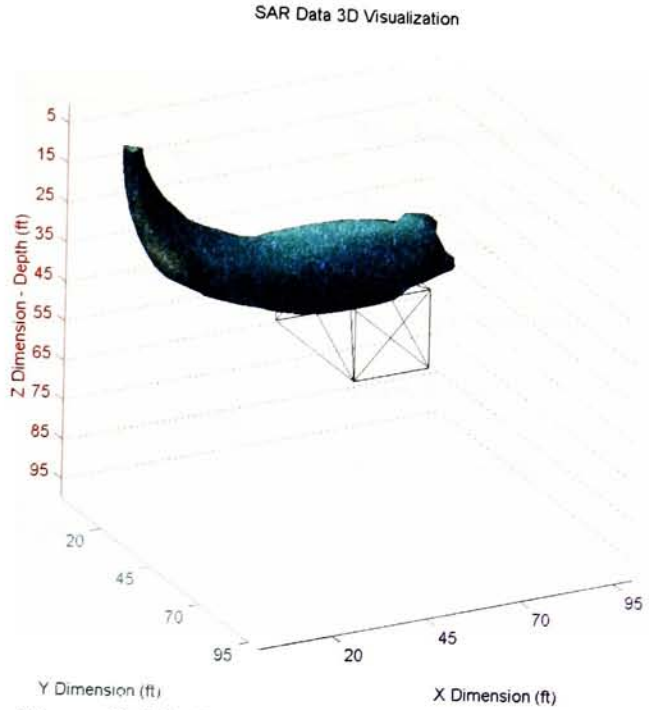

Figure 6.16b. Data Set 16 GPR Processed Image

Data Set 17:

Transmitter Origin:	(0,50,0)	**Ray Generation:**	Manual
Receiver Array Location:	(100,50,0)	**Receiver Array Dimensions:**	(100,100,0)
Receiver Spacing X:	10	**Receiver Spacing Y:**	10
Target Location:	(50,50,-40)	**Target Size:**	(20,40,20)
Ray Array Size: X	13	**Ray Array Size: Y**	13

Table 6.17: Data Set 17 Scene Configuration Information

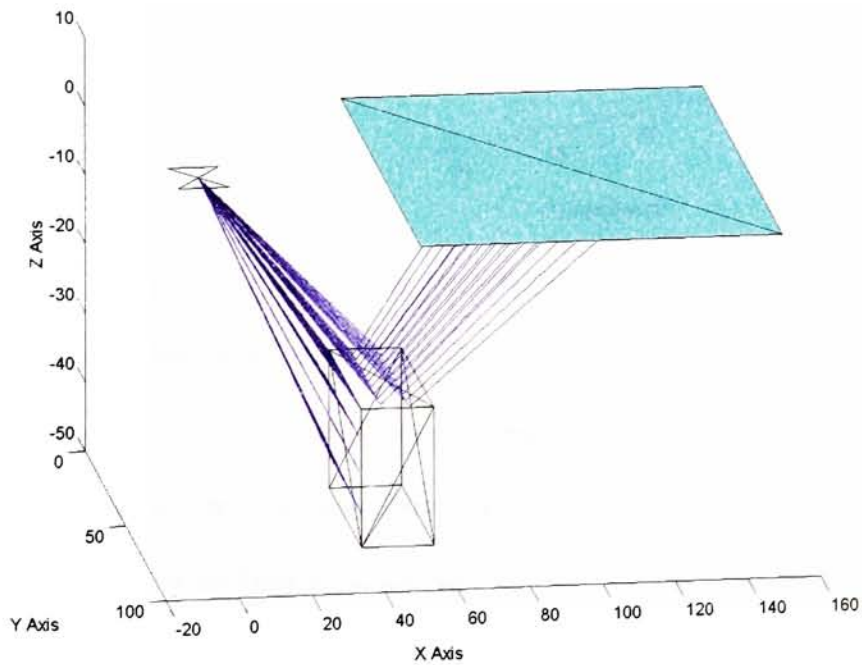

Figure 6.17a Data Set 17 Scene Configuration Image

In data set 17, a 13 by 13 ray array was used to generate the image. This is a quarter of the rays transmitted in data set 8. The image generated can be viewed as

Figure 6.17b. The image is slightly less resolved, with some clutter in the front and rear portions of the image.

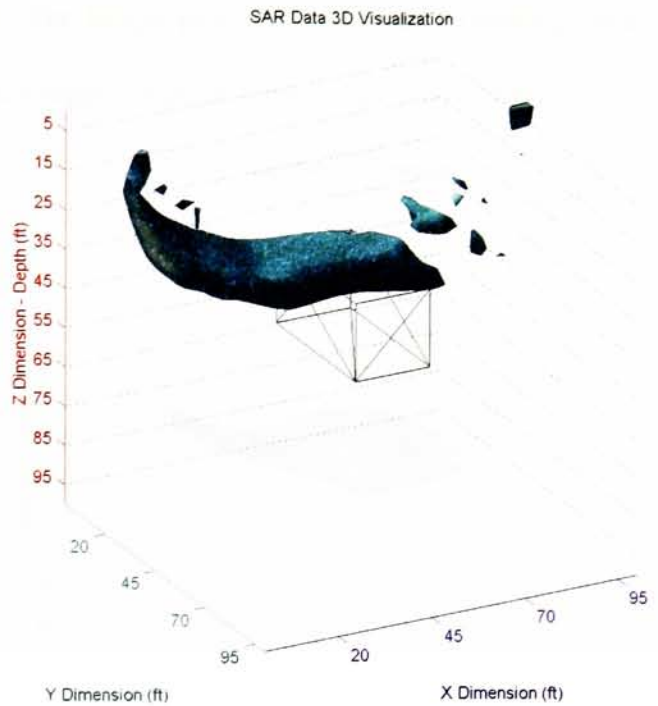

Figure 6.17b Data Set 17 GPR Processed Image

6.3 Uniform Point Scatterer Simulation

In data sets 18-20, the uniform point scatterer simulator created by Rome Labs was used to generate simulated images. The target used for these data sets consisted of a two dimensional array of uniform point scatterers in the X and Y dimensions. The array of scatterers was centered at (50, 50, -40). The dimensions of the array were 20 ft in the X direction and 40 ft in the Y direction. The receiver array used in data sets 18-20 was of dimensions 100 ft in the X direction and 100 ft in the Y direction, centered at (100, 50, 0). The receivers were spaced at 10 ft by 10 ft intervals within the receiver array.

In data set 18, the uniform point scatterers were spaced by 4 ft in the X direction and by 8 ft in the Y direction. The GPR processed image shown in Figure 6.18 shows the output of this run. The Image generated has a tail extending towards the transmitter in the X direction and a jagged edge on the front portion of the image.

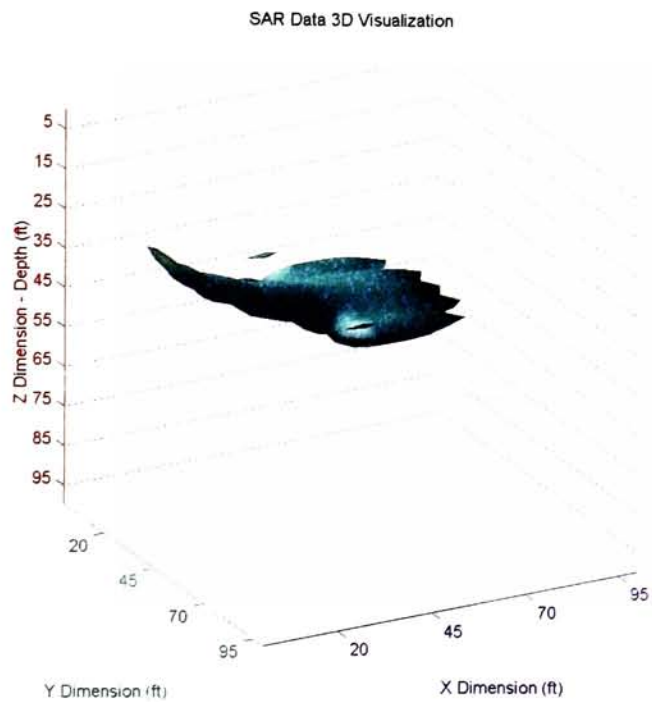

Figure 6.18. Data Set 18 GPR Processed Image

The scatterers were spaced by 2ft in the X direction and 4 ft in the Y direction in data set 19. The GPR processed image generated from this run can be viewed as Figure 6.19. While the image has a tail extending towards the transmitter, the image from the scatterer array is smooth and well resolved.

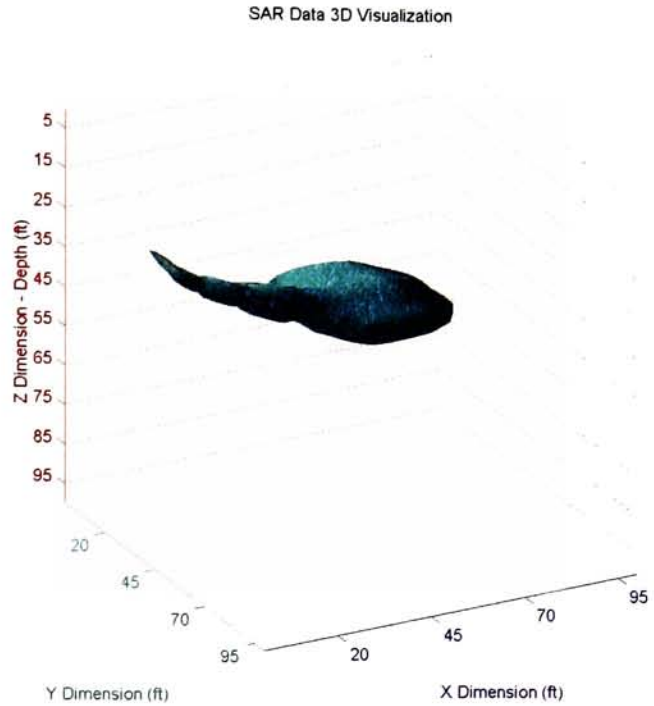

Figure 6.19. Data Set 19 GPR Processed Image

The final data set, data set 20, was generated using the uniform point scatterer simulation with the scatterers spaced by 10 ft in the X direction and 20 ft in the Y direction. The GPR processed image is shown in Figure 6.20. This image is discontinuous in the Y dimension, showing several shapes from each line of scatterers in the X direction.

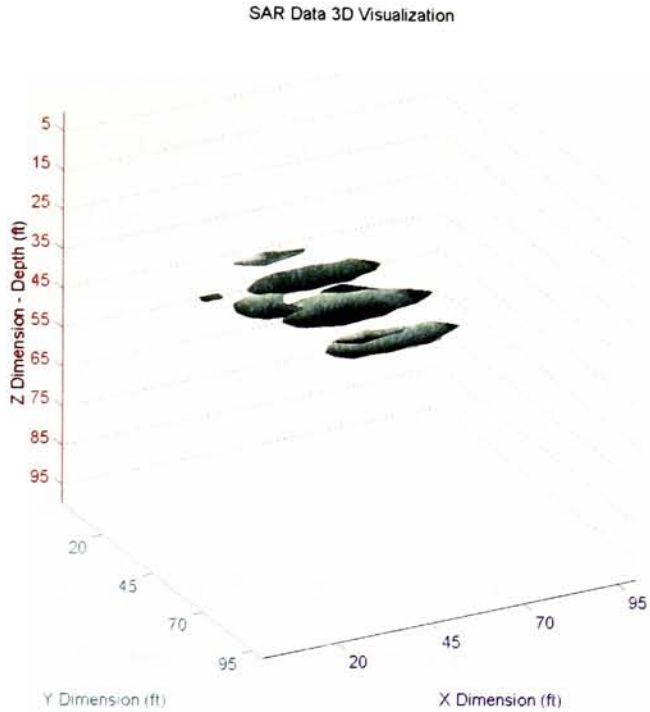

Figure 6.20. Data Set 20 GPR Processed Image

7. Discussion

The images generated using the ray-tracing simulator in Section 6 are dependent not only upon the size of the target, but also upon the configuration of the scene. This section will discuss the characteristics of these images and the effects scene configuration has upon them.

The path distance of each ray that is reflected from the target and received at a receiver location is indicative of the range from the transmitter to the receiver via the target. There is directional ambiguity associated with this range, as many points within the scene can be associated with this same range value. The points of equal range for a given transmitter location and receiver location form a three dimensional ellipse. This ellipse is pictured in two dimensions in Figure 7.1. For a horizontally oriented target, the bottom edge of the ellipse is located at the intersection point of the ray with the target. The width of the ellipse is dictated by the range.

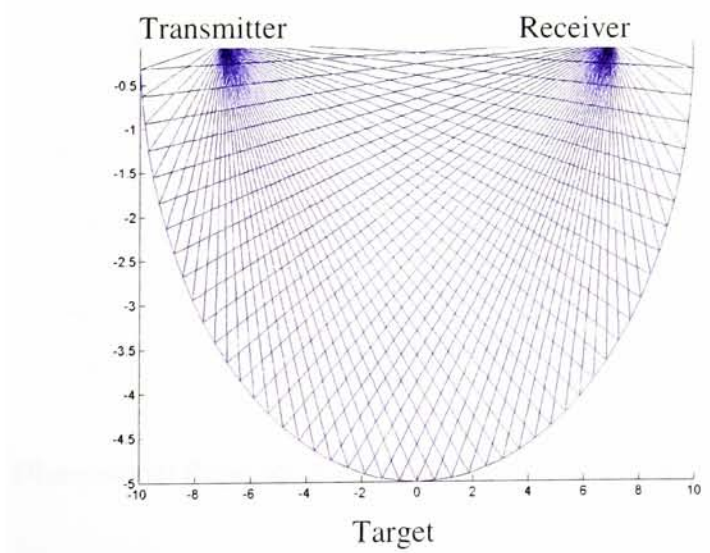

Figure 7.1 GPR Processing Directional Ambiguity Ellipse

The directional ambiguity associated with each received ray scribes a different ellipse. When a number of rays intersect the target in close proximity and are reflected towards the receiver array, these ellipses may overlap. By combining several ellipses, the directional ambiguity is reduced. In SAR processing, a magnitude value is assigned to each voxel in the ellipse based upon the voltage of the received signal. The processed image is created by additively combining the magnitude values of each voxel in the ellipses.

One characteristic of many of the GPR processed images is a tail extending from the top of the target towards the transmitter. This anomaly is caused by the overlap of several ellipses that are spaced along the top of the target and steadily increasing in width and will be referred to as the tail effect. This phenomenon is pictorially illustrated in Figure 7.2, which shows a two dimensional representation in the X dimension.

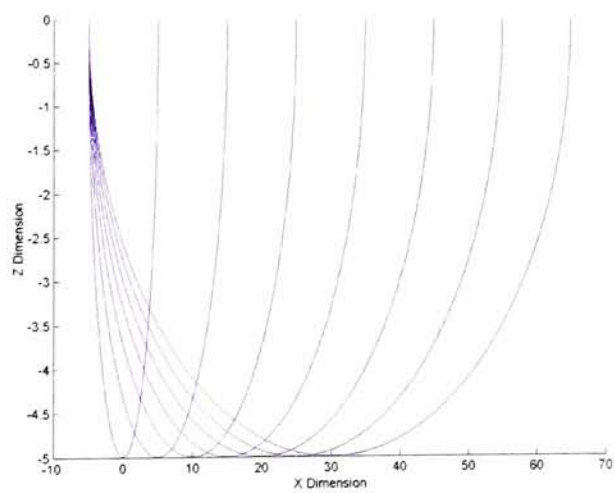

Figure 7.2 Two Dimensional Representation of GPR Processed Image in X Dimension

The ellipses pictured are equally spaced at 5 units, and steadily increasing in width in the X direction by 5 units, from left to right. In an imaged scene, the width of the ellipses increase because the path distances are steadily increasing for specular reflections at receiver locations further from the transmitter. The near proximity and overlap of these ellipses cause a high magnitude value for the voxels in the area where the tail is formed.

Many of the images in Section 6 are shifted towards the side of the target closest to the transmitter. This is also a function of the increasing focus of the ellipses. In Figure 7.2, several of the ellipses on the left side of the plot overlap. In an image generated using the GPR processor, the magnitude of the voxels in this region would be greater than the non-overlapping, wider ellipses on the right side of the image. This is the reason that the transmitter side of the GPR processed image frequently has a greater magnitude than the receiver side, an effect that will be referred to as range distortion.

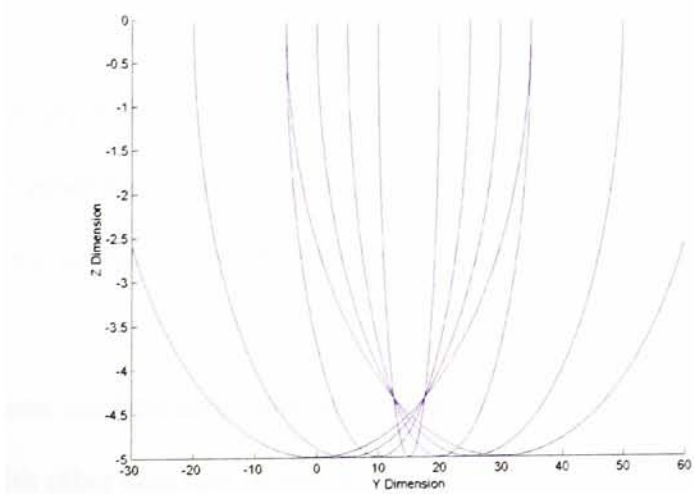

Figure 7.3 Two Dimensional Representation of GPR Processed Image in Y Dimension

Figure 7.3 shows a two dimensional representation of increasing ellipses in the Y dimension. The shortest path distance is associated with the center path in a scene that is symmetric in the Y dimension. The path distances increase with increased deviation from the center. In Figure 7.3, the ellipses are evenly spaced and steadily increasing in width as they deviate from the center. In an image generated by the GPR processor, the wider ellipses on either end would contribute to the narrow ellipse in the center, making the magnitude of the voxels relatively high in the center of the image. There is a sparse concentration of ellipses on the edges of the image, which would result in voxels of a lower magnitude in that region. This effect will be referred to as cross-range distortion.

7.1 Automatic Ray Generation

The images in Section 6.1 were created using the automatic ray generator. The direction of the transmitted rays and the size and position of the target were calculated to ensure that each receiver in the receiver array received a ray that was reflected specularly from the top of the target. Generating the rays this way allows the receiver array parameters and target depth to be changed while ensuring that a resolvable scene will result. It also generates a system of rays that are evenly spaced along the top of the target, which is a useful way to observe the tail effect, range distortion, and cross-range distortion.

The scene configuration used in data set 1 was selected to provide a basis for comparison with other data sets in this section. As can be seen in Figure 6.1b, the image generated in this data set have the characteristic tail and weighting on the transmitter side of the target associated with the tail effect and range distortion. Figures 7.4 a and b

illustrate these effects in the X and Y dimensions. They show a two-dimensional representation, although the actual generated ellipses are three-dimensional. The X dimension representation shows a cut taken down the center of the scene at the transmitter location. The Y dimension shows a cut taken along the first line of rays that intersect with the target. These plots were not created using the GPR processing software, but were generated using information from actual simulations. The foci and spacing of the ellipses were calculated from the path distances of rays projected in data set 1.

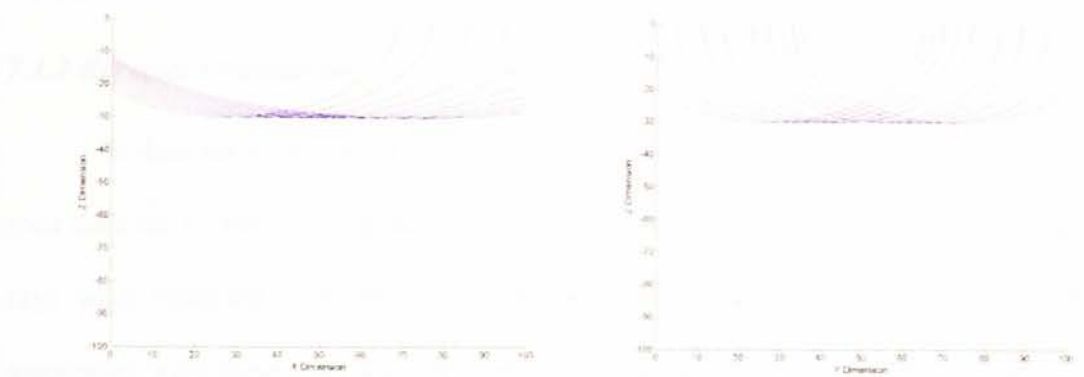

(a) **(b)**

Figure 7.4 X and Y Ellipse Representation of Data Set 1

The actual ellipses effect that creates the scene are three dimensional, and can be visualized by additively combining Figures 7.4 a and b. Figures 7.4a shows a high density of ellipses in the X dimension along the top of the target and along the tail extending in the direction of the transmitter. Figure 7.4b shows the ellipse diagram in the Y dimension for data set 1. The ellipses are most concentrated at in the center of the scene, a direct effect of cross-range distortion. This is consistent with the GPR processed image of data set 1, Figure 6.1b.

7.1.1 Transmitter Orientation

The images created in Section 6.1.1 were generated by varying the position of the transmitter relative to a fixed target and receiver location. The GPR processed images for data sets 1,2, and 3 exhibit tail effect, range distortion, and cross-range distortion as a result of the widening of the directional ambiguity ellipses. The shape of the generated image is similar in each of the data sets, but the orientation is different. The tails generated extend in the direction of the transmitting antenna. The generated images do not extend to the side of the target opposite the transmitter.

7.1.2 Receiver Orientation

In data set 4, the density of receivers in the array was increased by a factor of four over data set 1. Because the automatic ray generator was used, a greater concentration of rays were reflected from the target and received at the receiver array. The ellipses associated with these rays were spaced closer together than in data set 1. Figures 7.5 a and b show the effect of decreasing the distance between ellipses.

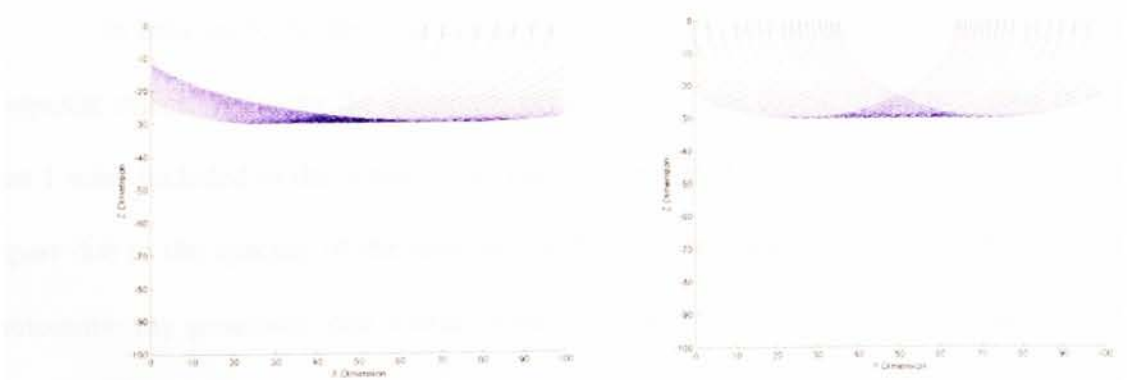

(a) **(b)**

Figure 7.5 X and Y Ellipse Representation of Data Set 4

Figure 7.5a is similar to Figure 7.4a, except the greater concentration of ellipses extends along the target further in the X direction. The ellipses are also distributed over a larger spacing in the Y dimension, resulting in less pronounced range and cross-range distortion. Both of these features can be observed in Figure 6.4b, as the resolved image is slightly larger compared to Figure 6.1b. The increased number of receivers in the array created an image that was well resolved, following the contours of the target better than the image generated using data set 1.

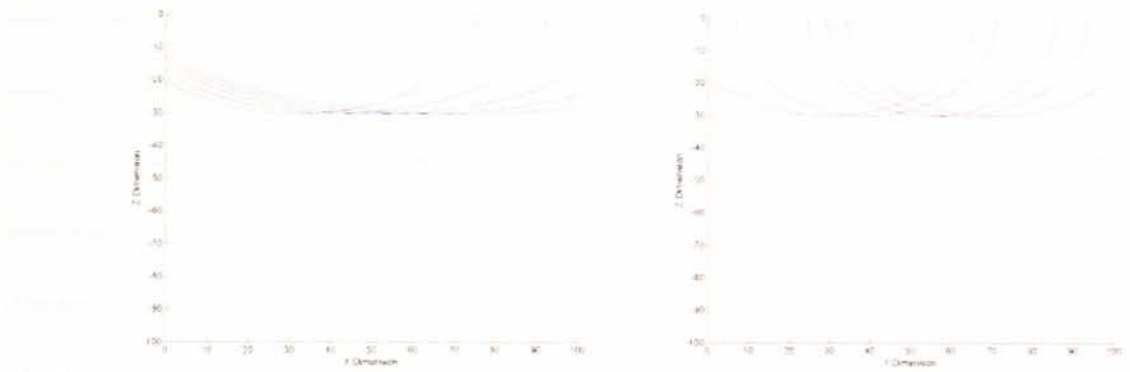

(a) **(b)**

Figure 7.6 X and Y Ellipse Representation of Data Set 5

In data set 5, the decreased number of receivers within the receiver array has the opposite effect. By using the automatic ray generator, one fourth of the rays used in data set 1 were included in the scene. The ellipses generated in the image are spaced further apart due to the spacing of the rays, as can be seen in Figure 7.6 a and b. By using the automatic ray generator, one fourth of the rays used in data set 1 were included in the scene. The ellipses generated in the image are spaced further apart due to the spacing of the rays, as can be seen in Figure 7.6 a and b.

The GPR processed image, shown in Figure 6.5b has a less concentrated tail than Figure 6.1b or 6.4b. The cumulative returns in the vicinity of the top of the target are small compared to the relative magnitude along the tail of the image. The image is concentrated in the Y dimension on the side of the target closest to the origin. This is because there are more rays reflected towards the receiver array on that side of the target.

The size of the receiver array was varied in data sets 6 and 7. In data set 6, the size of the receiver array was increased by 50 ft in the Y dimension. This added 55 additional receivers to the array, and consequently 55 additional rays to generate the image. The GPR processed image generated can be viewed as Figure 6.6b. The image created is wider in the Y dimension than the image created using the 100 ft by 100 ft receiver array. The ellipse diagram for data set 6 is shown as Figure 7.7. The X dimension cut is similar to that for data set 1 (shown as Figure 7.4a). The Y dimension plot is similar to 7.5b, which was generated using a higher concentration of rays. The

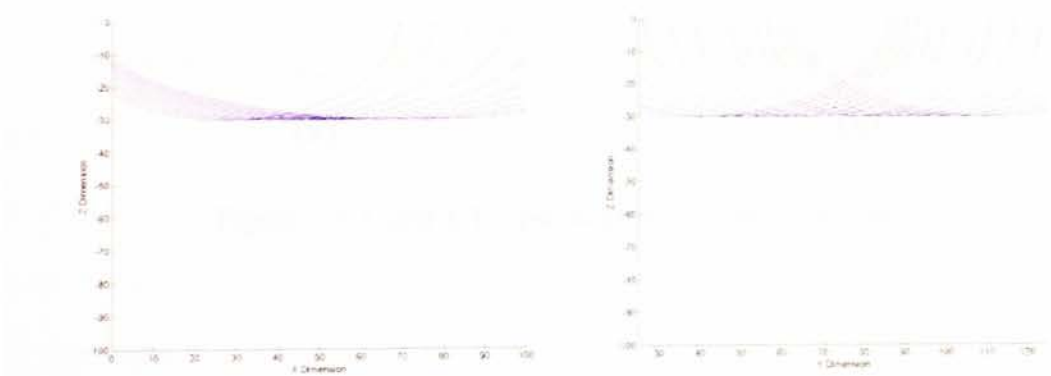

(a) **(b)**

Figure 7.7 X and Y Ellipse Representation of Data Set 6

increased receiver array size caused a greater number of ellipses in the Y dimension, along with a greater spreading of the width of the ellipses.

In data set 7, the receiver array was extended in the X dimension. The GPR processed image for this data set extends somewhat further in the X dimension than the image generated in data set 1, although it is approximately the same size in the Y dimension. Increasing the size of the receiver array caused a greater number of ellipses in the X dimension with an increased range of ellipse widening. This effect is shown in Figure 7.8.

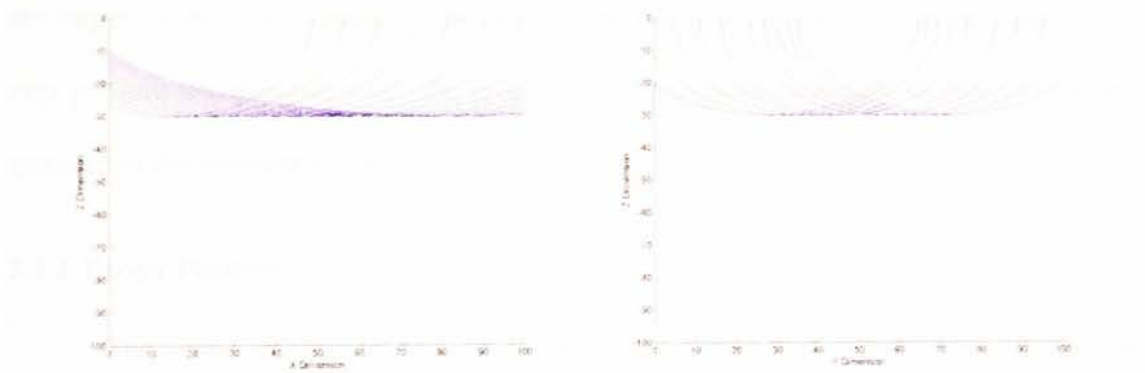

(a) **(b)**

Figure 7.8 X and Y Ellipse Representation of Data Set 7

7.2 Manual Ray Generation

Data sets 8-17 were formed using manual ray generation, which is required if a specific antenna model is desired. The rays created by the manual ray generator are evenly spaced in polar coordinates and aimed by the user. The rays therefore do not

intersect the top of the target at even Cartesian intervals, making it difficult to quantify the tail effect, range distortion, and cross-range distortion, although these phenomena are present. This section is used to demonstrate the image implications of different ray parameters in the scene.

Data set 8 was used to provide a comparison benchmark for the other data sets in the section. The image generated using data set 8 is included in Section 6 as Figure 6.8b. Similar to the images in the previous section, data set 8's image exhibits the tail effect. The ray spacing when using manual ray generation is much smaller than when the automatic ray generator is used, causing the generated image to cover the entire width of the target in the Y dimension. The rays in the manual ray tracing runs are spaced at 3 rays per unit wavelength, while the automatically generated rays only include one ray per receiver in the receiver array.

7.2.1 Target Position

The scene imaged in data set 9 includes a target that is stretched to cover the entire scene of interest and rotated so the long dimension is in the X direction. There are a large number of transmitted rays within the target, many of which eventually intersect with the receiver array. There are also several rays that reflect repeatedly between the top of the target and the ground / air interface, ultimately intersecting the receiver array. These rays can cause some anomalies, as their path distance may be much longer than the direct path distance to the target. The GPR processed image, shown in Figure 6.9b, shows some anomalies in the upper left side of the image, however the anomalies are not as extensive as would be expected from the number of rays that intersect the receiver

array as a result of multiple reflections. The reason these rays do not affect the image to a greater extent is that many of their path distances are too large to be included in the imaged scene. If the imaging window is extended to a lower depth, the effects of these additional rays will be apparent.

Another characteristic of Figure 6.9b is that the image is clustered around the transmitter side of the target. There is no image generated along the side of the target that is furthest from the transmitter. While range distortion contributes to this effect, but it is also caused by the spacing of the transmitted rays. The rays are spaced evenly in polar coordinates, causing the rays to intersect the target quite densely close to the transmitter and sparsely further from it. The closely spaced rays produce more densely spaced ellipses closer to the transmitter, resulting in a higher magnitude voxels in that region.

In data set 10, the target is once again stretched to cover the entire imaging window, but it is oriented so its longer dimension is in the Y direction. The resulting image, shown in Figure 6.10b is focused in the center of the target, with no return from either of the sides of the target. This is not expected, as the rays are transmitted along the length of the target. The image in Figure 6.10b is actually smaller than the one generated with data set 8, which used a smaller target.

The reason for these unexpected results is two-fold. First, while the rays are extended along the entire length of the target, the orientation of the scene causes the rays on either end of the target to extend past the width of the receiver array. The rays on either end of the target were reflected beyond the boundaries of the receiver array. The actual length of the target that provides a valid reflection towards the receiver array is

only a little larger than the target used in data set 8. Secondly, there is a higher concentration of rays intersecting the valid section of the target, causing several rays to be reflected to the same receiver location. This causes a high concentration of ellipses in the center of the target, magnifying the effects of cross-range distortion.

The scene orientation selected for data set 11 insured that no rays were specularly reflected from the top of the target to the receiver array. All of the rays that intersect the array are first transmitted through the target, subject to several reflections within the target, and then reflected back towards the receiver array. In data set 9, there were several transmitted and multiple reflected rays in the scene, but their path distances were too long to be included in the image. In data set 11, the distance traveled by the transmitted rays is on the order of the path distances used to calculate the processed image. The ellipses generated by these rays are therefore visible in the imaging window. There are three distinct layers of the cluttered image generated in Figure 6.11b. These are generated by groups of rays having similar reflected paths within the target. The generated image is very cluttered and it would be nearly impossible to define the target within it.

The depth of the target was increased to 100 ft below ground in data set 12. The generated image, pictured as Figure 6.12b is well resolved, and the tail effect is less defined. The tail is not as visible in this image because the overall path distance difference is smaller for targets at greater depths. The tail effect is therefore diminished. Figure 6.13b was generated using the automatic ray generator with a target at the same

depth as in data set 12 to further demonstrate this effect. Figure 7.9 a and b depict the ellipses generated in the X and Y planes for data set 13.

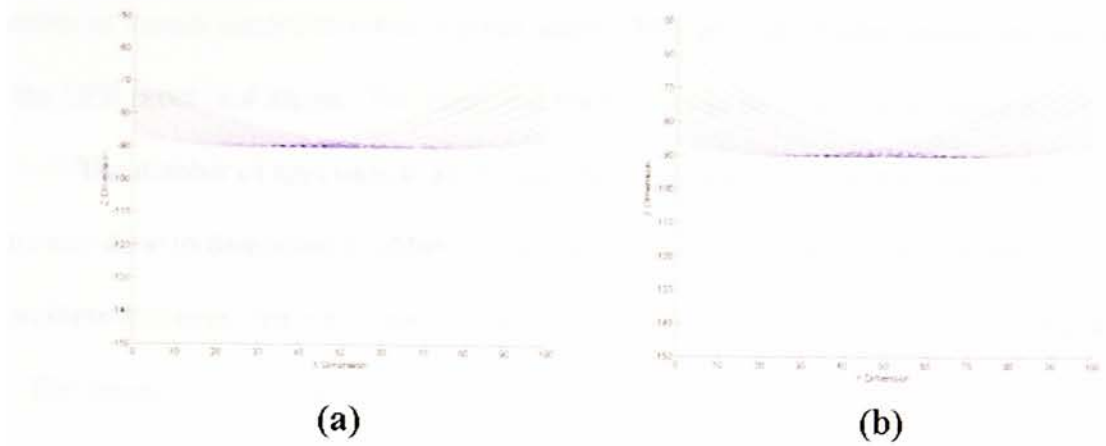

(a) (b)

Figure 7.9 X and Y Ellipse Representation of Data Set 13

As can be seen in Figure 7.9a, there is very little change in the width of the ellipses in the X direction. The result of this can be viewed in Figure 6.13b.

7.2.2 Resolution / Number of Rays

In data sets 14 and 15, the size of the voxels used to divide the scene was varied. These voxels are used to calculate the reference path length when creating the GPR processed image. Increasing the size of the voxels will decrease the number of voxels needed to cover a given scene. This degrades the image resolution because the size of the voxels used in SAR processing are the same as the voxels used to generate the image. In data set 14, the size of the voxels was increased to 10 ft. The resulting image is shown as Figure 6.14b. While the scene configuration and rays used to generate the image were identical to those used in data set 8, the GPR processed image is quite different. The generated image does not follow the contours of the target as accurately as in Figure 6.8b.

In contrast, Figure 6.15b is well resolved and follows the contours of the target very well. Data set 15 was generated by decreasing the size of the voxels, increasing the number of voxels needed to cover a given scene. This provides higher spatial resolution in the GPR processed image. The improved resolution can be observed in Figure 6.15b.

The number of rays used to illuminate the target was varied in data sets 16 and 17. This was done to determine if additional rays improve the generated image. Figure 6.16b represents an image that was created using four times the number of rays used in data set 8. The image is very similar in appearance to Figure 6.8b, which was generated with much fewer rays. This suggests that the number of rays used in data set 8 was sufficient to accurately illuminate the target.

In data set 17, the number of rays used to illuminate the scene was decimated by a factor of four compared to data set 8. The image, appearing as Figure 6.17b follows the contours of the target, but has additional clutter on the right and left sides of the image.

7.3 Uniform Point Scatterer Simulation

Figures 6.18 – 6.20 were generated to display the capabilities of the uniform point scatterer simulation. These images were generated with a target model composed of a two-dimensional point scatterer array. The spacing of the point scatterers was varied to show different resolutions. In Figures 6.18 and 6.19, the processed image is well resolved and conforms to the shape of the original target. There is a tail extending from the main target return in the direction of the transmitter. Figure 6.20 is not as well resolved as the others and the correct target shape is difficult to discern.

While the uniform point scatterer simulation is capable of generating well resolved images, it does not account for the electromagnetic effects of the transmitter, or the three-dimensional effects of the target. The uniform point scatterer simulation assumes that each point in a scene reflects equally to every receiver location. The reflection is actually dependent upon the orientation of the scene and the configuration of the target. The images generated with this simulation are an idealized view of the best possible image.

8. Conclusions

There are two main areas to which this thesis has provided a contribution. The first area of contribution is in creating an electromagnetic simulator for use with the Rome Labs GPR system. The second is an assessment of how different ray-tracing scene parameters impact the images generated by the Rome Labs GPR system. In this chapter, the strengths and limitations of the simulator described in this thesis will be discussed. We will also discuss future topics of research that could improve the ray-tracing GPR simulator.

8.1 Simulation

The simulator presented in this thesis provides an additional functionality to the Rome Labs GPR system. The capability of modeling a specularly reflected electromagnetic signal was added through this effort. The target model was also expanded to model complex, three-dimensional targets. The targets exhibit shadowing and also have dielectric properties associated with them. More flexibility was added to the transmitter model, allowing for antenna directivity and different antenna gain patterns.

8.2 Assessment of Ray-Tracing Effects

To assess the effectiveness of the ray-tracing technique to simulate returns in the Rome Labs GPR system, it is necessary to have a set of returns from a controlled environment where the dielectric properties of the target and ground are known. This information is not available; however, it is useful to observe the effects that the simulation has upon the generated image to aid in assessing the results when this information is available. There are several scene specific parameters that have an impact

on the generated image when implementing the ray-tracing simulation with the Rome Labs GPR processing system. The scene configuration, ray orientation, and system parameters must be considered, as they each have an affect upon the image.

The processed image is affected by scene configuration factors such as the size and position of the target relative to the transmitter and receiver array. Targets at a greater depth have less variation in their path distance, lessening the tail effect that is prevalent in more shallow targets. Target surfaces that are at acute angles to the transmitter are more likely to have rays that are transmitted into the surface of the target. These transmitted rays can cause clutter as they are reflected within the target and back towards the receiver. Multiple reflections between the target and the ground can also cause anomalous returns in some orientations.

The manually selected rays must be chosen carefully to ensure that enough rays are transmitted and that their orientation will make them useful. The density and spacing of the transmitted rays must be chosen to reflect the size and complexity of the target. An insufficient number of rays can result in decreased resolution. The configuration of the scene must also be considered in selecting the swath of rays. If a small receiver array is used, in conjunction with a large target, many of the specularly reflected rays may extend beyond the size limits of the receiver array.

Other system parameters can also have an impact upon the generated image. The voxel size of the imaged scene has an impact on the resolution of the image. The image is also affected by the size and density of the receiver array.

8.3. Future Work

While this thesis provides the start of creating an effective simulator, the work is by no means complete. Several assumptions were made in creating the ray-tracing simulator described in this thesis. The effects of diffraction were disregarded, an assumption that is valid if the return from the edges of the target are not determined to be significant. [4] If the effect of these regions is of interest, additional rays in the vicinity of the edges of the target can be generated to mimic the effects of diffraction.[9]

It was also assumed that the dielectric permittivity was constant within a target and that the magnetic permeability was constant throughout the scene. The dielectric permittivity can be varied within a specific target by dividing the target into smaller concentric targets. These concentric targets can be assigned a different dielectric, simulating the effects of a dielectric gradient.

The effects of dispersion were also not modeled. Goodman proposed combining the results of several different ray trace runs with different material parameter settings to simulate dispersion. [7]

The ray-tracing technique models specular reflections only. Schott discusses non-specular reflection in *Remote Sensing: The Image Chain Approach* stating that the reflection from a typical surface exhibits both diffuse and specular reflection characteristics. It is possible to combine the Uniform Point Scatterer simulation, which models perfectly diffuse reflections with the ray-tracing simulation, which models perfectly specular reflections to model surfaces that exhibit properties of both.

Figure 8.1 shows an image generated by the Rome Labs system from a data set that was collected at the Nevada Test Site facility outside of Las Vegas, Nevada. The

expected target is superimposed in the center of the image, with its longest dimension in the Y direction. There are several areas in this image that exhibit similar phenomena to those effects discussed in Section 7 of this thesis. With additional simulation analysis, it is possible that other anomalies in the scene can be explained and used to better interpret images in the future.

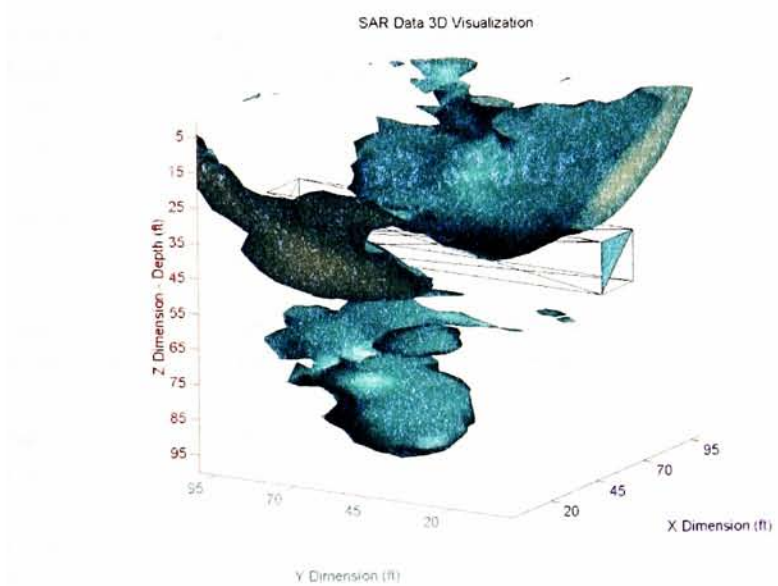

Figure 8.1 Nevada Test Site Example Image

BIBLIOGRAPHY AND CITATION INDEX

[1] Kane S. Yee, "Numerical Solution of Initial Boundary Value Problems Involving Maxwell's Equations in Isotropic Media", IEEE Transactions on Antennas and Propagation, Vol. AP-14, No. 8 May, 1966.

[2] Jean-Pierre Berenger, "Three-Dimensional Perfectly Matched Layer for the Absorption of Electromagnetic Waves", Journal of Computational Physics, Vol. 127 pp. 363-379, 1996.

[3] Yasuhiro Nishioka, Osamu Maeshima, Toru Uno, and Saburo Adachi, "FDTD Analysis of Resistor-Loaded Bow-Tie Antennas Covered with Ferrite-Coated Conducting Cavity for Subsurface Radar", IEEE Transactions on Antennas and Propagation, Vol. 47, No. 6, June 1999

[4] David Halliday and Robert Resnick, *Fundamentals of Physics*, John Wiley & Sons, Inc., New York, 1981.

[5] Jun Cai, and George A. McMechan, "Ray-Based Synthesis of Bistatic Ground-Penetrating Radar Profiles", Geophysics, Vol. 60, No. 1, January-February 1995

[6] Andrew S. Glassner, *Introduction to Ray Tracing* Academic Press Inc., San Diego, California, 1989.

[7] Dean Goodman, "Ground-Penetrating Radar Simulation in Engineering and Archaeology", Geophysics, Vol. 59, No. 2, February 1994

[8] Users Manual for XPATCH, DEMACO, 100 Trade Centre Drive, Champaign IL, 1993

[9] Toru Sato, Toshio Wakayama, and Kazuhisa Takemura, "An Imaging Algorithm of Objects Embedded in a Lossy Dispersive Medium for Subsurface Radar Data Processing", IEEE Transactions on Geoscience and Remote Sensing, Vol. 38, No. 1, January 2000

[10] Eugene Hecht, *Optics*, Addison Wesley Longman, Inc., Reading Massachusetts, 1998.

[11] Markus Zahn, *Electromagnetic Field Theory: A Problem Solving Approach*, Robert E. Krieger Publishing Company, Inc., Malabar, Florida, 1987

[12] Edward C. Jordan and Keith G. Balmain, *Electromagnetic Waves and Radiating Systems*, Prentice Hall, Inc., Englewood Cliffs, New Jersey, 1968

[13] Liang Chi Shen, and Jin Au Kong, *Applied Electromagnetism*. PWS Publishing Company, Boston, Massachusetts, 1987

[14] Occupational Health & Safety Administration. "Extent of Near Field Region." http://www.oshaslc.gov/SLTC/radiofrequencyradiation/rfpresentation/microwavemeasure/non2.html, August 5, 2002. US Department of Labor.

[15] Merrill I. Skolnik, *Introduction to Radar Systems*, McGraw Hill, Boston, Massachusetts, 1980.

[16] Fabrice Hollender, and Sylvie Tillard, "Modeling Ground-Penetrating Radar Wave Propagation and Reflection with the Jonscher Parameterization", Geophysics, Vol. 63, No. 6, November-December, 1998.

[17] William B. Jones, *Introduction to Optical Fiber Communication Systems*. Holt, Rinehart and Winston, Inc., Fort Worth, Texas, 1988

[18] Richard P. Feynman, *QED The Strange Theory of Light and Matter*. Princeton University Press, Princeton, New Jersey, 1988

[19] Gary M. Miller, *Modern Electronic Communciation*. Prentice-Hall Inc., Englewood Cliffs, New Jersey, 1996

[20] Warren L. Stutzman, and Gary A. Theile, *Antenna Theory and Design*. John Wiley and Sons, New York, New York, 1981

[21] Narayana N. Rao, *Elements of Engineering Electromagnetics*. Printice-Hall, Inc., Englewood Cliffs, New Jersey, 1977

[22] E. Douglas Lynch, Russell D. Brown, David D. Mokry, James M. VanDamme, Michael C. Wicks, "Experimental HF Radar for Sub-Surface Sensing", 7th International Conference on Ground-Penetrating Radar, 27-30 May, 1998

[23] Lawrence B. Conyers, and Dean Goodman, *GROUND-PENETRATING RADAR: An Introduction for Archeologists*. AltaMira Press, Walnut Creek, Cal, 1997

[24] John R. Schott, *Remote Sensing The Image Chain Approach*. Oxford University Press, New York, New York, 1997

[25] Paul Lorrain, and Dale R. Corson, *Electromagnetic Fields and Waves*. W. H. Freeman and Company, San Francisco, California, 1970

[26] Christoph E. Baumann, and Edson E.S. Sampaio, "Electric Field of a Horizontal Antenna Above a Homogeneous Half-Space: Implications for GPR", Geophysics, Vol. 65, No. 3, May-June 2000

[27] Jose M. Carcione, and Michael A. Schoenberg, "3-D Ground-Penetrating Radar Simulation and Plane-Wave theory in Anisotropic Media", Geophysics, Vol. 65, No. 5, September-October 2000

[28] Ying Wang, Safieddin Safavi-Naeini, and Sujeet K. Chaudhuri, "A Hybrid Technique Based on Combining Ray Tracing and FDTD Methods for Site-Specific Modeling of Indoor Radio Wave Propagation", IEEE Transactions on Antennas and Propagation, Vol. 48, No. 5, May 2000

[29] George A. Deschamps, "Ray Techniques in Electromagnetics", Proceedings of the IEEE, Vol. 60, No. 9, September 1972

[30] Albane C. Saintenoy and Albert Tarantola, "Ground-Penetrating Radar: Analysis of Point Diffractors for Modeling and Inversion", Geophysics, Vol. 66, No. 2, March-April 2001

[31] Tsili Wang and Michael L. Oristaglio, "3-D Simulation of GPR Surveys Over Pipes in Dispersive Soils", Geophysics, Vol. 65, No. 5, September-October 2000

[32] George A. Deschamps, "Ray Techniques in Electromagnetics", Proceedings of the IEEE, Vol. 60, No. 9, September 1972

[33] Shung Wu Lee, "Electromagnetic Reflection From a Conducting Surface: Geometrical Optics Solution", IEEE Transactions on Antennas and Propagation, Vol. AP-23, No. 2, March 1974

[34] Xiaoxian Zeng, George A. McMechan, Jun Cai, and How-Wei Chen, "Comparison of Ray and Fourier Methods for Modeling Monostatic Ground-Penetrating Radar Profiles", Geophysics, Vol. 60, No. 6, November-December 1995